FFI RAPPORT

ELECTROMAGNETIC SHADOW EFFECTS BEHIND WIND TURBINES

HØYE Gudrun

FFI/RAPPORT-2007/00842

ELECTROMAGNETIC SHADOW EFFECTS BEHIND WIND TURBINES

HØYE Gudrun

FFI/RAPPORT-2007/00842

FORSVARETS FORSKNINGSINSTITUTT
Norwegian Defence Research Establishment
P O Box 25, NO-2027 Kjeller, Norway

FORSVARETS FORSKNINGSINSTITUTT (FFI)
Norwegian Defence Research Establishment

P O BOX 25
N0-2027 KJELLER, NORWAY

UNCLASSIFIED

SECURITY CLASSIFICATION OF THIS PAGE
(when data entered)

REPORT DOCUMENTATION PAGE

1) PUBL/REPORT NUMBER	2) SECURITY CLASSIFICATION	3) NUMBER OF PAGES
FFI/RAPPORT-2007/00842	UNCLASSIFIED	96
1a) PROJECT REFERENCE	**2a) DECLASSIFICATION/DOWNGRADING SCHEDULE**	
FFI-II/1013/912	-	

4) TITLE

ELECTROMAGNETIC SHADOW EFFECTS BEHIND WIND TURBINES

5) NAMES OF AUTHOR(S) IN FULL (surname first)

HØYE Gudrun

6) DISTRIBUTION STATEMENT

Approved for public release. Distribution unlimited. (Offentlig tilgjengelig)

7) INDEXING TERMS

IN ENGLISH:	IN NORWEGIAN:
a) Shadow effects	a) Skyggevirkning
b) Wind turbine	b) Vindmølle
c) Radar	c) Radar
d) Electromagnetic field	d) Elektromagnetisk felt
e)	e)

THESAURUS REFERENCE:

8) ABSTRACT

The development of wind farms may sometimes conflict with Defence interests by degrading the performance of Defence installations such as radars or telecommunications systems. This report has studied the potential problem with electromagnetic shadow effects behind the wind turbines.

The analyses have shown that there will be a shadow behind the wind turbine that is narrow (about 10 m wide) close to the turbine, but not very deep. At lower frequencies the shadow is wider and shallower, while at higher frequencies the shadow is narrower and deeper. The shadow increases in width and decreases in depth for increasing distance behind the wind turbine. For distances larger than 10 km the shadow depth is less than 3 dBV/m for all relevant frequencies. The radar's ability to detect targets will not be significantly affected by the shadow effects, except possibly for small targets that are close to the turbine.

The shadow effects calculations can be quite time consuming, especially for higher frequencies. A new set of equations has therefore been derived that can be used to quickly calculate the shadow boundary and depth behind a wind turbine.

9) DATE	AUTHORIZED BY	POSITION
	This page only	
2007-03-31	Vidar S Andersen	Director

ISBN 978-82-464-1149-1

UNCLASSIFIED

SECURITY CLASSIFICATION OF THIS PAGE
(when data entered)

CONTENTS

		Page
1	INTRODUCTION	7
2	THEORY	8
2.1	Wind turbines	8
2.2	Shadow effects behind wind turbines	10
2.3	The infinitely long conducting cylinder model	11
2.4	Boundary and depth of the shadow region	13
2.4.1	The shadow boundary equation	13
2.4.2	The shadow depth equation	14
3	LITERATURE STUDY	15
3.1	Paper I	15
3.2	Paper II	18
3.3	Paper III	24
3.4	Paper IV	28
3.5	Paper V	30
3.6	The cylinder radius	31
4	RESULTS	33
4.1	The electric field around an infinitely long conducting cylinder	34
4.2	The shadow boundary equation	35
4.3	The shadow depth equation	36
4.4	The angular dependency of the electric field	37
4.5	Cross-range cuts of the electric field	42
4.6	The radial dependency of the electric field	47
4.7	The shadow boundary and depth	52
5	DISCUSSION	53
5.1	The electric field around an infinitely long conducting cylinder	53
5.2	The shadow boundary equation	53
5.3	The shadow depth equation	54
5.4	The angular dependency of the electric field	54
5.5	Cross-range cuts of the electric field	55
5.6	The radial dependency of the electric field	55
5.7	The shadow boundary and depth	56
5.8	Shadow effects behind wind turbines	57

5.9 Summary 58

6 SUMMARY 59

APPENDIX

A THE INFINITELY LONG CONDUCTING CYLINDER MODEL 60

B BOUNDARY AND DEPTH OF THE SHADOW REGION 64

B.1 The shadow boundary equation 64

B.2 The shadow depth equation 69

C TERMINATION OF THE SUMMATION IN THE SECONDARY FIELD EQUATION 73

C.1 The secondary field equation 73
C.1.1 The coefficient a_m 74
C.1.2 The cosinus-factor 74
C.1.3 The Hankel-factor 75
C.1.4 The Bessel function 77

C.2 Method 78

C.3 Results 78
C.3.1 The secondary field as a function of *m* 78
C.3.2 Determining M 80

D MAPPING OF THE ELECTRIC FIELD AROUND THE WIND TURBINE 85

E IMPLEMENTATION OF THE SHADOW EFFECTS CALCULATIONS IN WTES 89

E.1 Generate Shadowing Pixmap.vi 90

E.2 Init Shadowing Cluster.ctl 92

E.3 Init Cluster.ctl 93

E.4 RADAR Settings.vi 93

E.5 RADAR Calculations.vi 94

References 96

ELECTROMAGNETIC SHADOW EFFECTS BEHIND WIND TURBINES

1 INTRODUCTION

There is at present a considerable interest in renewable energy sources, and a large number of onshore and offshore wind farms are currently under planning or being developed, both in Norway and in several other countries.

Figure 1.1 Wind farm in Magdeburg, Germany.

Wind turbines are large structures, and a wind farm typically consists of several turbines that are distributed over a wide area. Depending on location, the development of a wind farm in a particular area may conflict with Defence interests by degrading the performance of Defence installations such as radars or telecommunications systems. Forsvarets forskningsinstitutt (FFI) is currently looking into the matter through the FFI-project 1013 VINDKRAFT ("The effect of windmill development on telecommunication and radar").

One potential problem is the electromagnetic shadow that is cast behind a wind turbine when the wind turbine is illuminated by a radar. The shape and the strength of the shadow will depend on the radar frequency. This report studies the shadow effect, and draws some conclusions regarding its significance.

The outline of the report is as follows: Chapter 2 presents the theory for electromagnetic shadow effects behind wind turbines. In Chapter 3 a literature study is performed that forms the basis for a comparison with our findings. Chapter 4 presents the results of our calculations, and Chapter 5 gives an analysis of our findings. A summary is given in Chapter 6. Appendices A-C cover the theory for shadow effects in detail, while Appendices D-E present matter related to the implementation of the shadow effects in the software WTES (Wind Turbine and Electromagnetic Systems) (1) developed by the FFI-project 1013 VINDKRAFT.

2 THEORY

We will in this chapter present the theory for shadow effects behind wind turbines. We start by giving a description of the general features of wind turbines (Section 2.1), followed by a short introduction to the nature of electromagnetic shadowing (Section 2.2). In Section 2.3 we present the infinitely long conducting cylinder model that is used to represent the wind turbine, and in Section 2.4 we derive equations that can be used to quickly calculate the shadow boundary and depth behind a wind turbine.

2.1 Wind turbines

Wind turbines are large constructions that are significantly different from buildings and other structures in the terrain such as electricity pylons, large chimneys, etc. This difference is not only due to their physical size but also the shapes and materials used.

Typical modern turbines are of the horizontal axis type with three blades that rotate in the vertical plane. The electrical generation equipment is housed behind the blade-hub in an enclosed structure that can be rotated about the vertical axis to orientate the blades into the wind. The housing is mounted on the top of a cylindrical or gradually tapering tower usually of hollow steel construction. Figure 2.1 shows a photo of a wind turbine.

Figure 2.1 Photo of a typical wind turbine.

The wind turbine consists of three parts:

1) The tower
2) The nacelle
3) The blades

The tower height can vary from about 50 m for small wind turbines up to 120 m for large wind turbines. Corresponding blade lengths are 30-60 m. The total height of the wind turbine can reach 180 m for the largest turbines. Table 2.1 shows typical dimensions for different wind turbines.

	'mini'	'small'	'large'	'giant'
Tower Height [m]	50	60	100	120
Tower diameter @ base [m]	4	4.5	5	6
Tower diameter @ top [m]	2.5	3	4	5
Gondola [m x m x m]	5 x 2 x 3		8 x 3 x 4	
Blade length [m]	30	40	50	60
Total Height [m]	80	100	150	180
Length of first part of blade [m]	5.3	6.3	10	15
Maximal width of blade [m]	0.4 x 1.7	0.4 x 1.7	0.5 x 2.0	0.5 x 2.0

Table 2.1 Typical dimensions for wind turbines (Table 1 in (4)).

A wind farm consists of several wind turbines that are distributed over a large area. The turbines are separated by distances that are dictated by local terrain features and the desire to minimize the effect of airflow disturbances on successive turbines in the flow. Usually, the wind turbines are spaced 2-3 diameters apart in the cross-wind direction of the prevailing wind. Figure 2.2 shows a typical wind farm.

A Typical Wind Farm Cluster - Dun Law Wind Farm
Photo courtesy of Renewable Energy Systems

Figure 2.2 Example of a wind farm (Figure 3.1 in (8)).

2.2 Shadow effects behind wind turbines

Shadowing is a familiar phenomenon in daily life. Objects on the ground (buildings, cars, trees, persons, etc.) cast a clearly defined shadow behind them when lit by the sunlight, see Figure 2.3.

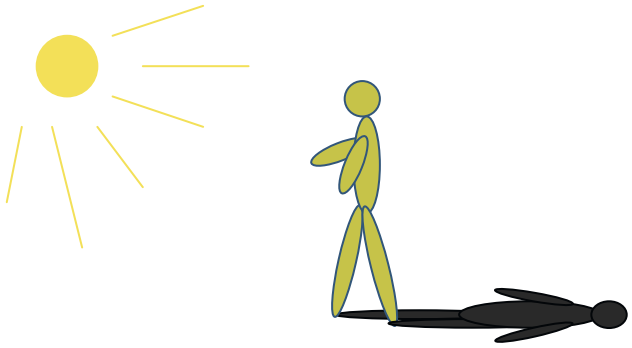

Figure 2.3 The shadow cast by a person standing in the sunlight.

Visible light from the sun has wavelengths in the range $\lambda = 400 - 800$ nm, while the physical dimension of objects that surround us is typically of the order of meters ($D \sim$ few meters). Hence, the wavelength of the incoming sunlight is much smaller than the size of the objects that cast the shadow, i.e., $\lambda \ll D$. In this case, the shadow cast behind the object has a clearly defined border. Inside the border the shadow is completely dark, while outside the border there is no shadow.

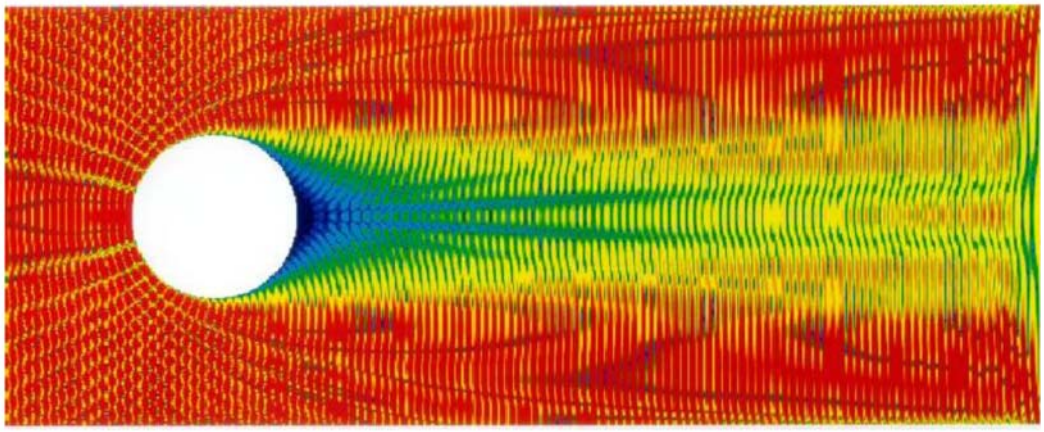

Figure 2.4 The shadow cast behind a cylinder that has dimensions of the same order as the wavelength of the incoming electromagnetic wave. Courtesy of EADS (5).

The electromagnetic waves emitted by radars have wavelengths in the range of centimeters to meters, while wind turbines have physical dimensions in the order of meters. The wavelength of the incoming electromagnetic wave is therefore of the same order as the size of the wind turbine, i.e., $\lambda \sim D$. In this case, the shadow behind the wind turbine will not be completely dark and will not have a clearly defined border. The reason for this is that the waves “bend”

around the wind turbine and partly penetrates into the shadow region behind the turbine. This is illustrated in Figure 2.4 and Figure 2.5.

The wind turbine has a complex shape and different parts may contribute differently to the shadow effect. To simplify the calculations we will assume that the tower is the main source of the shadowing, and that the contribution from the nacelle and the blades can be neglected. The tower can be modelled as an infinitely long conducting cylinder, and the infinitely long conducting cylinder model will be presented in the following section.

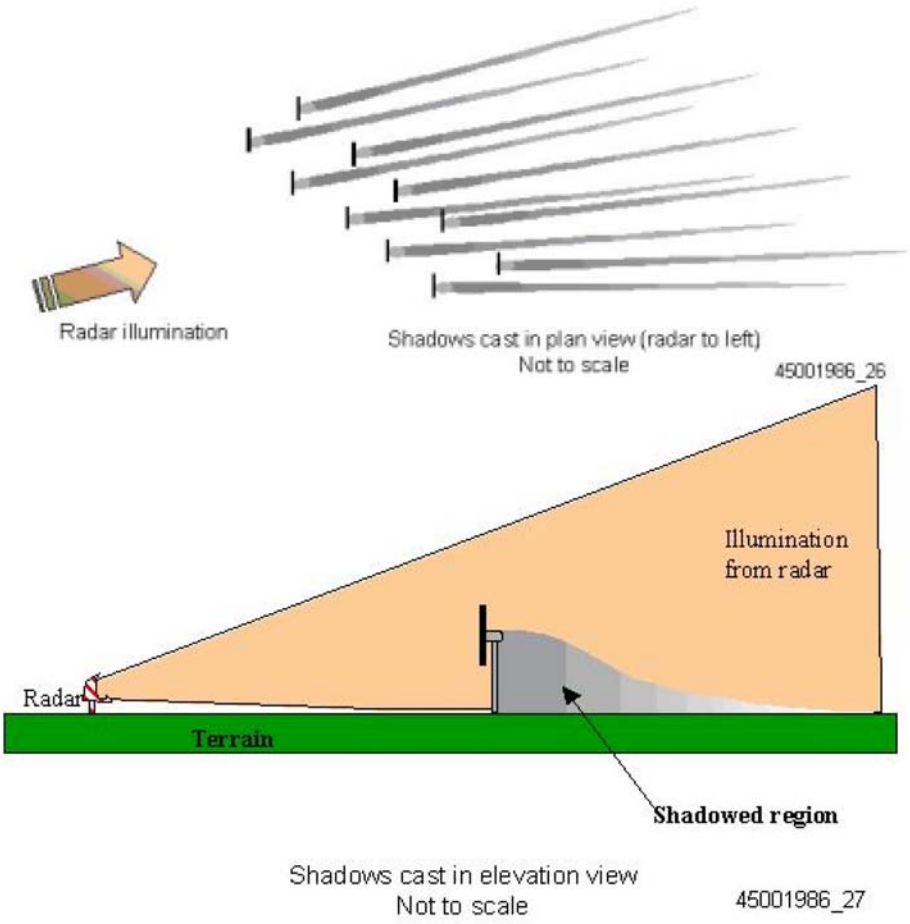

Figure 3.4 Shadowing of the Space Behind Turbines

Figure 2.5 The electromagnetic shadow cast behind a wind turbine (Figure 3.4 in (8)).

2.3 The infinitely long conducting cylinder model

In the infinitely long conducting cylinder model the wind turbine is modelled as an infinitely long conducting cylinder with radius r_{cyl}. The incoming (from the radar) electromagnetic primary wave E_z^{prim} is assumed to be a plane wave with electric field component along the z-axis only. It is also assumed that the electric field is homogeneous in the z-direction. The problem can then be solved in 2 dimensions. The geometry of the problem is shown in Figure 2.6.

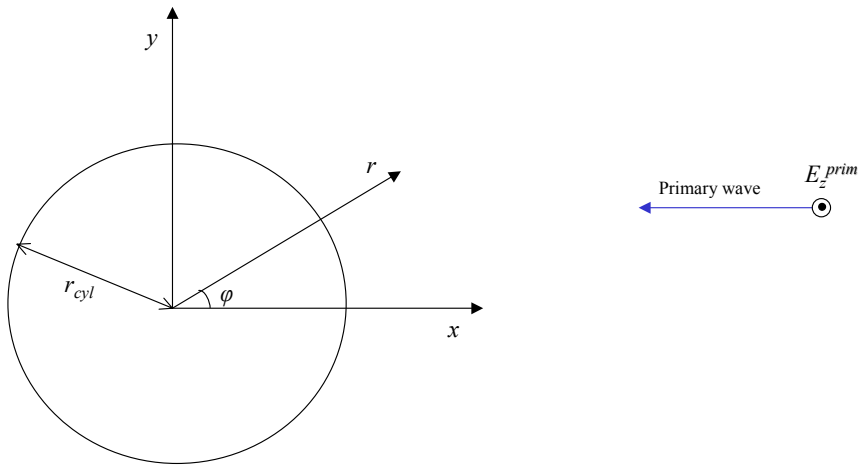

Figure 2.6 Diffraction on an infinitely long conducting cylinder (cross-section in the xy-plane).

The total electric field E_z^{tot} around the cylinder is given by

$$E_z^{tot} = E_z^{prim} + E_z^{\sec} \tag{2.1}$$

Here E_z^{prim} is the incoming primary field

$$E_z^{prim} = E_0 e^{jkr\cos\varphi} \tag{2.2}$$

where E_0 is the electric field amplitude, r is the distance from the cylinder, φ is the angle around the cylinder, and $k = 2\pi/\lambda$ is the wave number with λ being the wavelength.

$E_z^{\sec}$ is the secondary field that is generated by the cylinder in response to the incoming field

$$E_z^{\sec} = \sum_{m=0}^{\infty} A_m H_m^{(2)}(kr)\cos(m\varphi) \tag{2.3}$$

Here $H_m^{(2)}$ are Hankel functions of the second kind, and the coefficients A_m are given by

$$A_0 = -\frac{E_0 J_0(kr_{cyl})}{H_0^{(2)}(kr_{cyl})} \tag{2.4}$$

and

$$A_m = -2j^m E_0 \frac{J_m(kr_{cyl})}{H_m^{(2)}(kr_{cyl})} \tag{2.5}$$

The summation in Equation (2.3) for the secondary field can be terminated when $m = M$, where M is given by

$$M = \mathrm{ceil}\left[10 + 6.4 \cdot \left(\frac{r_{cyl}}{\lambda}\right)\right] \tag{2.6}$$

Equation (2.6) is valid for $r_{cyl} / \lambda \le 1000$.

2.4 Boundary and depth of the shadow region

The boundary and depth (reduction in the electric field) of the shadow region can be determined from Equations (2.1)-(2.5). This may, however, be time consuming especially for high frequencies where the number of terms that must be included in the summation in Equation (2.3) is large. We have therefore derived separate equations that can be used to quickly calculate the shadow boundary and depth. Details can be found in Appendix B.

2.4.1 The shadow boundary equation

We define the shadow boundary to be the closest cross-range distance Y_b, at given distance d behind the cylinder, where the total electric field E_z^{tot} is equal to the unperturbed electric field, i.e., where there is no shadow. The shadow boundary can then be calculated from (see Appendix B.1)

$$Y_b = \pm \begin{cases} y_b(d), & d > d_0 \\ r_{cyl} + \left(\dfrac{y_b(d_0) - r_{cyl}}{d_0}\right) \cdot d, & d \le d_0 \end{cases} \tag{2.7}$$

where

$$y_b(d) = \sqrt{\frac{d \cdot r_{cyl}}{w}} \tag{2.8}$$

and

$$d_0 = \begin{cases} 5r_{cyl} \cdot \left(\dfrac{r_{cyl}}{\lambda}\right), & \dfrac{r_{cyl}}{\lambda} > 1 \\ 5r_{cyl}, & \dfrac{r_{cyl}}{\lambda} \le 1 \end{cases} \tag{2.9}$$

Here r_{cyl} is the cylinder radius, λ is the wavelength, and w is given by

$$w = g \cdot \left(\frac{r_{cyl}}{\lambda}\right)^k \tag{2.10}$$

where g and k are two constants given by

$$\begin{aligned} g &= 1.6 \\ k &= 0.96 \end{aligned} \tag{2.11}$$

2.4.2 The shadow depth equation

The shadow depth can be calculated from (see Appendix B.2)

$$20 \lg E_z^{tot} = a \cdot \left(\frac{d}{r_{cyl}} \right)^{-b} \tag{2.12}$$

where r_{cyl} is the cylinder radius, d is the distance behind the cylinder, and a is given by

$$a = u \cdot \left(\frac{r_{cyl}}{\lambda} \right)^{s} \tag{2.13}$$

where λ is the wavelength, and u and s are two constants given by

$$\begin{aligned} u &= -27.714 \\ s &= 0.22298 \end{aligned} \tag{2.14}$$

The parameter b is given by

$$\lg b = q_3 \cdot \left[\lg\left(r_{cyl} / \lambda \right) \right]^3 + q_2 \cdot \left[\lg\left(r_{cyl} / \lambda \right) \right]^2 + q_1 \cdot \lg\left(r_{cyl} / \lambda \right) + q_0 \tag{2.15}$$

where the coefficients $q_0 - q_3$ have the following values

$0.1 \le \frac{r_{cyl}}{\lambda} \le 10$:

$$\begin{aligned} q_0 &= -0.2395 \\ q_1 &= -0.02645 \\ q_2 &= -0.01852 \\ q_3 &= -0.003527 \end{aligned} \tag{2.16}$$

and

$10 < \frac{r_{cyl}}{\lambda} \le 1000$:

$$\begin{aligned} q_0 &= -0.2395 \\ q_1 &= \ \ 0.01692 \\ q_2 &= -0.08798 \\ q_3 &= \ \ 0.02256 \end{aligned} \tag{2.17}$$

3 LITERATURE STUDY

We have studied the available literature on shadow effects behind wind turbines. The purpose was to evaluate the validity of our use of the infinitely long conducting cylinder model for the wind turbine and to be able to adjust the parameters in the model so that it represents the reality as closely as possible.

The following papers were included in the study:

Paper I: C Samela, C Fernandes, L Fauro: *TV Interference from Wind Turbines*.

Paper II: J G Gallagher (2003): *Radio frequency and radar shadowing, The impact of Robin Wigg wind turbines on maritime radio frequency systems*, Technical report, QINETIQ/S&E/SPS/TR030449.

Paper III: D Trappeniers and E Van Lil (2005): *Computation of the effects of wind turbines on aeronautical radar and communication systems*, Version 8, 29-07-2005, Belgocontrol.

Paper IV: A. Frye and B. D. Bloch (2003): *Final report: Effect of obstacles on HF-supported guidance systems, Follow-up study,* EADS Deutschland GmbH.

Paper V: M Howard and C Brown (2004): *Results of the electromagnetic investigations and assessments of marine radar, communications and positioning systems undertaken at the North Hoyle wind farm by QinetiQ and the Maritime and Coastguard Agency*, QinetiQ/03/00297/1.1, MCA MNA 53/10/366, 22 November 2004.

3.1 Paper I

Paper I studies the TV interference from wind turbines (7).

The wind turbine is modelled as an infinitely long conducting cylinder with radius $r_w = 1.5$ m. The cylinder is illuminated by an incoming plane wave that is normal to the surface of the cylinder. The generated secondary field is calculated from (Equation (1) in (7))

$$ {}^{I}E_z^{\sec} = E_0 \left[\frac{J_0(kr_{cyl})}{H_0^{(2)}(kr_{cyl})} H_0^{(2)}(kr) + 2\sum_{m=0}^{\infty} (-j)^m \frac{J_m(kr_{cyl})}{H_m^{(2)}(kr_{cyl})} H_m^{(2)}(kr)\cos(m\varphi) \right] \tag{3.1} $$

with the primary field given by ${}^{I}E_z^{prim} = E_0 e^{-jkr\cos\varphi}$. This corresponds to Equations (2.2)-(2.5) in this report if substituting $-j$ by $+j$ in the expressions for the primary and secondary fields

above[1]. Note also the opposite sign of the secondary field ${}^{I}E_z^{\sec}$ (compared to Equation (2.3)). This means that the total field ${}^{I}E_z^{tot}$ is given by

$$ {}^{I}E_z^{tot} = {}^{I}E_z^{prim} - {}^{I}E_z^{\sec} \tag{3.2}$$

Paper I presents a plot of the electric field around the cylinder at 100 MHz (see Figure 3.1 in this report) together with numbers for the electric field at different frequencies and distances behind the cylinder (see Table 3.1 in this report). We have performed the same calculations for comparison. Figure 3.2 and Table 3.1 show the results.

Figure 3.1 (paper I) and Figure 3.2 (our calculations) show the electric field behind the cylinder at 100 MHz. We see that there is good agreement between the two figures. Both show similar patterns of light (high electric field) and dark (low electric field) areas. This is as expected, since the same model (infinitely long conducting cylinder) was used in both cases. Differences in dynamic range in the two figures may be explained by the use of different grid resolution during the calculations and /or different choice of cut-off value for the dynamic range.

Table 3.1 shows the maximum reduction in the electric field at different frequencies and distances behind the cylinder as calculated by paper I for a cylinder radius of r_w=1.5 m. The corresponding numbers calculated by us are given in parentheses. The last column in the table shows the cylinder radius r_{cyl} that we would use in our calculations to obtain the same results as paper I. We see that for both 100 MHz and 1 GHz there is reasonably good agreement between the numbers calculated by us and those calculated by paper I.

Frequency	**Distance**	**Maximum reduction in electric field**	**r_w**	**r_{cyl}**
100MHz	100m	<3dBV/m (2.2dBV/m)	1.5m	<2.1m
1GHz	100m	8.5dBV/m (6.2dBV/m)	1.5m	2.0m

Table 3.1 Maximum reduction in the electric field for given frequency and distance behind the cylinder. The column marked r_w shows the cylinder radius used by paper I for the calculations, while the column marked r_{cyl} shows the cylinder radius used in this report to obtain the same values. Numbers in parentheses show the results for the maximum reduction in the electric field when we use $r_{cyl}= r_w$.

[1] Using $-j$ (paper I) instead of $+j$ (this report) in the expressions for the primary and secondary fields corresponds to reversing the directions of the field. Therefore, when using $-j$ the angle φ=0 corresponds to "behind" the cylinder as opposed to $\varphi=\pi$ when using $+j$ in the equations.

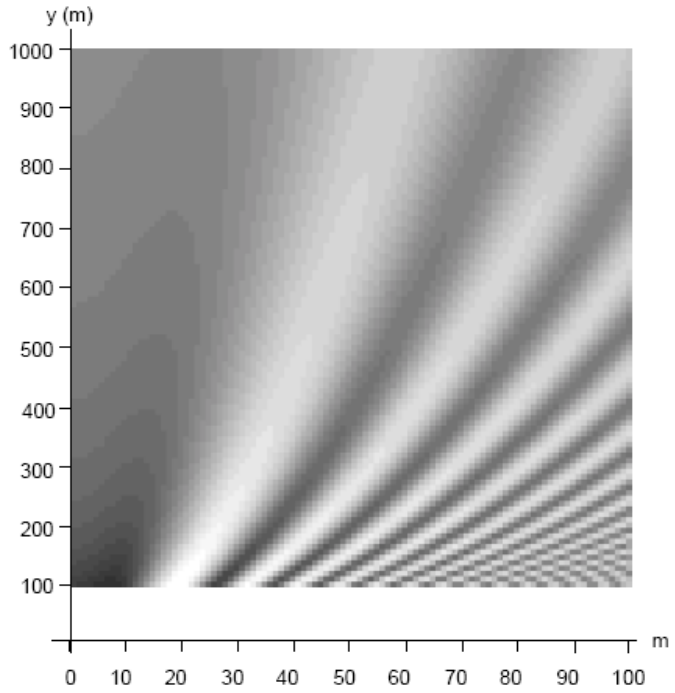

Fig. 2. Density plot of the total field E around a vertical infinite cylinder with $r = 1.5$ m at 100 MHz.

Figure 3.1 *Figure 2 in (7) showing the electric field behind an infinitely long conducting cylinder with radius 1.5 m at 100 MHz. The cylinder is situated in the lower left corner of the figure, and the incoming electromagnetic plane wave moves in the +y-direction. Range; –3 dBV/m (black) to 1.5 dBV/m (white).*

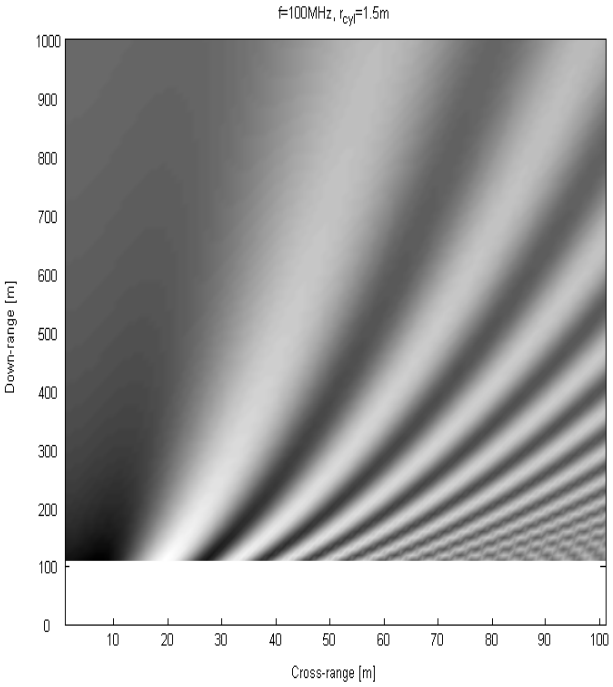

Figure 3.2 *The electric field behind an infinitely long conducting cylinder with radius 1.5 m at 100 MHz (compare with Figure 3.1). The cylinder is situated in the lower left corner of the figure, and the incoming electromagnetic plane wave moves in the +y-direction. Range; –2.1 dBV/m (black) to 1.6 dBV/m (white).*

3.2 Paper II

Paper II studies the impact of wind turbines on radio frequency systems (6).

The wind turbine is modelled as a perfectly conducting cylinder with radius $r_w = 2.6$ m. The cylinder is illuminated by an incoming plane wave that is normal to the surface of the cylinder. Paper II does not give the equations that the calculations are based on. However, for an *infinitely* long perfectly conducting cylinder the equations should be the same as Equations (2.1)-(2.5) in this report. Paper II does not, however, specifically state that the cylinder is infinitely long.

Paper II presents plots of the reduction in echo strength behind the cylinder at 9.4 GHz (Figure 3.3 and Figure 3.5 in this report) together with several figures showing the corresponding cross-range cuts at different distances behind the cylinder (Figure 3.7, Figure 3.9, and Figure 3.11 in this report). Numbers for the reduction in echo strength at different frequencies and distances behind the cylinder are also given (see Table 3.2 in this report). We have performed the same calculations for comparison. Figure 3.4, Figure 3.6, Figure 3.8, Figure 3.10, Figure 3.12, and Table 3.2 show the results.

Figure 3.3 and Figure 3.5 (paper II) and Figure 3.4 and Figure 3.6 (our calculations) show the reduction in echo strength behind the cylinder at 9.4 GHz. We see that there is good agreement between the figures, showing similar patterns for the reduction in echo strength. This is as expected, since the same model (perfectly conducting cylinder) was used in both cases. Differences in dynamic range in the figures may be explained by the use of different grid resolution during the calculations and/or different choice of cut-off value for the dynamic range.

Figure 3.7, Figure 3.9, and Figure 3.11 (paper II) and Figure 3.8, Figure 3.10, and Figure 3.12 (our calculations) show cross-range cuts of the reduction in echo strength at 9.4 GHz at different distances behind the cylinder. We see that there is good agreement between our results and the results of paper II. The shape of the curves is similar, and the width and depth of the shadow region behind the cylinder (around $y = 0$) are of the same size.

Table 3.2 shows the reduction in echo strength for given frequency and distance behind the cylinder as calculated by paper II for a cylinder radius of r_w=2.6 m. The corresponding numbers calculated by us are given in parentheses. The last column in the table shows the cylinder radius r_{cyl} that we would use in our calculations to obtain the same values as paper II. At 9.4 GHz and a distance of 1000 m behind the cylinder our results for the reduction in echo strength (11-21 dBs) agree well with the results found by paper II (10-20 dBs). At 2000 m behind the wind turbine paper II gives an order of size estimate for the reduction in echo strength (~ 10 dBs), and this value falls well inside the range calculated by us (8-14 dBs). We conclude that there is good agreement between our results and the results of paper II.

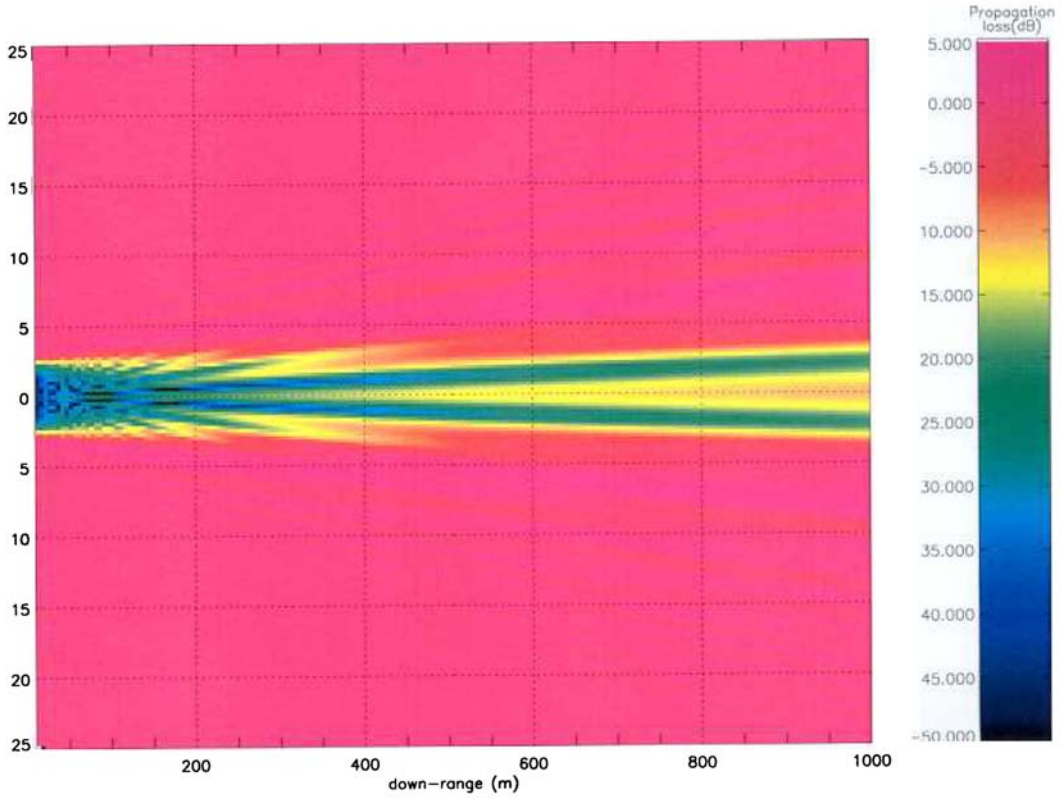

Figure 3.3 *Figure 1 in (6) showing the reduction in echo strength behind a conducting cylinder with radius 2.6 m at 9.4 GHz. Range; -50dBs (dark blue) to 5 dBs (red).*

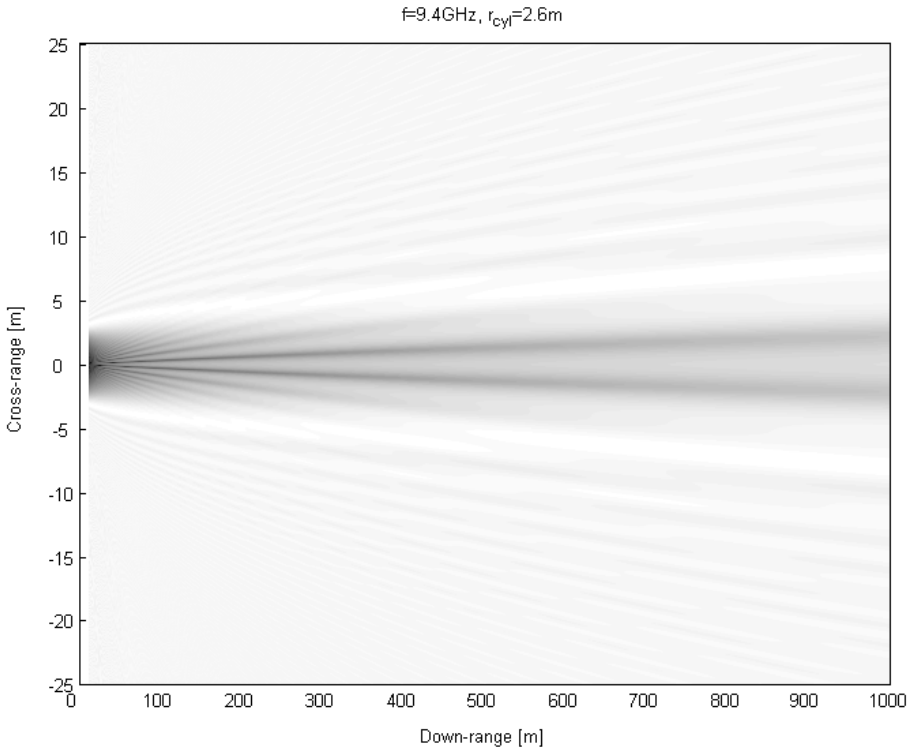

Figure 3.4 *Reduction in echo strength behind an infinitely long conducting cylinder with radius 2.6 m at 9.4 GHz (compare with Figure 3.3). Range; –105 dBs (black) to 4 dBs (white).*

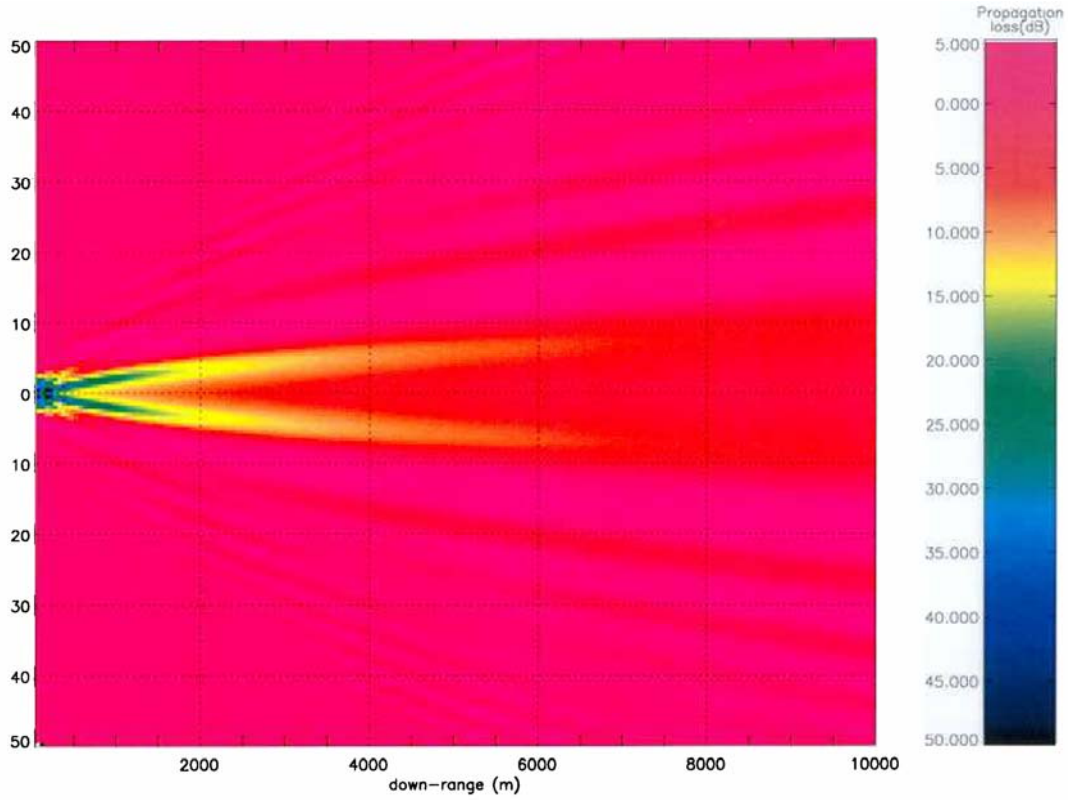

Figure 3.5 *Figure 2 in (6) showing the reduction in echo strength behind a conducting cylinder with radius 2.6 m at 9.4 GHz. Range; -50dBs (dark blue) to 5 dBs (red).*

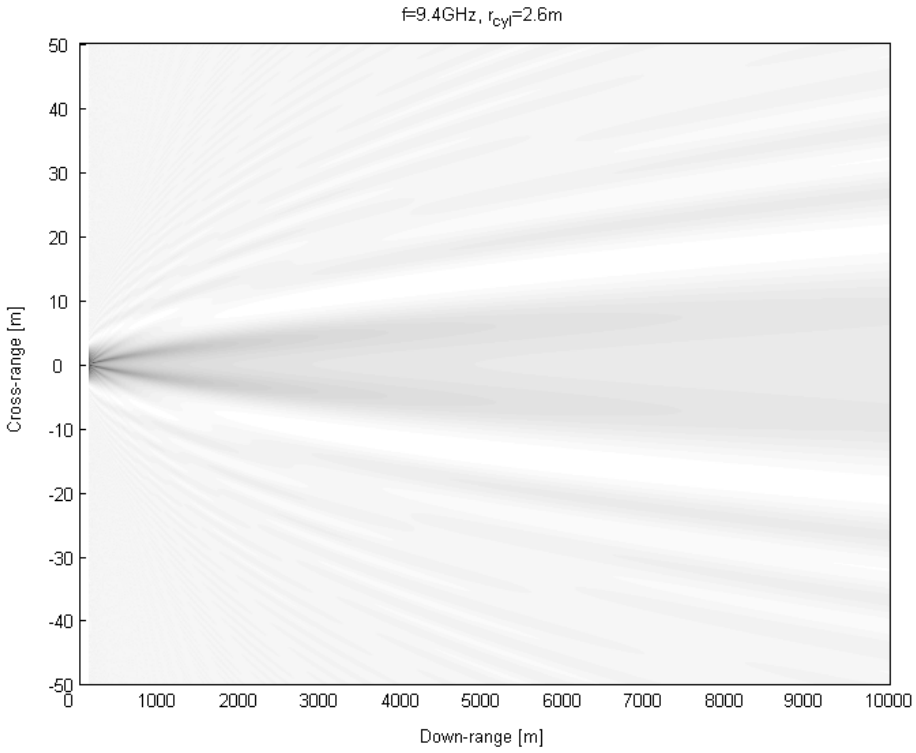

Figure 3.6 *Reduction in echo strength behind an infinitely long conducting cylinder with radius 2.6 m at 9.4 GHz (compare with Figure 3.5). Range; -99 dBs (black) to 5 dBs (white).*

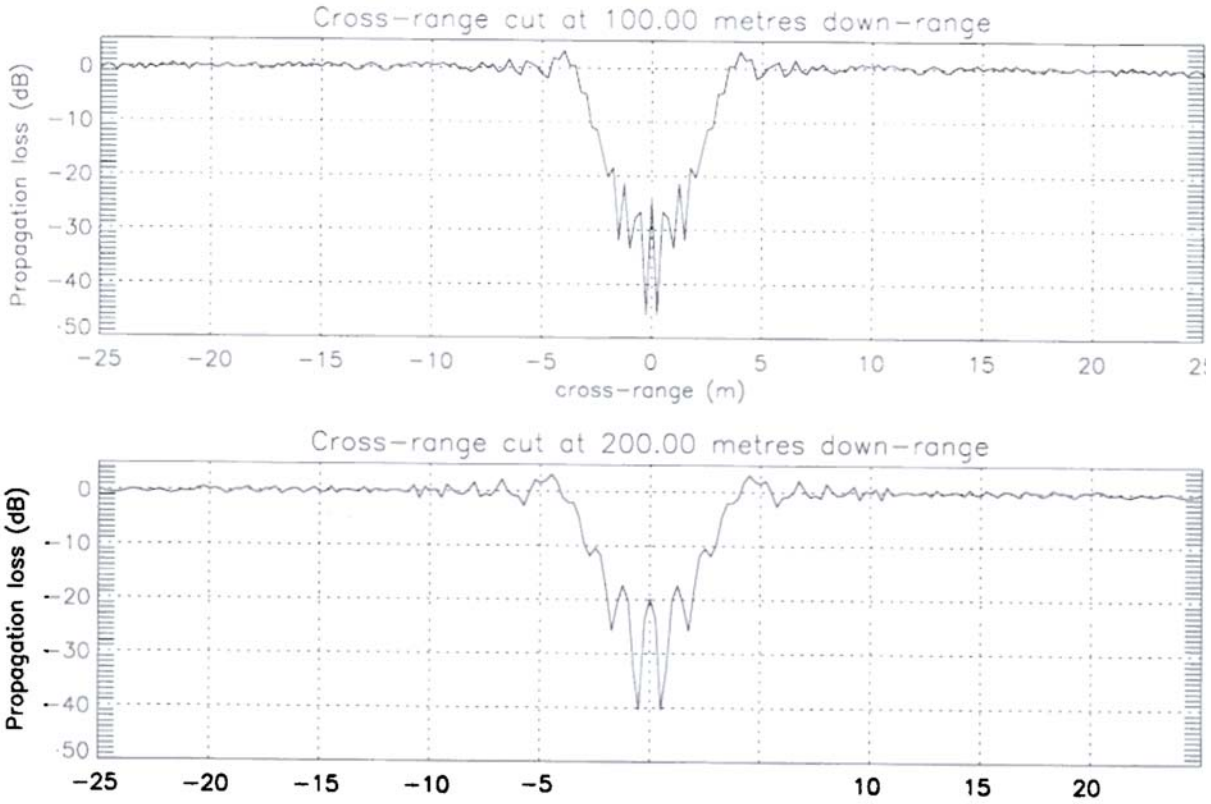

Figure 3.7 *Figure 3 in (6) showing cross-range cuts of the reduction in echo strength at 100 m and 200 m behind a conducting cylinder with radius 2.6 m at 9.4 GHz.*

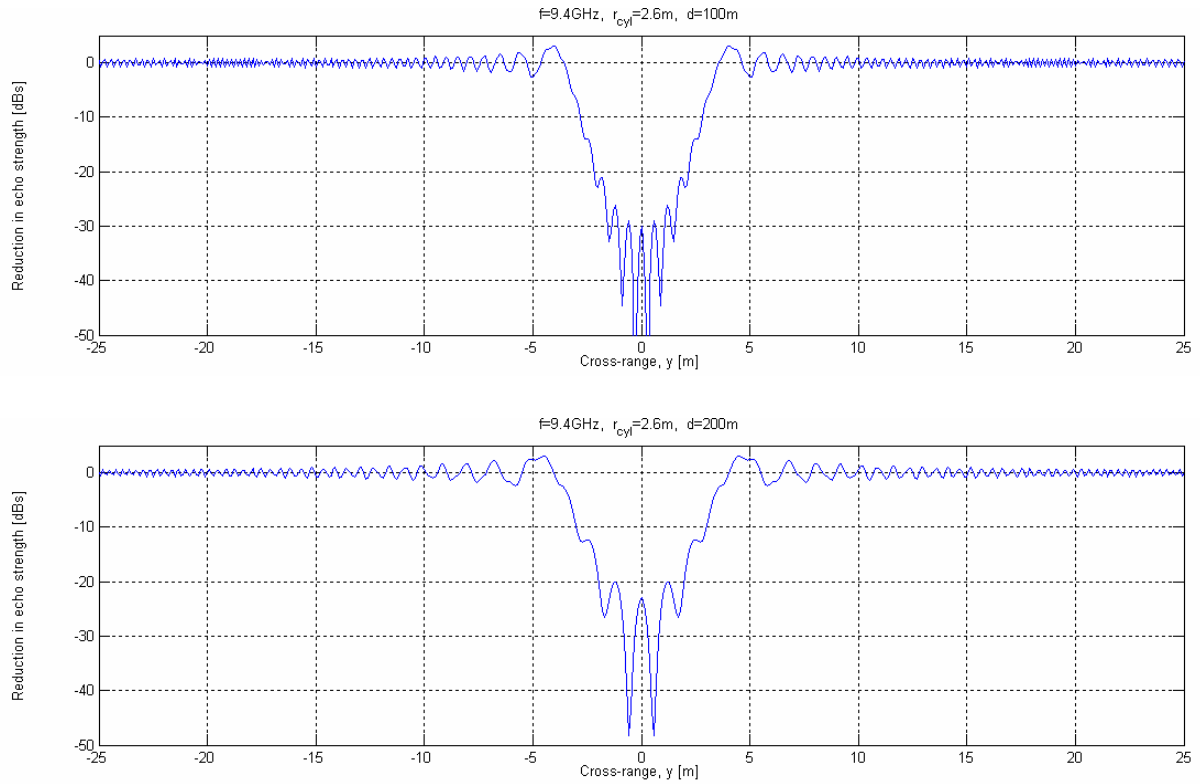

Figure 3.8 *Cross-range cuts of the reduction in echo strength at 100 m and 200 m behind an infinitely long conducting cylinder with radius 2.6 m at 9.4 GHz (compare with Figure 3.7).*

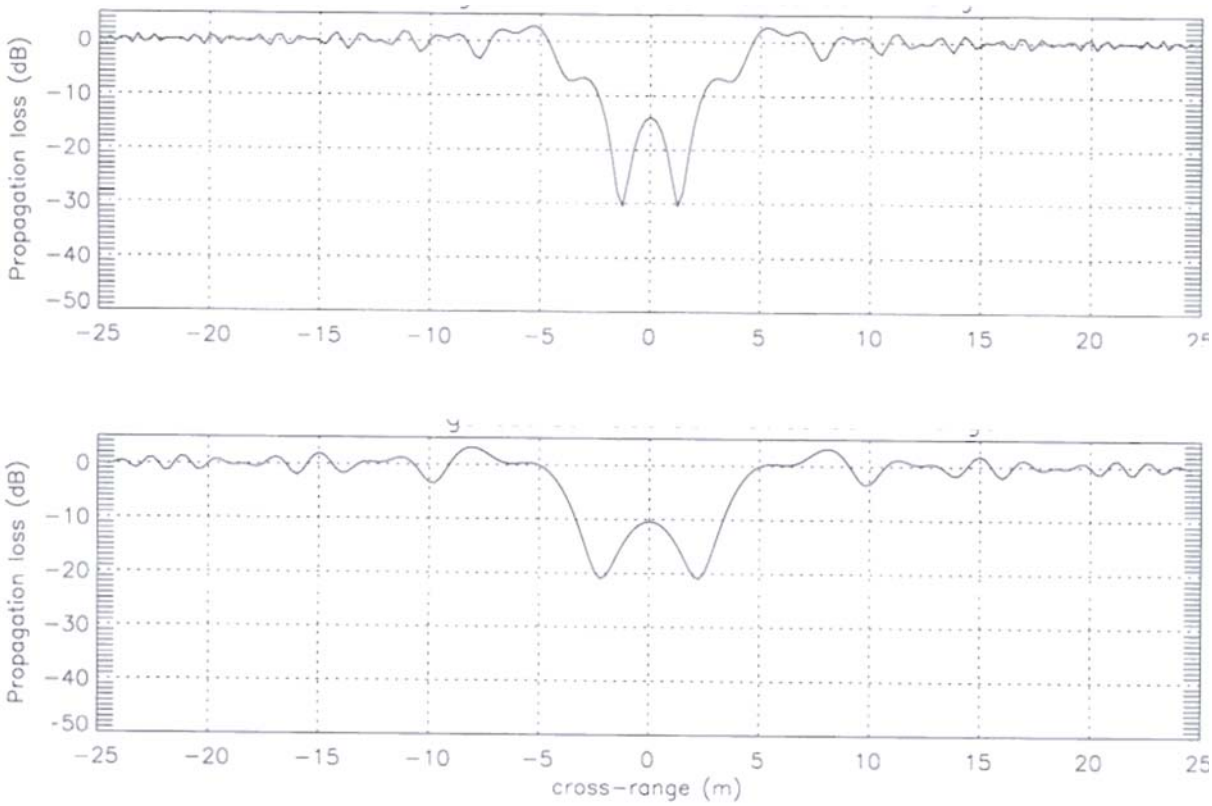

Figure 3.9 *Figure 3 in (6) showing cross-range cuts of the reduction in echo strength at 500 m and 1000 m behind a conducting cylinder with radius 2.6 m at 9.4 GHz.*

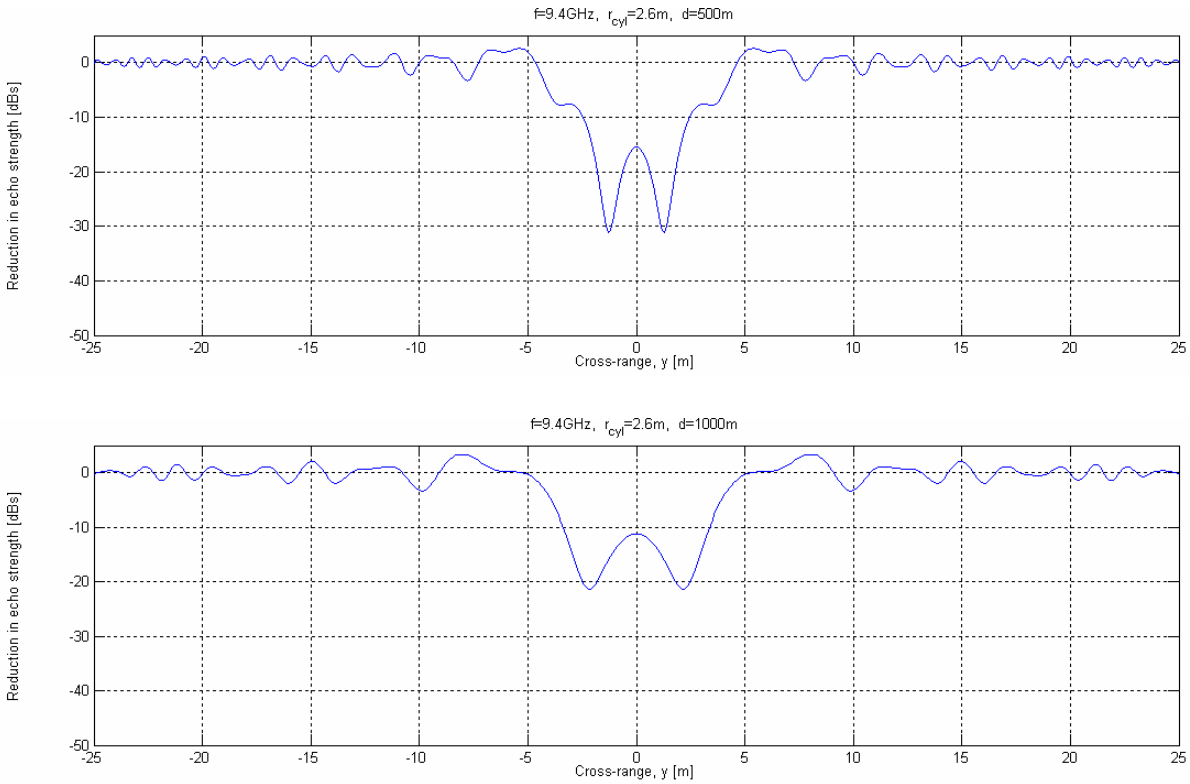

Figure 3.10 *Cross-range cuts of the reduction in echo strength at 500 m and 1000 m behind an infinitely long conducting cylinder with radius 2.6 m at 9.4 GHz (compare with Figure 3.9).*

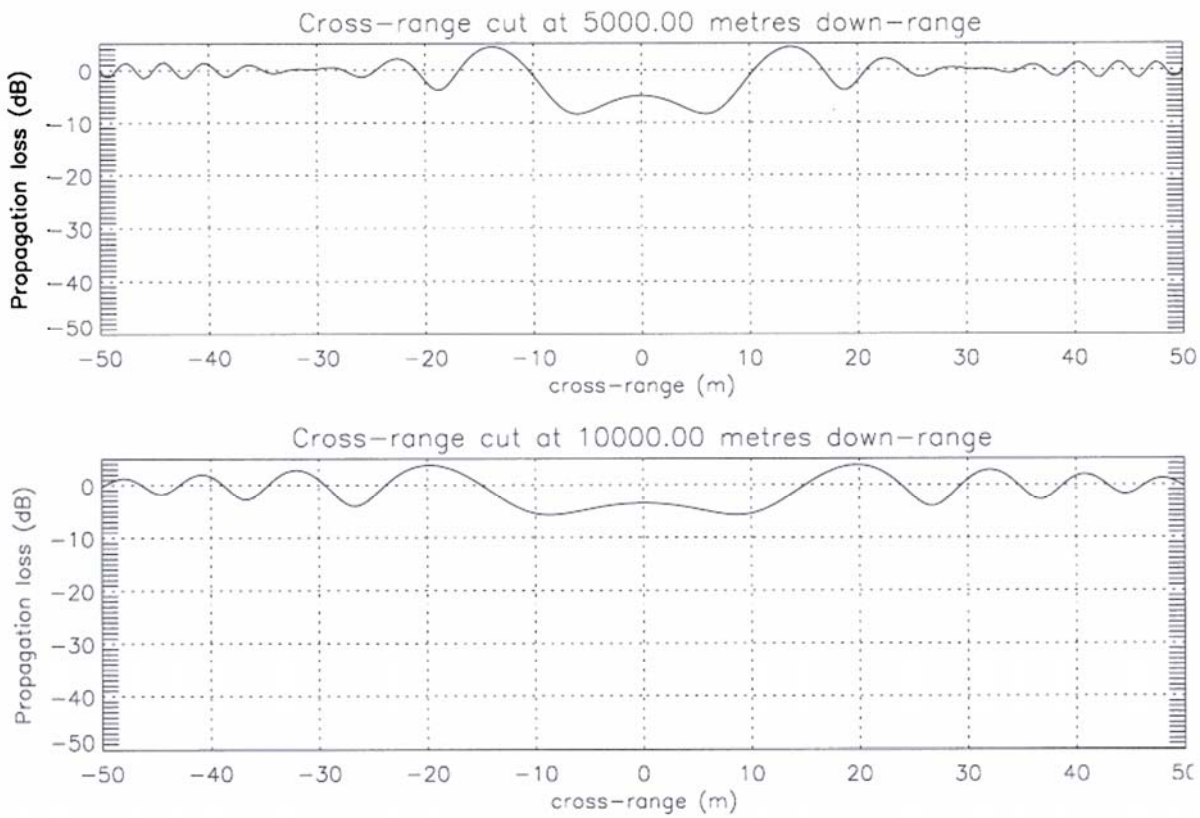

Figure 3.11 Figure 4 in (6) showing cross-range cuts of the reduction in echo strength at 5000m and 10000m behind a conducting cylinder with radius 2.6 m at 9.4 GHz.

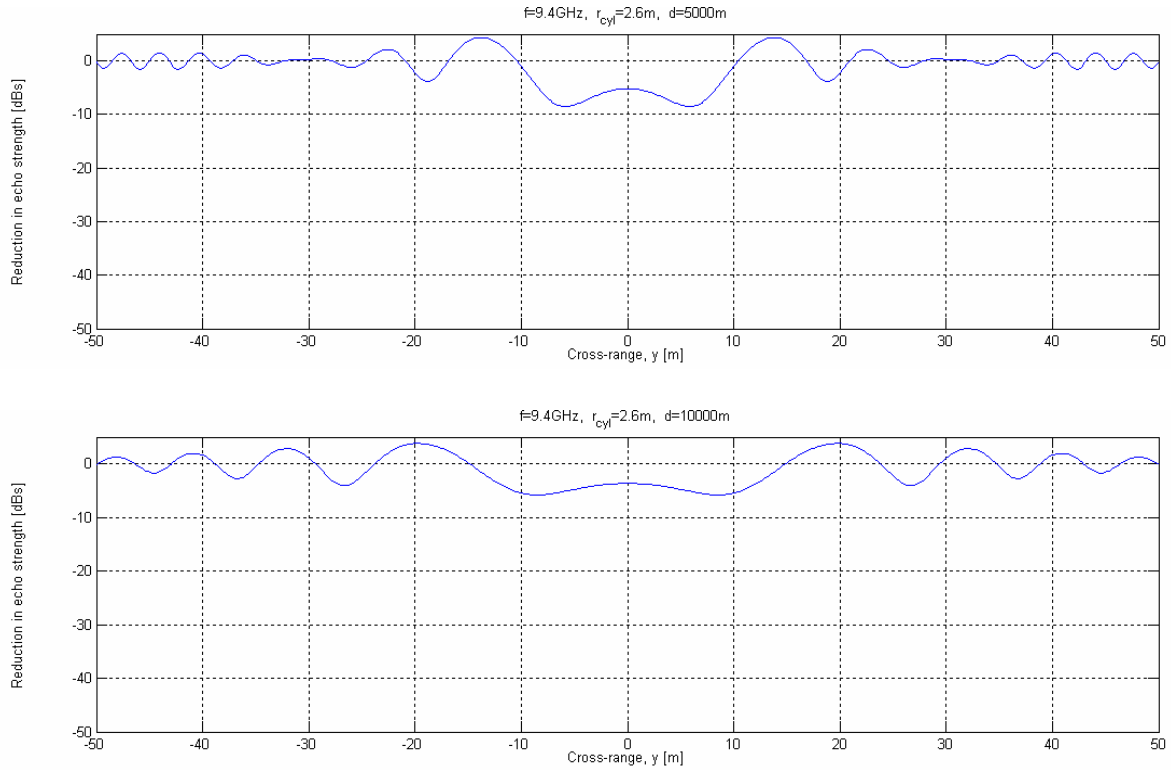

Figure 3.12 Cross-range cuts of the reduction in echo strength at 5000 m and 10000 m behind an infinitely long conducting cylinder with radius 2.6 m at 9.4 GHz (compare with Figure 3.11).

Frequency	Distance	Reduction in echo strength	r_w	r_{cyl}
9.4GHz	1000m	10-20dBs (11-21dBs)	2.6m	2.6m
9.4GHz	2000m	~ 10dBs (8-14dBs)	2.6m	2.6m

Table 3.2 *Reduction in echo strength for given frequency and distance behind the cylinder. The column marked r_w shows the cylinder radius used by paper II for the calculations, while the column marked r_{cyl} shows the cylinder radius used in this report to obtain the same values. Numbers in parentheses show the results for the reduction in echo strength when we use $r_{cyl} = r_w$.*

3.3 Paper III

Paper III studies the effects of wind turbines on aeronautical radars and communication systems (4).

The calculations in paper III are based on geometric-optical diffraction theory, inclusive slope diffraction. The tower base is approximated by a polygon with 17 sides (heptadecahedron), and it is assumed that its outer side planes are perfectly conducting. The rotor blades are tilted 6° and are assumed to have perfectly conducting outer surfaces. Figure 3.13 shows two of the wind turbine models that are used in paper III.

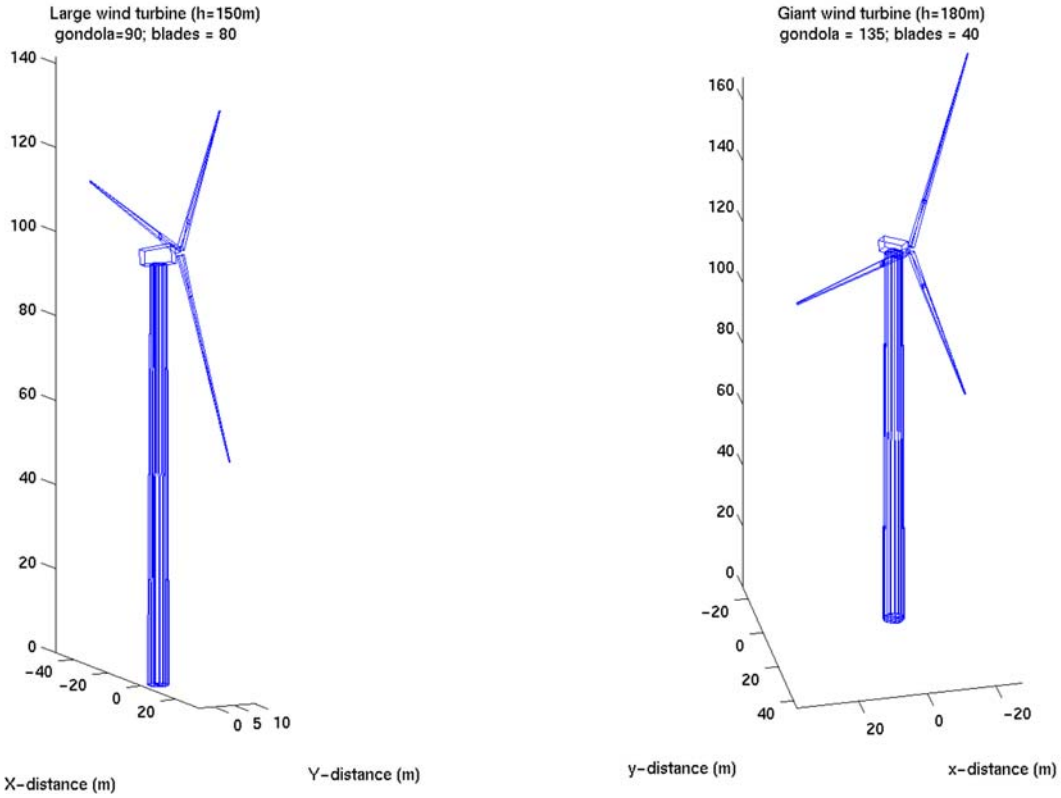

Figure 3.13 *Figure 2 in (4) showing the geometric implementation of a "large" (left figure) and "giant" (right figure) wind turbine.*

Paper III presents a plot of the reduction in echo strength behind a large wind turbine with radius $r_w = 3$ m at 9.065 GHz (Figure 3.14 in this report). It also presents a corresponding cross-range cut at a distance 900 m behind the wind turbine (Figure 3.16 in this report).We have performed the same calculations for comparison. Figure 3.15 and Figure 3.17 show the results.

Figure 3.14 (paper III) and Figure 3.15 (our calculations) show the reduction in echo strength at 9.065 GHz behind respectively a large wind turbine and an infinitely long conducting cylinder, both with radius 3 m. We see that there is good agreement between the two figures, showing similar patterns for the reduction in echo strength. Differences in the dynamic range in the figures may be explained by use of different grid resolution during the calculations and/or different choice of cut-off value for the dynamic range.

Figure 3.16 (paper III) and Figure 3.17 (our calculations) show the corresponding cross-range cuts at a distance 900 m behind respectively the wind turbine and the cylinder. We see that there is a good overall agreement between the two figures. The shape of the curve is similar, but some differences can be seen in the actual values for the reduction in echo strength. The most noticeable is the more shallow "dips" in our curve (Figure 3.17) around $y = \pm 2$ m reaching down to only about -26 dBs as opposed to –37 dBs for the curve presented in paper III (Figure 3.16). The placement of the "dips" (at $y = \pm 2$ m), however, is the same. Note also that our curve in general shows less reduction in the echo strength than the curve presented in paper III for all values of y.

We also calculated cross-range cuts for cylinder radii both smaller and larger than $r_{cyl} = 3$ m. For $r_{cyl} < 3$ m the reduction in the echo strength became smaller (less shadow) and the "dips" in the curve were placed further away from the center, while for $r_{cyl} > 3$ m the reduction in the echo strength became larger (more shadow) and the "dips" in the curve were placed closer to the center. We found that a cylinder radius of $r_{cyl} = 3$ m corresponded best to the results obtained by paper III.

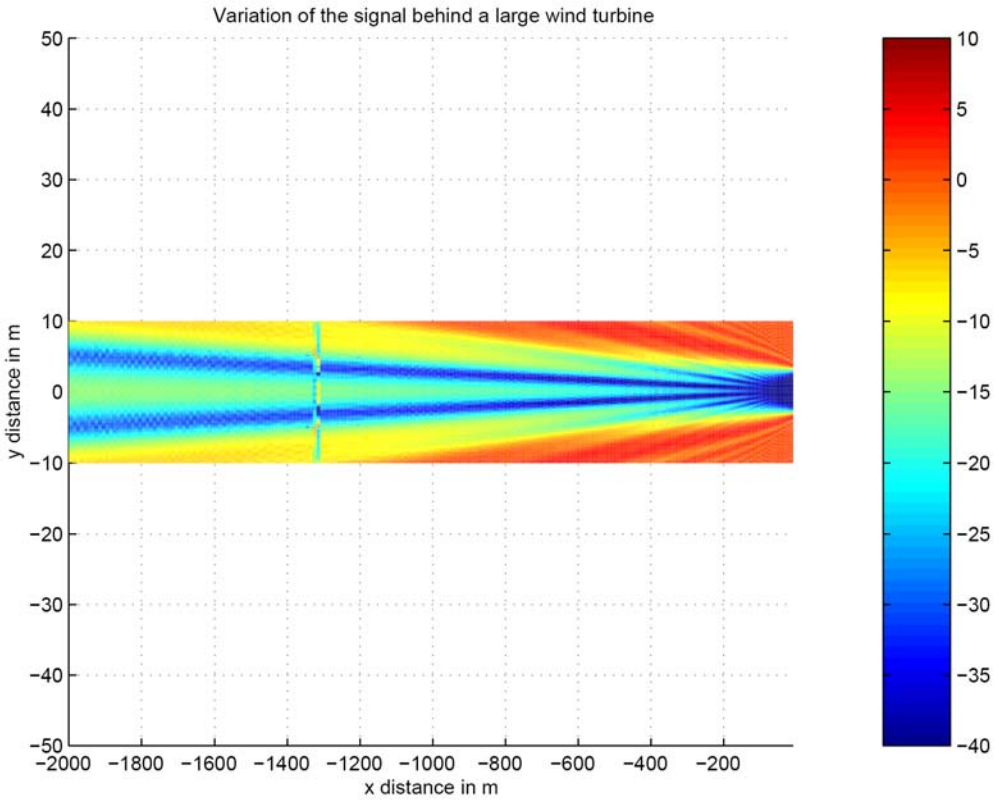

Figure 3.14 *Figure 8 in (4) showing the reduction in echo strength behind a wind turbine with radius 3 m at 9.065 GHz. Range; -40 dBs (dark blue) to 10 dBs (dark red).*

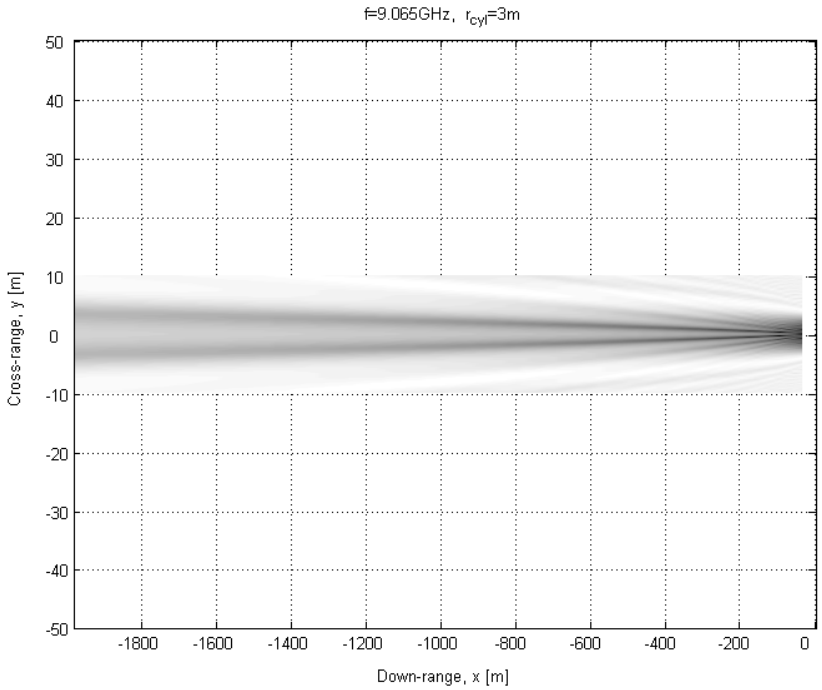

Figure 3.15 *Reduction in echo strength behind an infinitely long conducting cylinder with radius 3 m at 9.065 GHz (compare with Figure 3.14). Range; –69 dBs (black) to 4 dBs (white).*

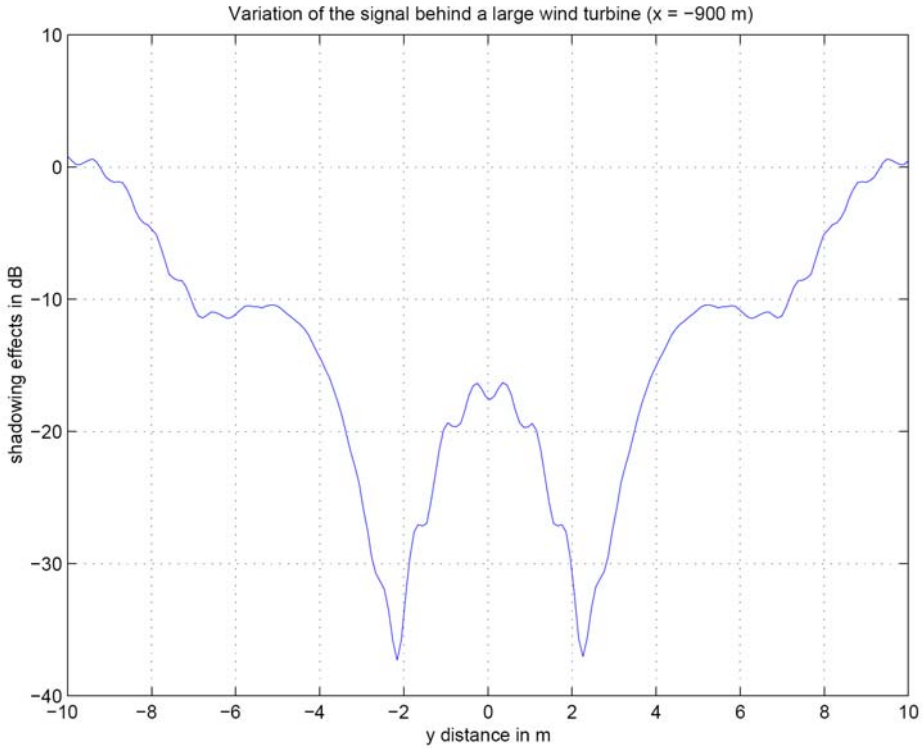

Figure 3.16 *Figure 9 in (4) showing a cross-range cut of the reduction in echo strength 900 m behind a wind turbine with radius 3 m at 9.065 GHz.*

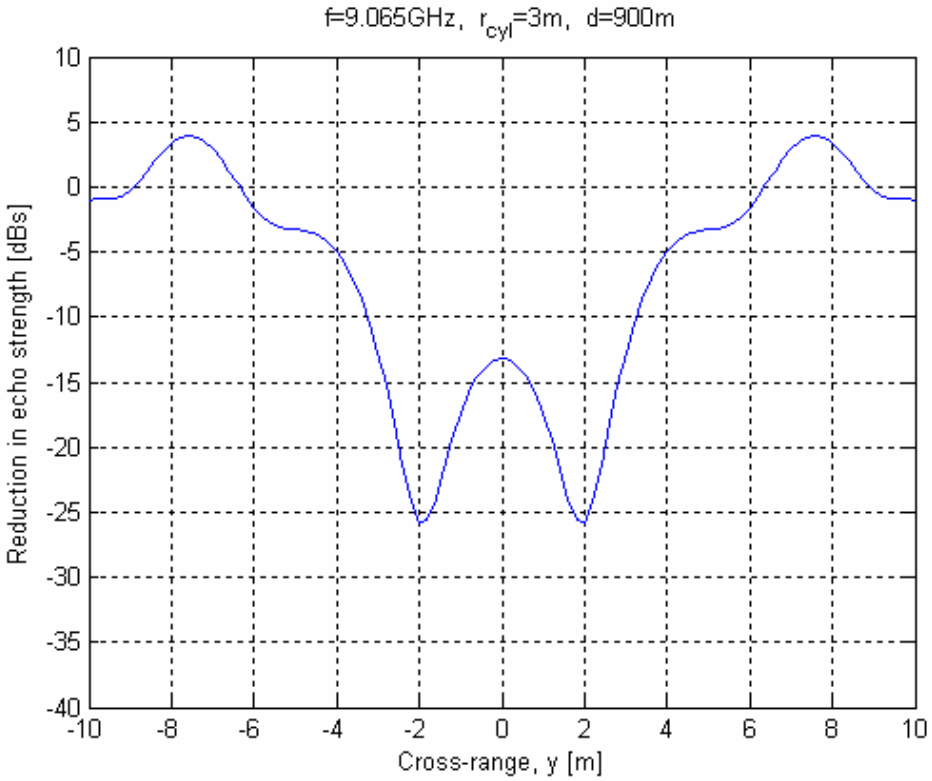

Figure 3.17 *Cross-range cut of the reduction in echo strength 900 m behind an infinitely long conducting cylinder with radius 3 m at 9.065 GHz (compare with Figure 3.16).*

3.4 Paper IV

Paper IV studies the effects of wind turbines on radar systems (5).

Paper IV bases its calculations on numerical simulations for the wind turbine - radar system, and uses the Method of Moments (MoM) and the Multi-Level Fast Multidipole Method (MLFMM). The wind turbine is modelled as consisting of three parts; 1) the tower, which is modelled as a "truncated cone", 2) the nacelle, which is modelled as a rotational ellipsoid with vertical rotation axis, and 3) the rotor blades.

Paper IV presents a figure showing the electric field behind a wind turbine with radius $r_w = 3.5$ m at 3 GHz (Figure 3.18 in this report). The wind turbine is placed at 25.1 km distance from the emitter, on the direct line between the emitter and the receiving radar, and 4900 m in front of the receiving radar. The reduction in the electric field at the receiving radar is also calculated separately (see Table 3.3 in this report). We have performed the same calculations for comparison. Figure 3.19 and Table 3.3 show the results.

Table 3.3 shows the maximum reduction in the electric field at 3 GHz at a distance 4900 m behind the wind turbine. We see that there is a relatively large discrepancy between our results (3.2 dBV/m) and the results in paper IV (6.6 dBV/m). We must apply a cylinder radius of $r_{cyl} = 6.7$ m in our calculations to obtain the same results as paper IV.

Figure 3.18 (paper IV) shows the reduction in the electric field behind a wind turbine with radius 3.5 m at 3 GHz. Figure 3.19 (our calculations) shows the electric field behind an infinitely long conducting cylinder with radius 6.7 m at 3 GHz. We see that there is quite good agreement between the two figures.

We also performed calculations for cylinder radii smaller and larger than $r_{cyl} = 6.7$ m. The results showed that when $r_{cyl} < 6.7$ m the reduction in the electric field is smaller (less shadow) at all distances, which agrees well with the results of paper IV close behind the wind turbine, but gives too little shadow at longer distances. When $r_{cyl} > 6.7$ m the reduction in the electric field is larger at all distances, which gives too dark shadow compared to the results in paper IV, especially close behind the wind turbine. Based on our findings, we conclude that a cylinder radius of $r_{cyl} = 6.7$ m gives the best correspondence with the results of paper IV.

Frequency	Distance	Maximum reduction in electric field	r_w	r_{cyl}
3GHz	4900m	6.6dBV/m (3.2dBV/m)	3.5m	6.7m

Table 3.3 *Maximum reduction in the electric field for given frequency and distance behind the wind turbine. The column marked r_w shows the cylinder radius used by paper IV for the calculations, while the column marked r_{cyl} shows the cylinder radius used in this report to obtain the same values. Numbers in parentheses show the results for the maximum reduction in the electric field when we use $r_{cyl} = r_w$.*

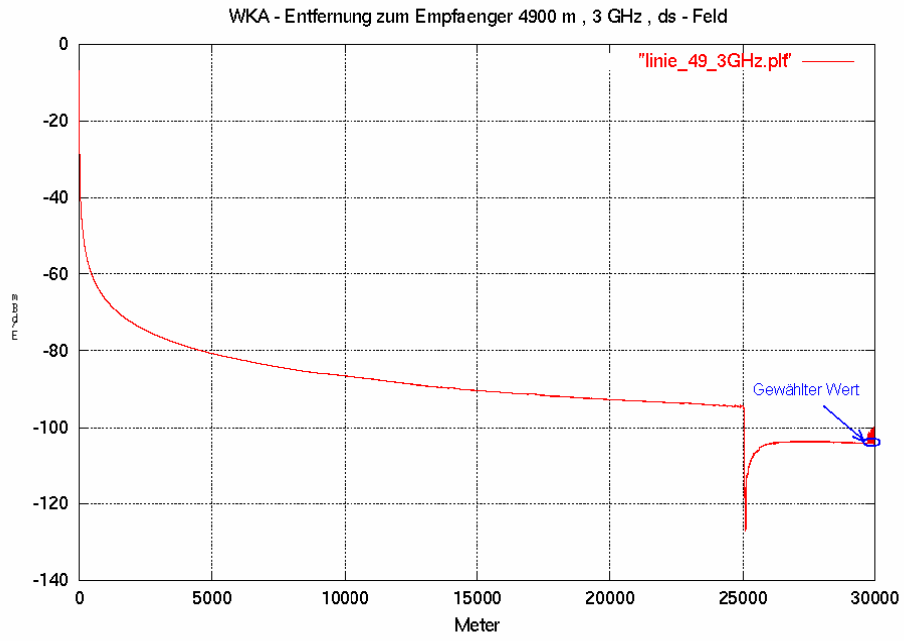

Figure 3.18 *Figure 10 in (5) showing the electric field behind a wind turbine with radius 3.5 m at 3 GHz. The wind turbine is at 25.1 km distance from the emitter and 4900 m in front of the receiving radar (marked by blue arrow in the figure).*

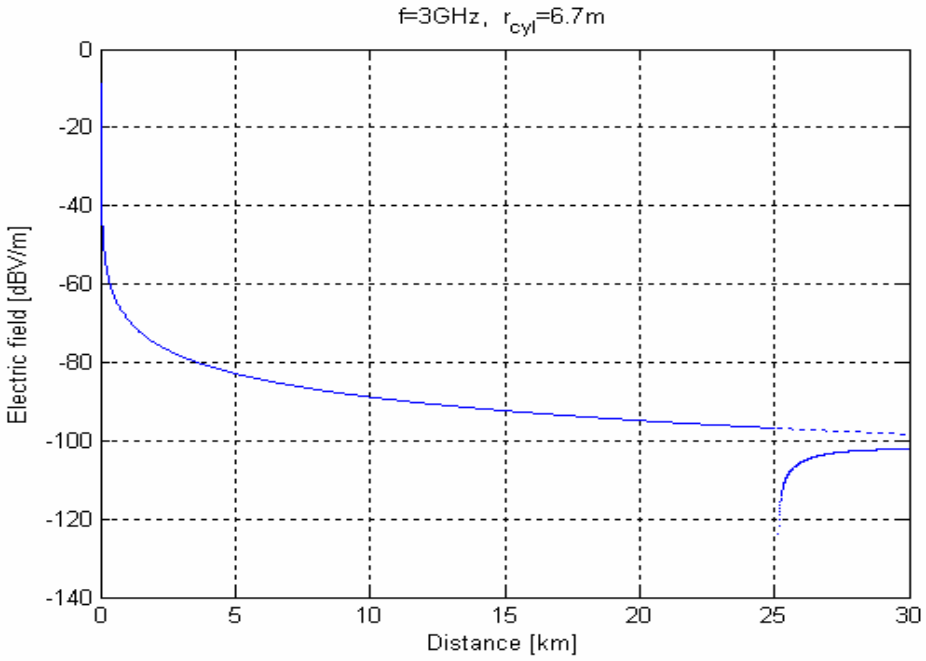

Figure 3.19 *The electric field behind an infinitely long conducting cylinder with radius 6.7 m at 3 GHz (compare with Figure 3.18). The cylinder is at 25.1 km distance from the emitter and 4900 m in front of the receiving radar.*

3.5 Paper V

Paper V presents the results of the electromagnetic investigations and assessments of marine radar, communications and positioning systems undertaken at the North Hoyle wind farm by QinetiQ and the Maritime and Coastguard Agency (MCA) (3).

The North Hoyle wind farm is the first large-scale off-shore wind farm in the United Kingdom. The North Hoyle wind turbines have a tower height (above water) of 70 m and a radius of $r_w = 2.5$ m. Figure 3.20 shows a photo of the wind turbines.

Figure 3.20 North Hoyle Vestas wind turbines (Figure 6-1 in (3)).

Trials were performed for both VHF and radar frequencies. Table 3.4 in this report presents the results from the trials showing the measured maximum reduction in electric field/echo strength for different frequencies and distances behind the wind turbine. The corresponding numbers calculated by us are given in parentheses. The last column in the table shows the cylinder radius r_{cyl} that we would use in our calculations to obtain the same results as measured in the trials.

At 150 MHz and a distance of 5 m behind the wind turbine the maximum reduction in the electric field calculated by us (25.1 dBV/m) is significantly larger than the maximum reduction measured during the trial (10 dBV/m). On the other hand, at the same frequency and a distance of 500 m the maximum reduction in the electric field calculated by us (1.7dBV/m) is somewhat smaller than the measured value (2-3dBV/m). At 9.4 GHz and a distance of 1000 m behind the wind turbine the maximum reduction in echo strength calculated by us (20.5dBs) is larger than the measured value (14.4 dBs).

The results from our calculations deviate from the measured values, being sometimes larger and sometimes smaller. In order to obtain the same values as measured in the trial, we have to use cylinder radii in the range $r_{cyl} = 1.0 - 4.0$ m in our calculations.

Frequency	Distance	Maximum reduction in electric field/echo strength	r_w	r_{cyl}
150MHz	5m	10dBV/m (25.1dBV/m)	2.5m	1.0m
150MHz	500m	2-3dBV/m (1.7dBV/m)	2.5m	4.0m
9.46GHz	1000m	14.4dBs (20.5dBs)	2.5m	1.8m

Table 3.4 Measured maximum reduction in electric field/echo strength for given frequency and distance behind the wind turbine. The column marked r_w shows the radius of the North Hoyle wind turbines, while the column marked r_{cyl} shows the cylinder radius used in this report to obtain the same results as were found in the trials. Numbers in parentheses show the results for the maximum reduction in the electric field/echo strength when we use $r_{cyl}= r_w$.

3.6 The cylinder radius

The infinitely long conducting cylinder model is a simplified representation of the wind turbine. The model has one parameter that can be adjusted; the cylinder radius r_{cyl}. The cylinder radius describes the size of the wind turbine, and it may or may not be equal to the actual wind turbine radius r_w. Based on the literature study in Section 3.1-3.5 we will try to determine the value for the cylinder radius r_{cyl} that best represents the actual wind turbine.

Table 3.5 shows the results from the literature study we did in Section 3.1-3.5. Paper I and II base their calculations on the (infinitely long) conducting cylinder model, and we found good agreement between their results and our results, as we would expect.

Paper III and IV use more sophisticated models for the wind turbine and is therefore expected to represent reality more closely. Comparison of our results with the results of paper III indicates that we should use a cylinder radius equal to the wind turbine radius, i.e., $r_{cyl} = r_w$. On the other hand, comparing our results with the results of paper IV showed that we should choose a cylinder radius somewhat larger (6.7 m) than the wind turbine radius (3.5 m), i.e., $r_{cyl} = 1.9 r_w$.

Paper V presents actual measurement results, and the wind turbines used in the trials have a radius of 2.5 m. Comparison of their measured values with the results from our calculations indicates that we should use a cylinder radius in the range $r_{cyl} = (0.4 - 1.6) r_w$.

Table 3.6 presents a summary of the findings above. Based on the table we conclude that the cylinder radius should be approximately equal to the actual wind turbine radius. Note, however, that this is the average wind turbine radius. The tower is usually wider at the base ($r_w^{\max} > r_w$) and narrower at the top ($r_w^{\min} < r_w$). In order to cover the worst-case scenario, we recommend to use

$$r_{cyl} = r_w^{\max} \tag{3.3}$$

where $r_w^{\max}$ is the maximum wind turbine tower radius.

Paper	Method	Frequency	Distance	Reduction in electric field/echo strength	r_w	r_{cyl}
I	Infinite conducting cylinder	100MHz	100m	<3dBV/m (2.2dBV/m)	1.5m	**<2.1m**
		1GHz	100m	8.5dBV/m (6.2dBV/m)	1.5m	**2.0m**
II	Conducting cylinder	9.4GHz	1000m	10-20dBs (11-21dBs)	2.6m	**2.6m**
		9.4GHz	2000m	~10dBs (8-14dBs)	2.6m	**2.6m**
III	Geometric-optical diffraction	9.065GHz	-	See Figure 3.14-Figure 3.17	3m	**3m**
IV	MoM, MLFMM	3GHz	4900m	6.6dBV/m (3.2dBV/m)	3.5m	**6.7m**
		3GHz	≤4900m	See Figure 3.18-Figure 3.19	3.5m	**6.7m**
V	Trial	150MHz	5m	10dBV/m (25.1dBV/m)	2.5m	**1.0m**
		150MHz	500m	2-3dBV/m (1.7dBV/m)	2.5m	**4.0m**
		9.46GHz	1000m	14.4dBs (20.5dBs)	2.5m	**1.8m**

Table 3.5 Summary of the results from the literature study in Section 3.1-3.5. The table shows the calculated/measured reduction in the electric field/echo strength for different frequencies and distances behind the wind turbine. The column marked r_w shows the wind turbine radius, while the column marked r_{cyl} shows the cylinder radius used in this report to obtain the same values. Numbers in parentheses show the results for the reduction in electric field/echo strength when we use $r_{cyl} = r_w$.

Paper	r_{cyl}
III	1 r_w
IV	1.9 r_w
V	(0.4-1.6) r_w

Table 3.6 *Best choice for the cylinder radius.*

4 RESULTS

We will in this chapter present the results from the calculations on electromagnetic shadow effects behind wind turbines.

The wind turbine has been modelled as an infinitely long conducting cylinder. We have used a cylinder radius of 3 m for the calculations. This corresponds to a large wind turbine with maximum tower radius 3 m.

We have calculated the shadow effects for five different frequencies; 100 MHz, 1 GHz, 3 GHz, 9 GHz, and 15 GHz.

4.1 The electric field around an infinitely long conducting cylinder

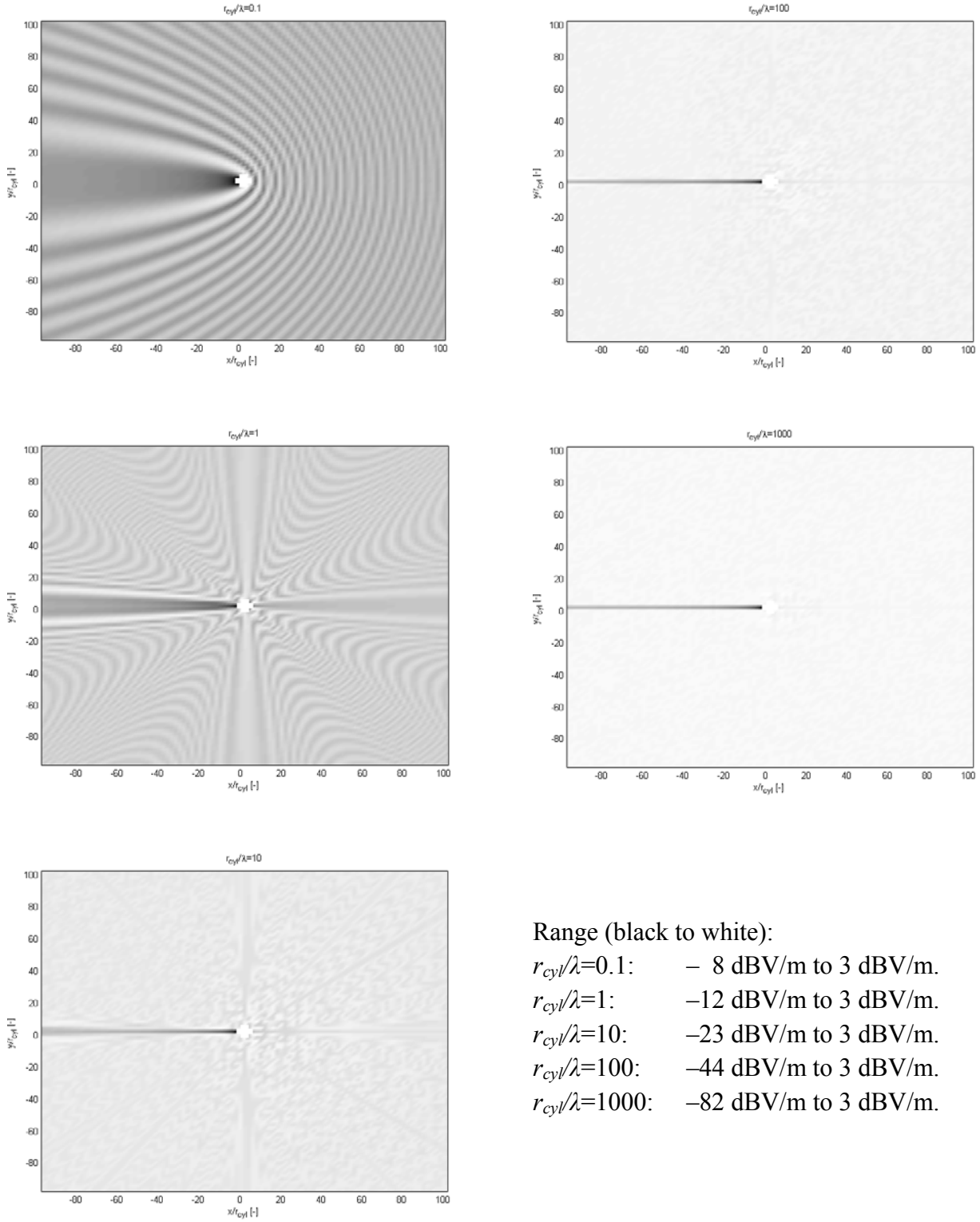

Range (black to white):

r_{cyl}/λ=0.1: – 8 dBV/m to 3 dBV/m.
r_{cyl}/λ=1: –12 dBV/m to 3 dBV/m.
r_{cyl}/λ=10: –23 dBV/m to 3 dBV/m.
r_{cyl}/λ=100: –44 dBV/m to 3 dBV/m.
r_{cyl}/λ=1000: –82 dBV/m to 3 dBV/m.

Figure 4.1 The electric field (dBV/m) around an infinitely long conducting cylinder for different r_{cyl}/λ.

4.2 The shadow boundary equation

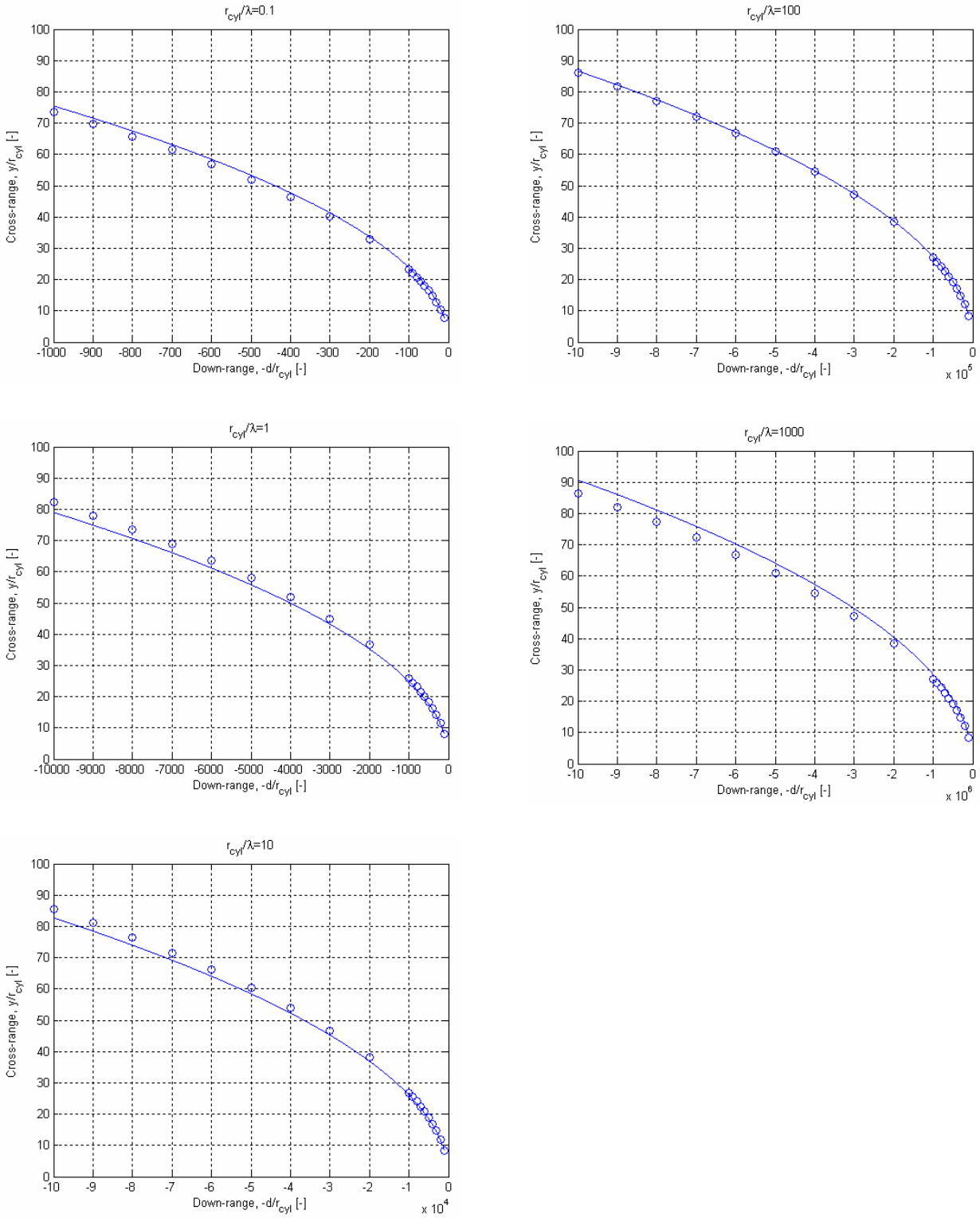

Figure 4.2 The boundary of the shadow region behind an infinitely long conducting cylinder for different r_{cyl}/λ (blue circles). The solid blue line shows the results when using Equation (2.7) to calculate the shadow boundary.

4.3 The shadow depth equation

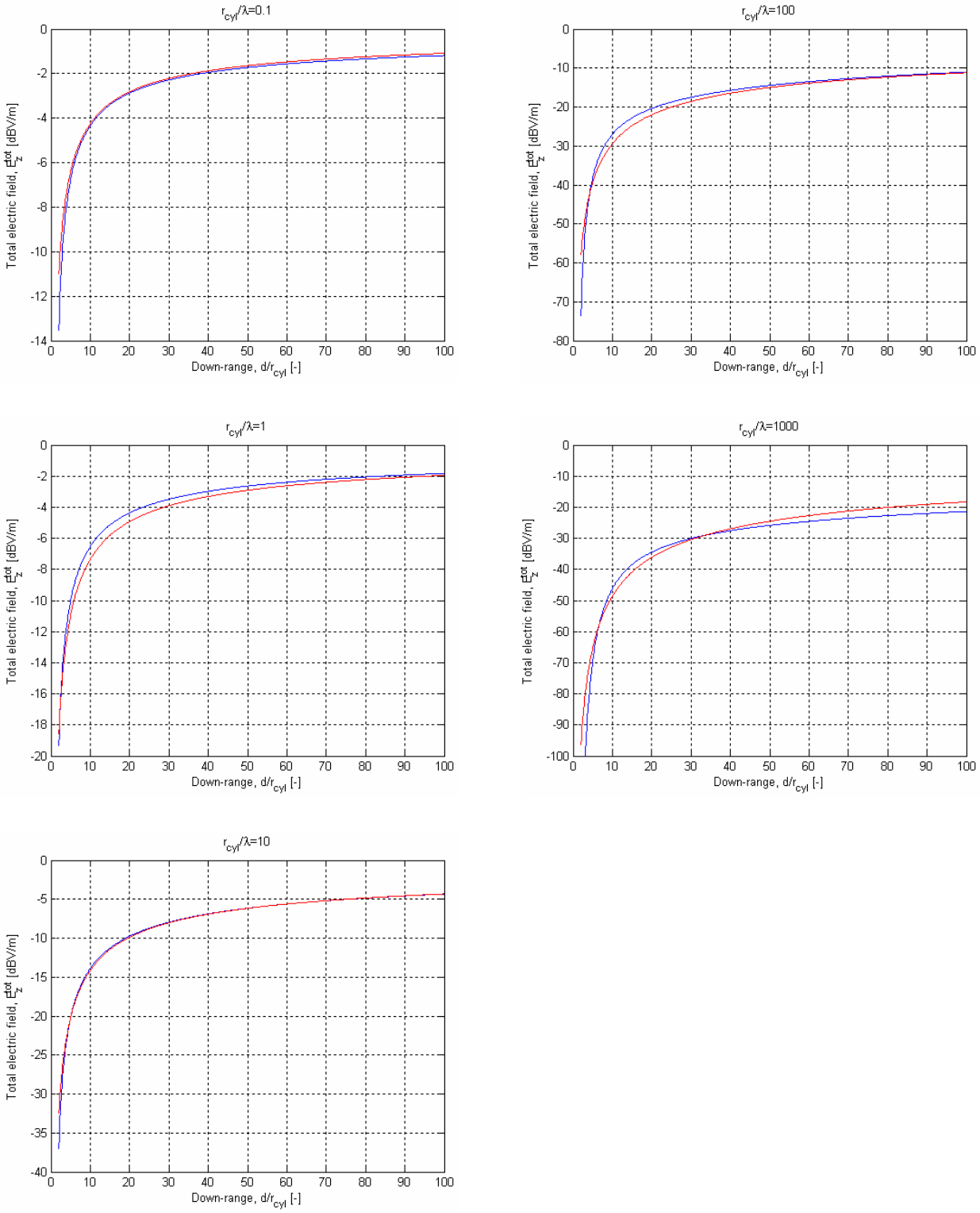

Figure 4.3 The reduction in the electric field (shadow depth) behind an infinitely long conducting cylinder for different r_{cyl}/λ (blue line). The red line shows the results when using Equation (2.12) to calculate the shadow depth.

4.4 The angular dependency of the electric field

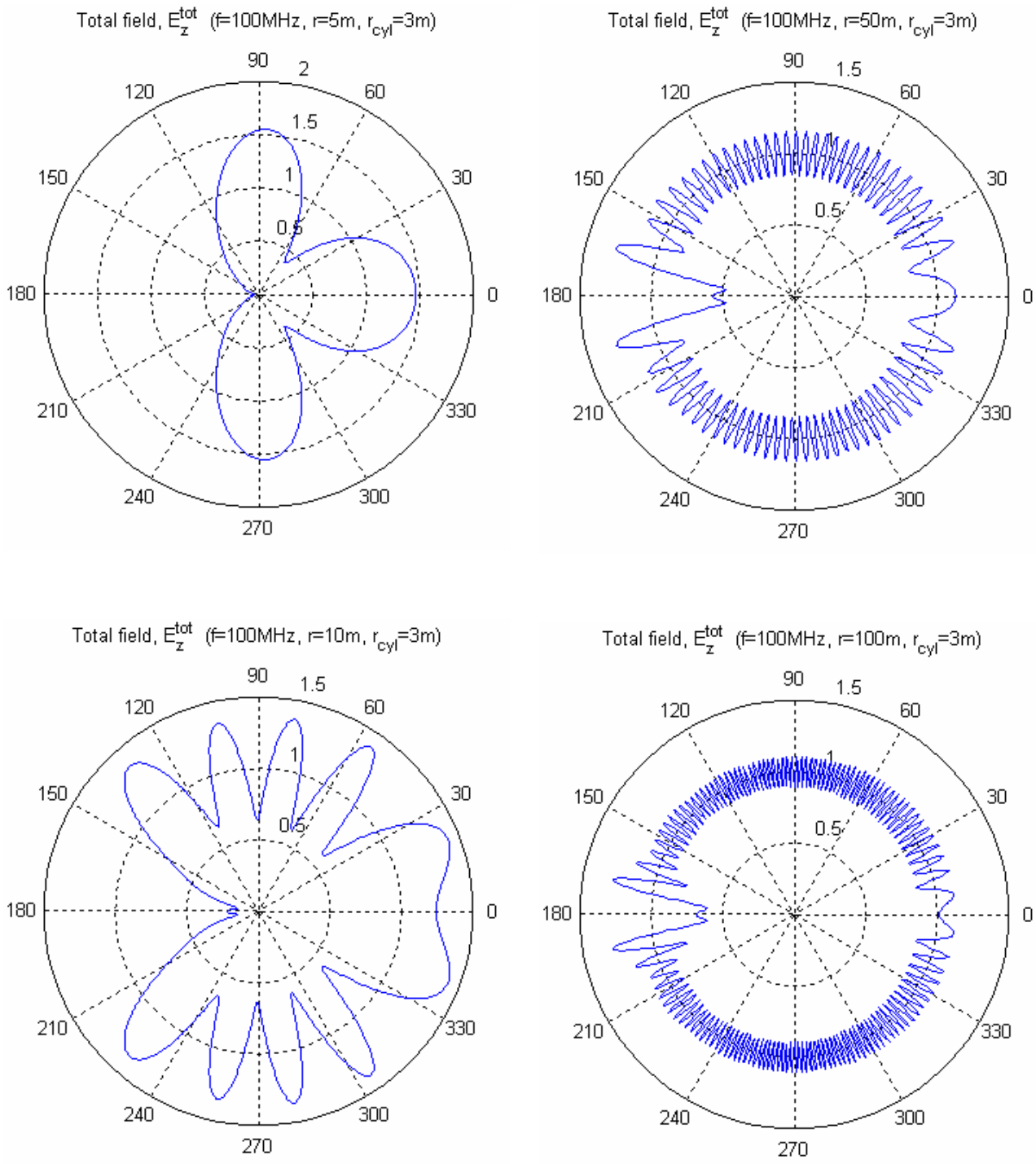

Figure 4.4 Angular plots of the electric field (V/m) at different distances around an infinitely long conducting cylinder with radius 3 m at 100 MHz.

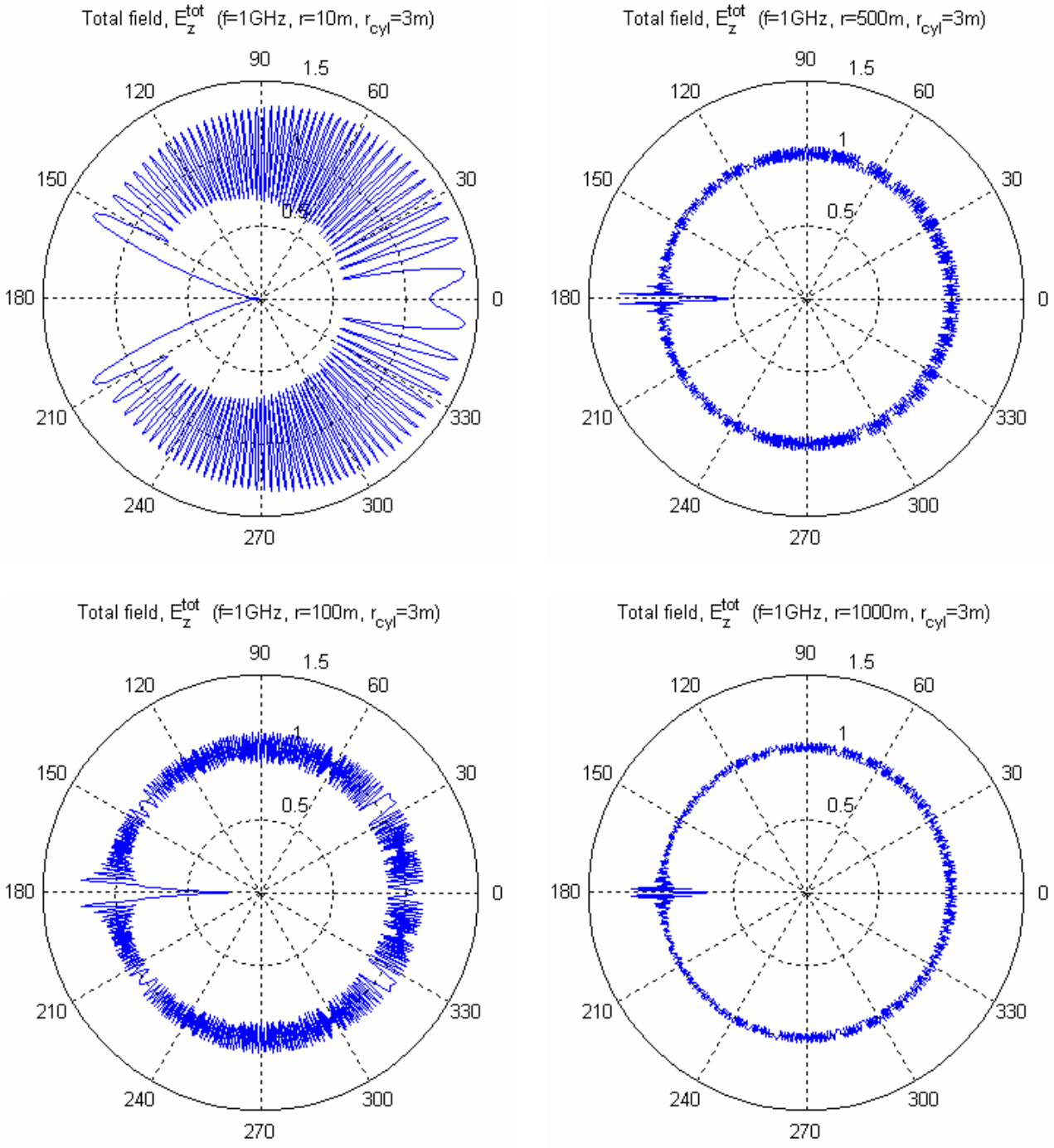

Figure 4.5 *Angular plots of the electric field (V/m) at different distances around an infinitely long conducting cylinder with radius 3 m at 1 GHz.*

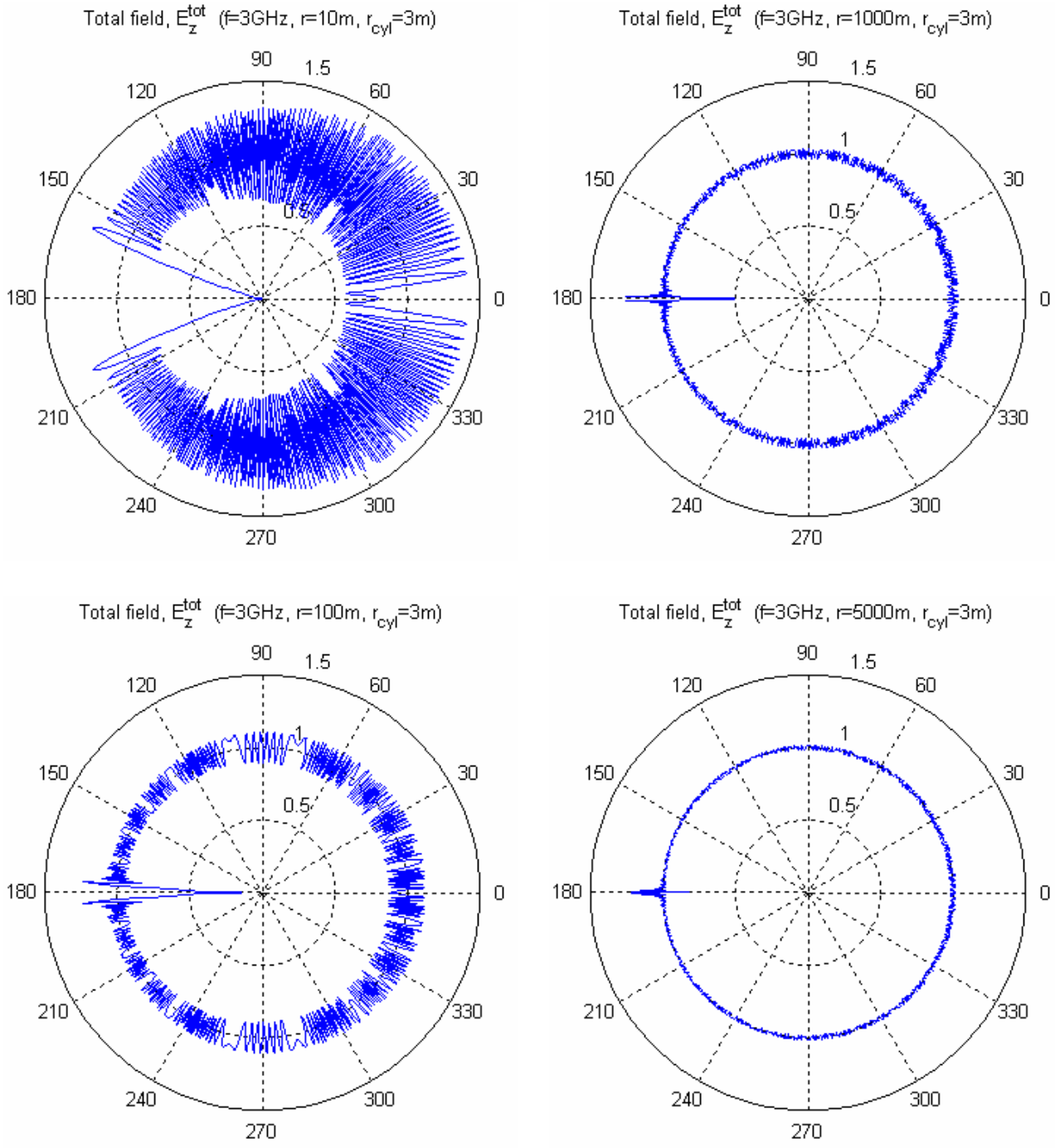

Figure 4.6 *Angular plots of the electric field (V/m) at different distances around an infinitely long conducting cylinder with radius 3 m at 3 GHz.*

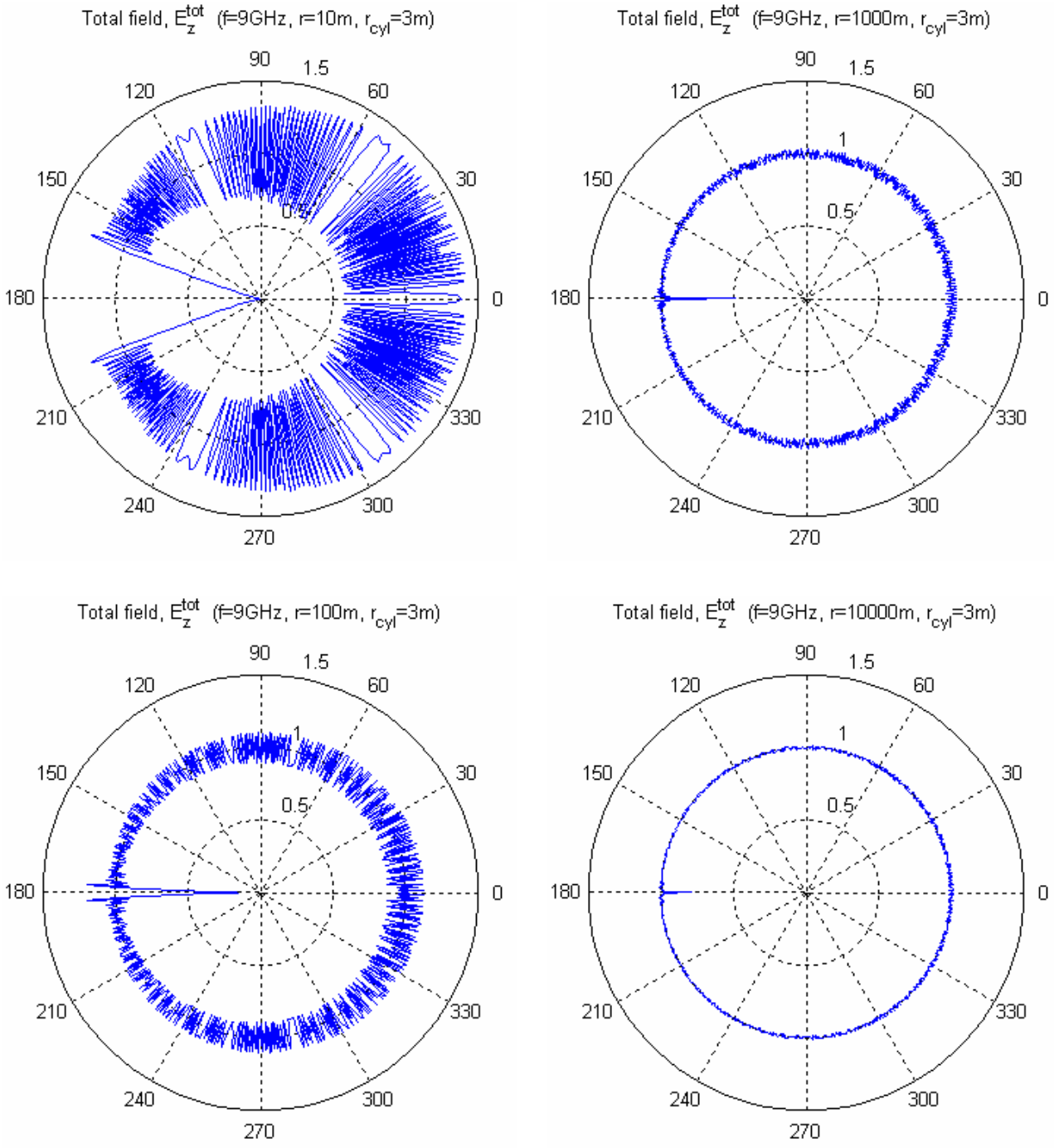

Figure 4.7 *Angular plots of the electric field (V/m) at different distances around an infinitely long conducting cylinder with radius 3 m at 9 GHz.*

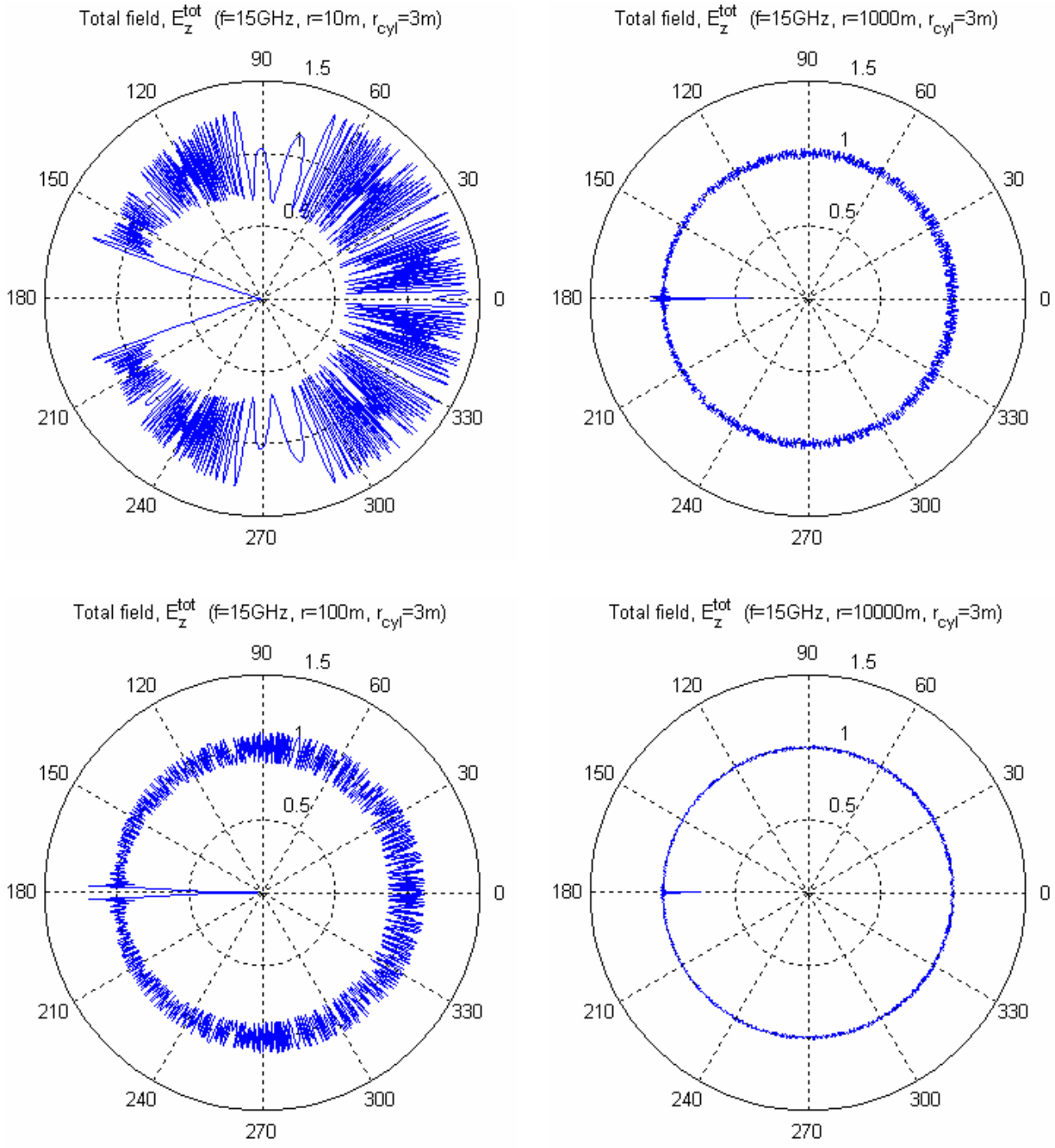

Figure 4.8 *Angular plots of the electric field (V/m) at different distances around an infinitely long conducting cylinder with radius 3 m at 15 GHz.*

4.5 Cross-range cuts of the electric field

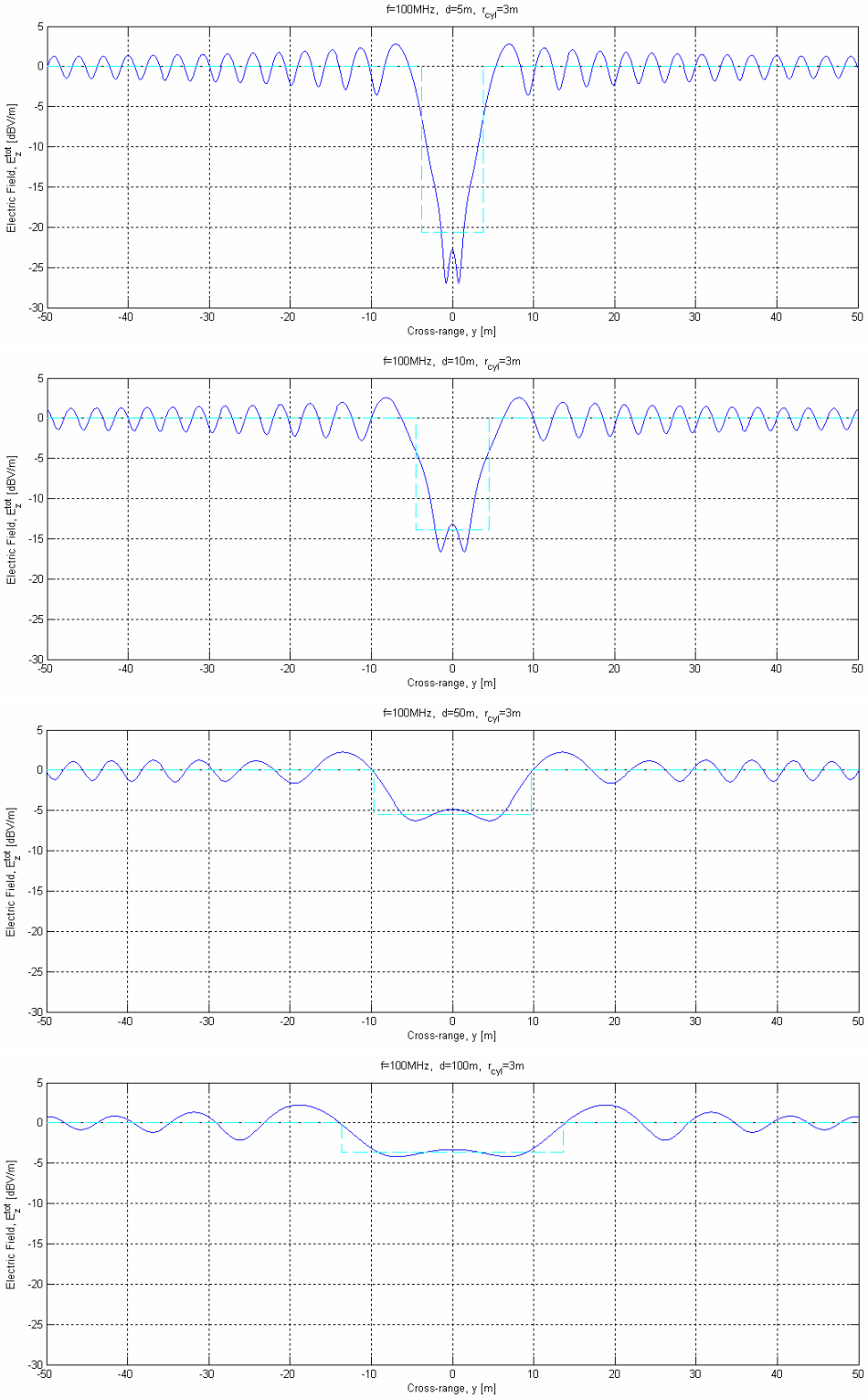

Figure 4.9 *Cross-range cuts of the electric field at different distances behind an infinitely long conducting cylinder with radius 3 m at 100 MHz (dark blue line). Light blue dashed line shows the electric field when using Equations (2.7) and (2.12) to calculate the shadow boundary and depth.*

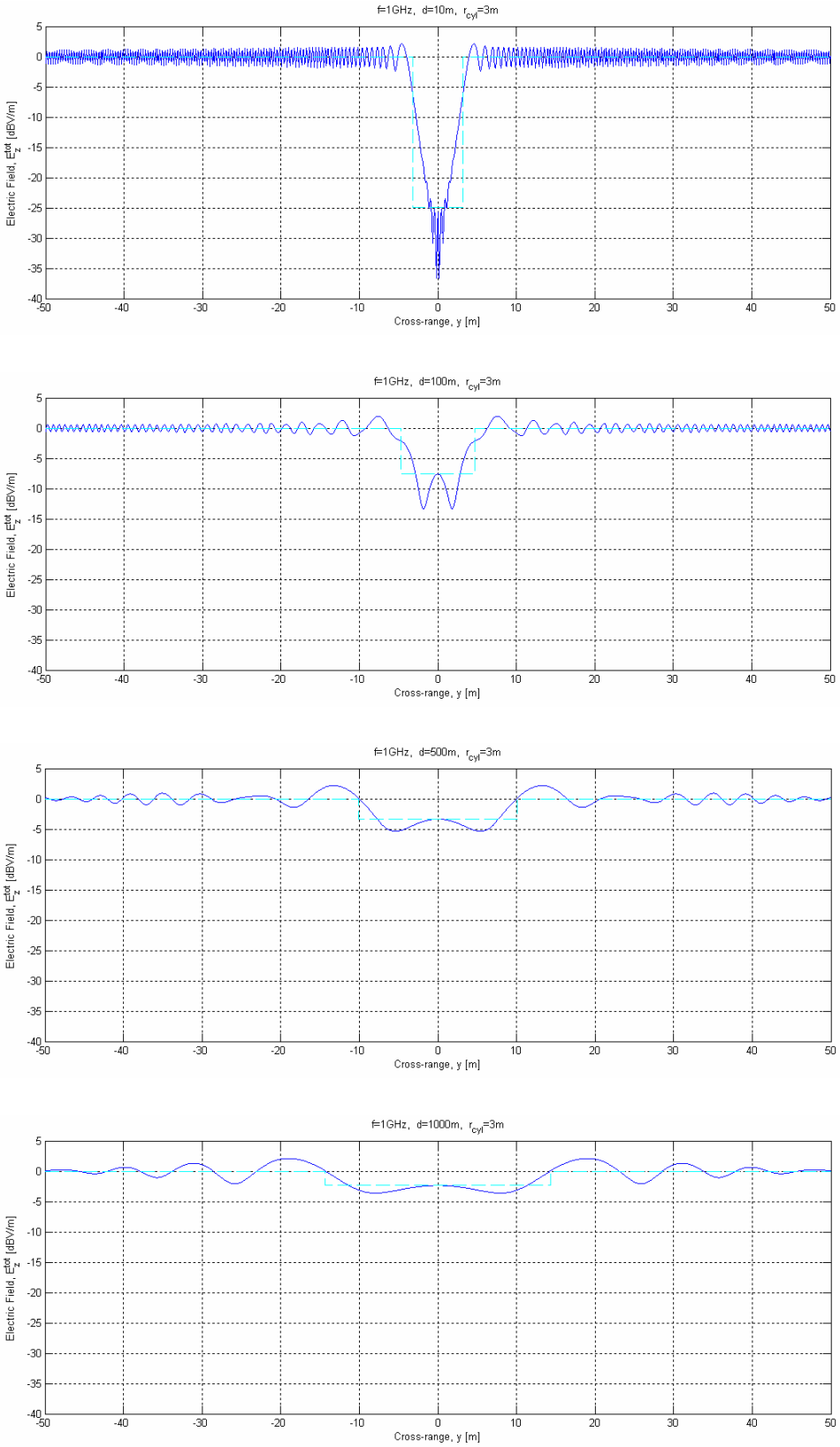

Figure 4.10 Cross-range cuts of the electric field at different distances behind an infinitely long conducting cylinder with radius 3 m at 1 GHz (dark blue line). Light blue dashed line shows the electric field when using Equations (2.7) and (2.12) to calculate the shadow boundary and depth.

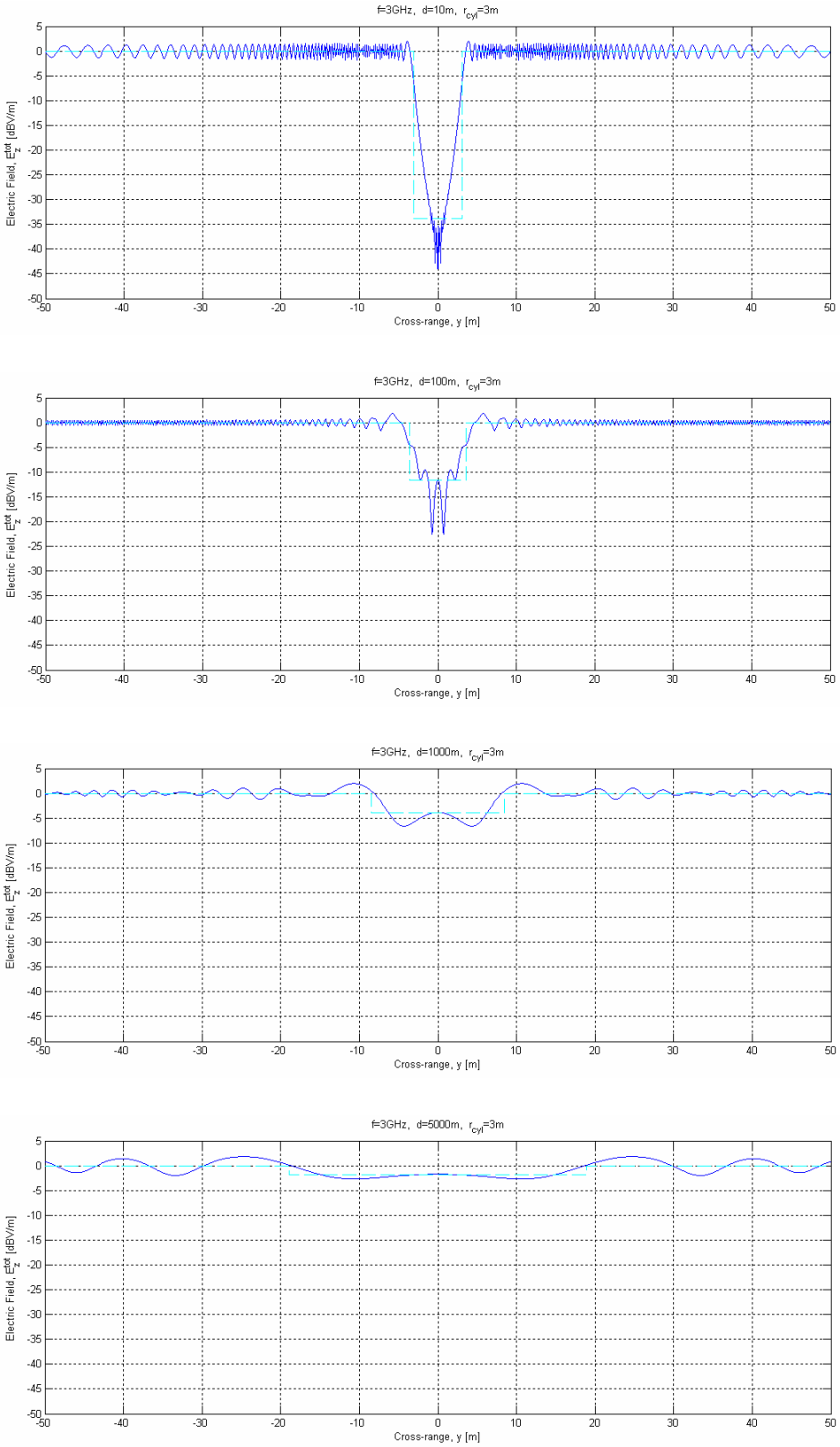

Figure 4.11 Cross-range cuts of the electric field at different distances behind an infinitely long conducting cylinder with radius 3 m at 3 GHz (dark blue line). Light blue dashed line shows the electric field when using Equations (2.7) and (2.12) to calculate the shadow boundary and depth.

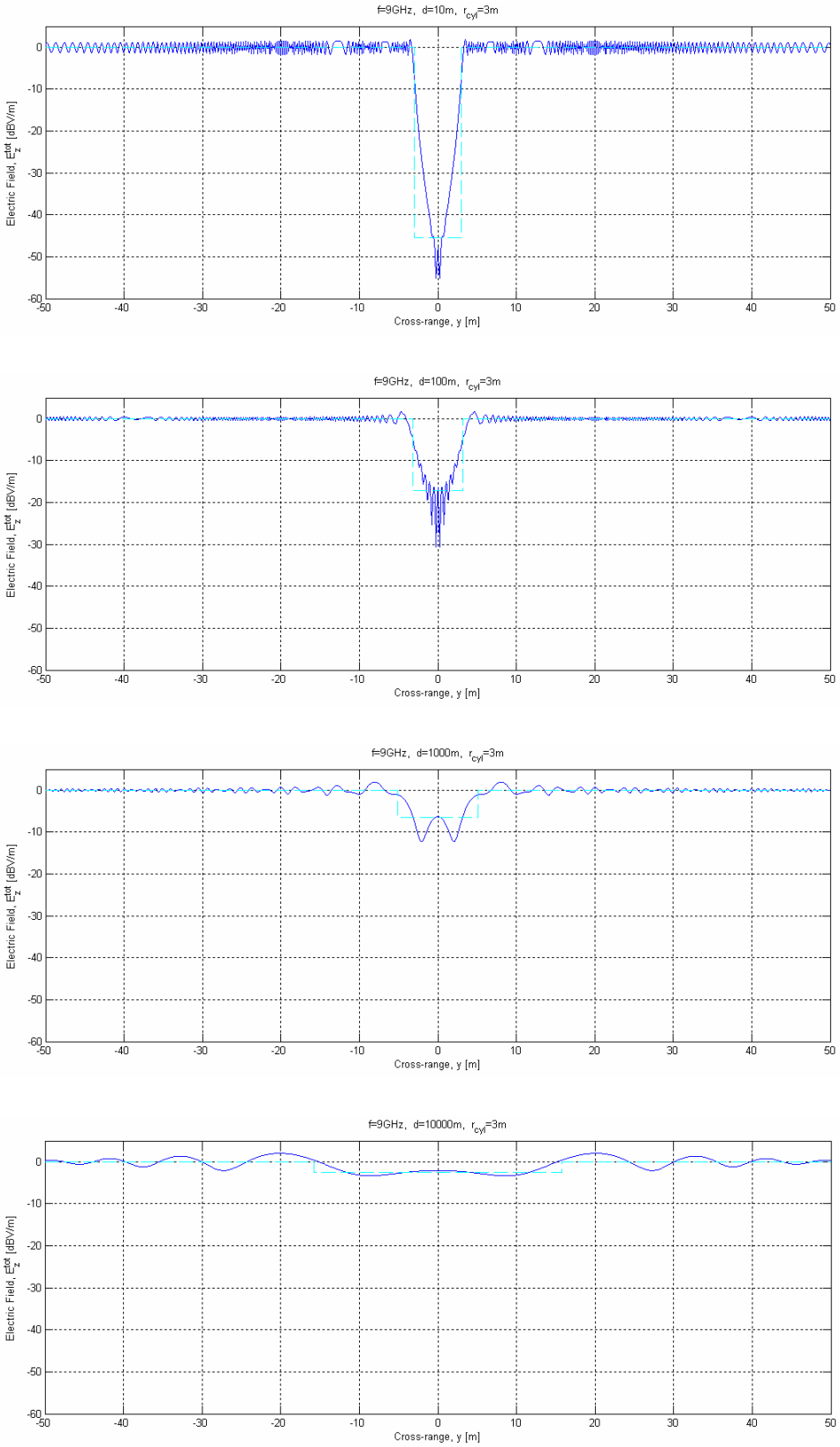

Figure 4.12 Cross-range cuts of the electric field at different distances behind an infinitely long conducting cylinder with radius 3 m at 9 GHz (dark blue line). Light blue dashed line shows the electric field when using Equations (2.7) and (2.12) to calculate the shadow boundary and depth.

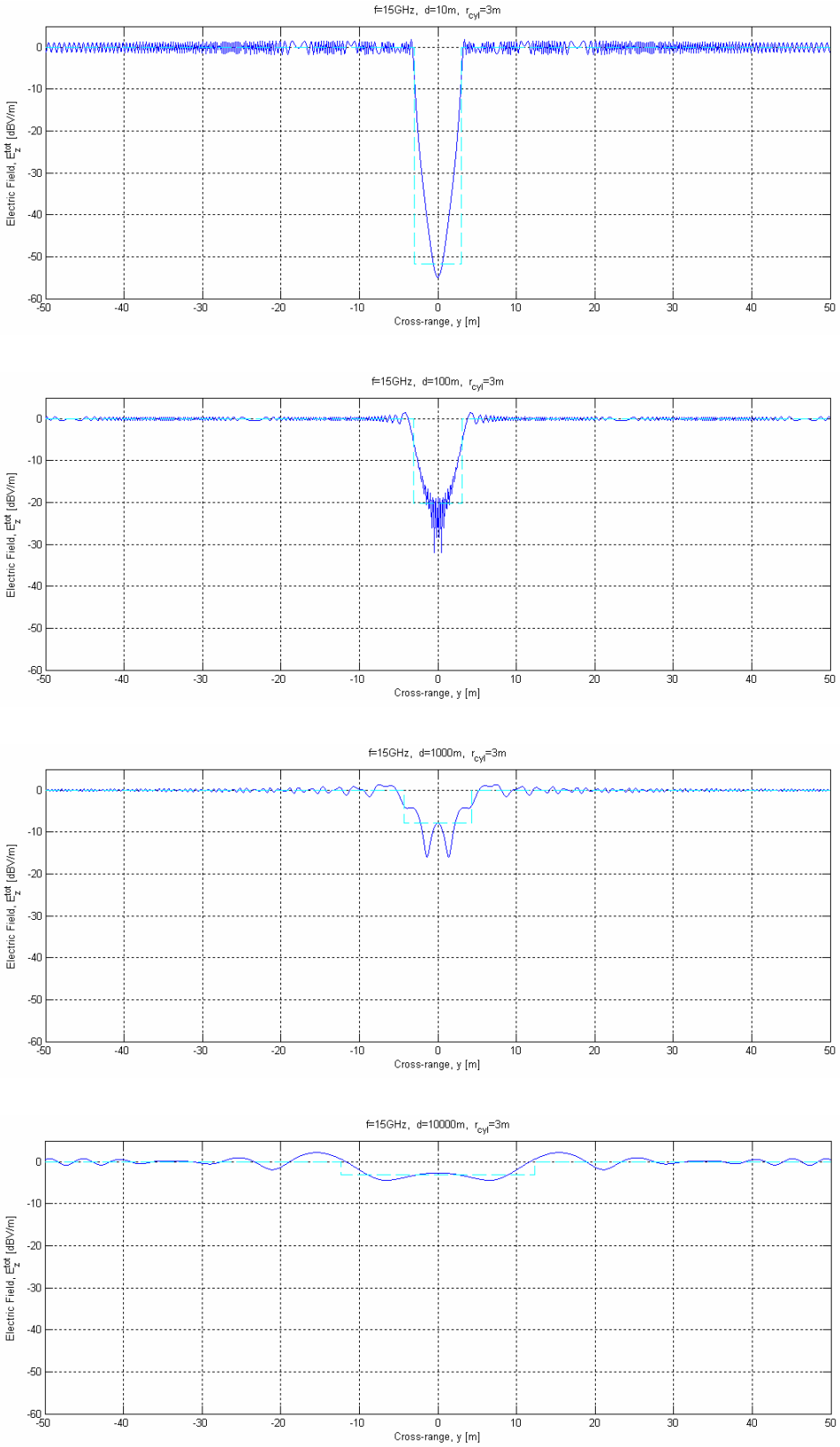

Figure 4.13 Cross-range cuts of the electric field at different distances behind an infinitely long conducting cylinder with radius 3 m at 15 GHz (dark blue line). Light blue dashed line shows the electric field when using Equations (2.7) and (2.12) to calculate the shadow boundary and depth.

4.6 The radial dependency of the electric field

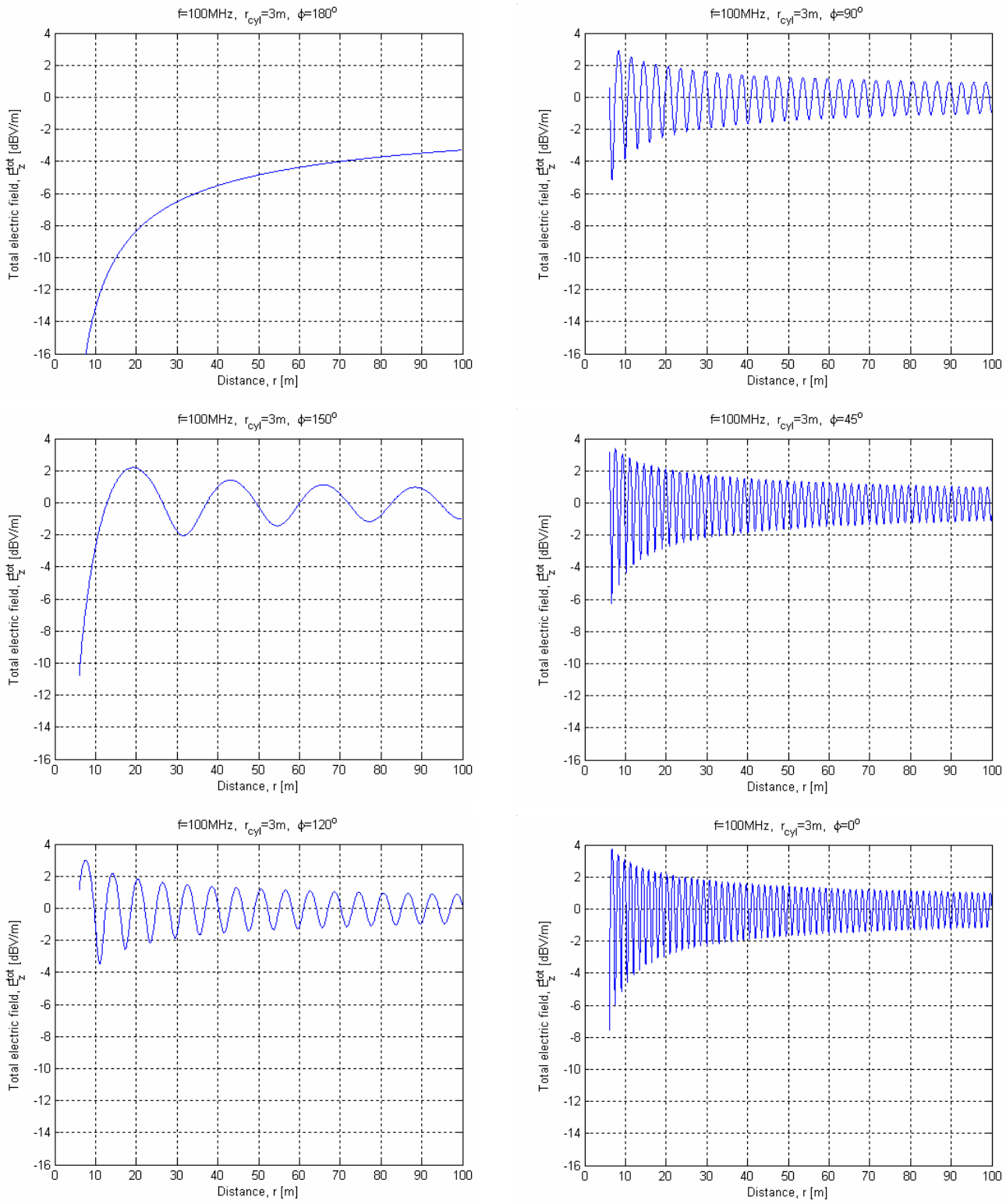

Figure 4.14 The electric field as a function of distance for different angles around an infinitely long conducting cylinder with radius 3 m at 100 MHz.

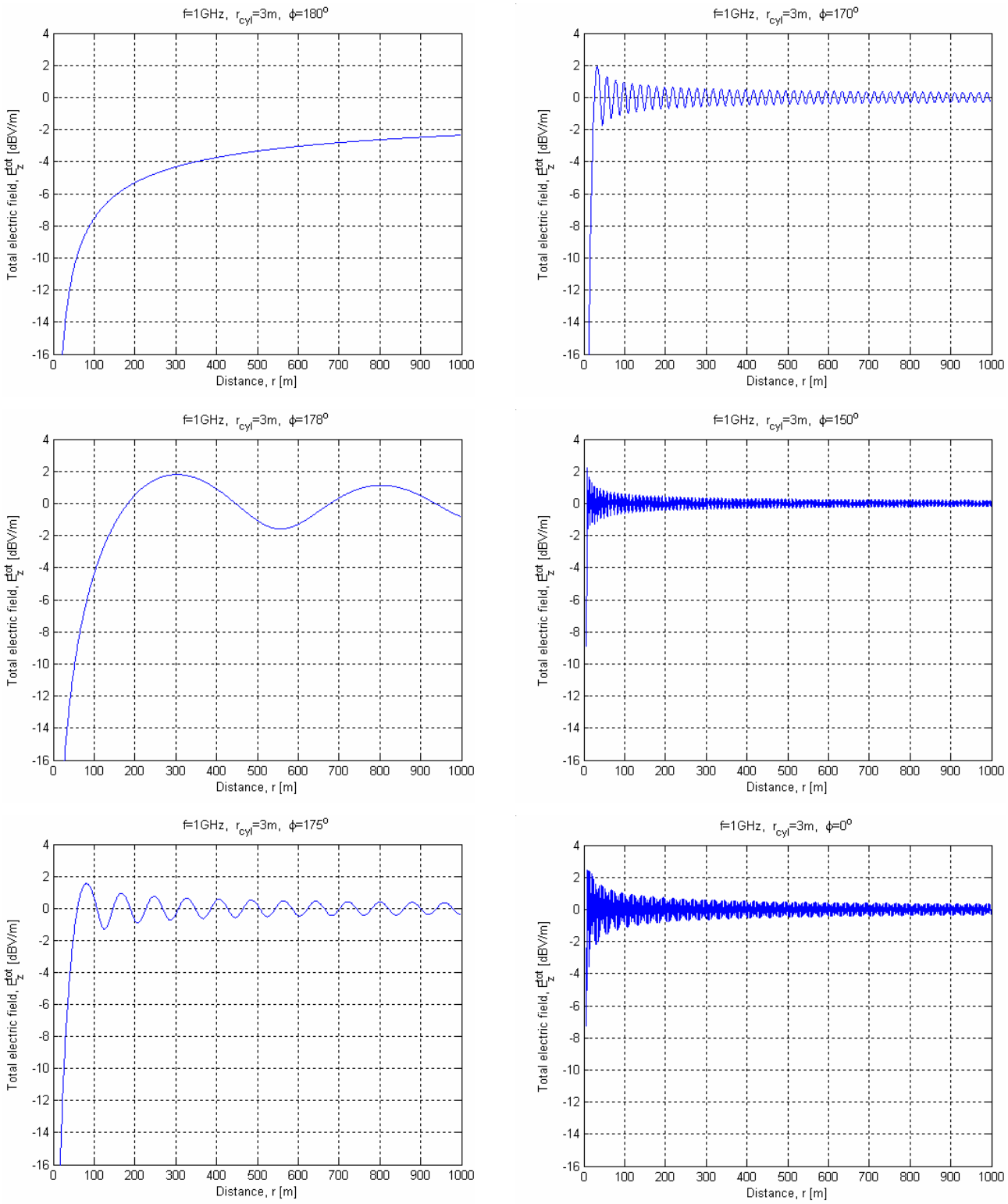

Figure 4.15 The electric field as a function of distance for different angles around an infinitely long conducting cylinder with radius 3 m at 1 GHz.

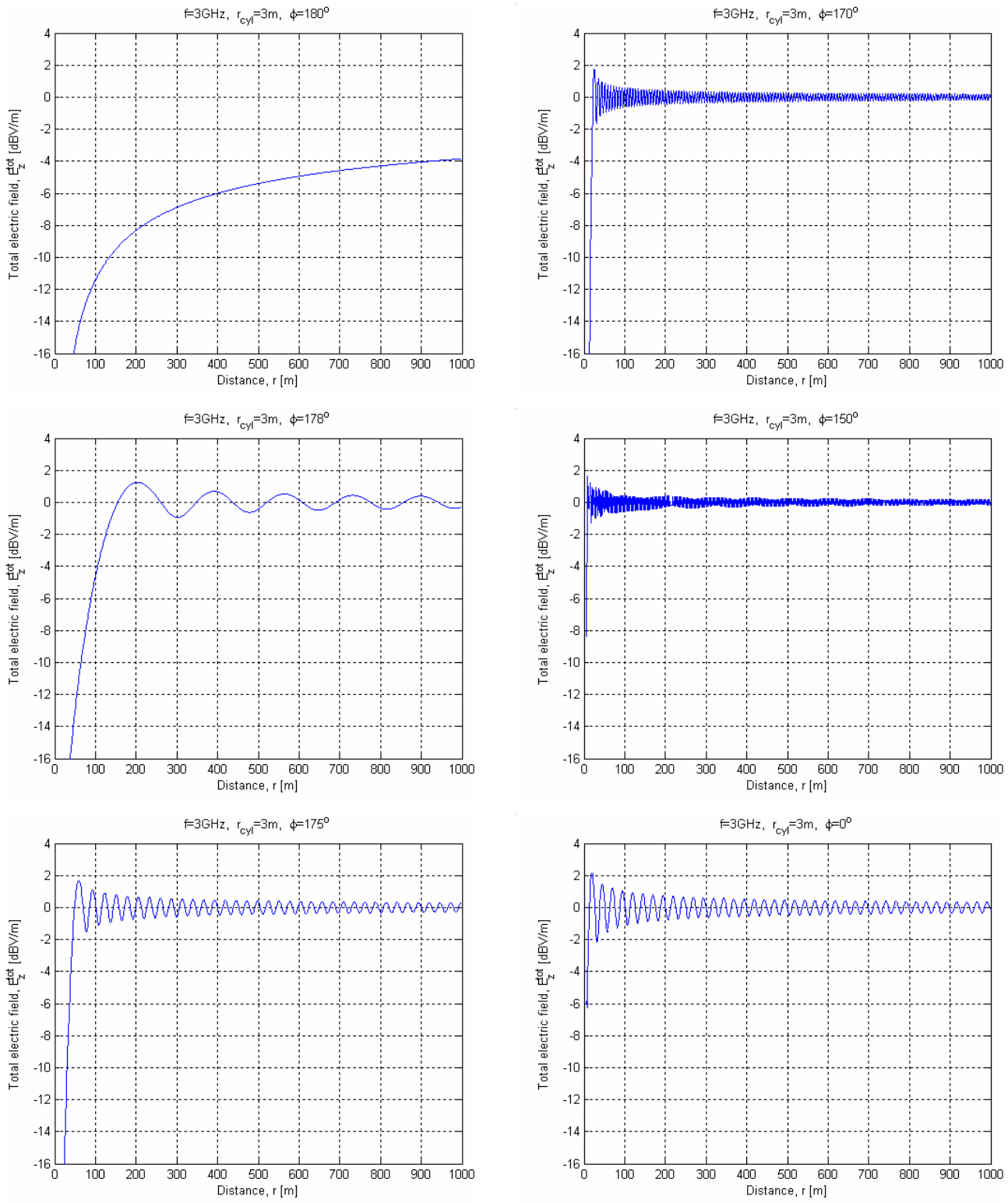

Figure 4.16 The electric field as a function of distance for different angles around an infinitely long conducting cylinder with radius 3 m at 3 GHz.

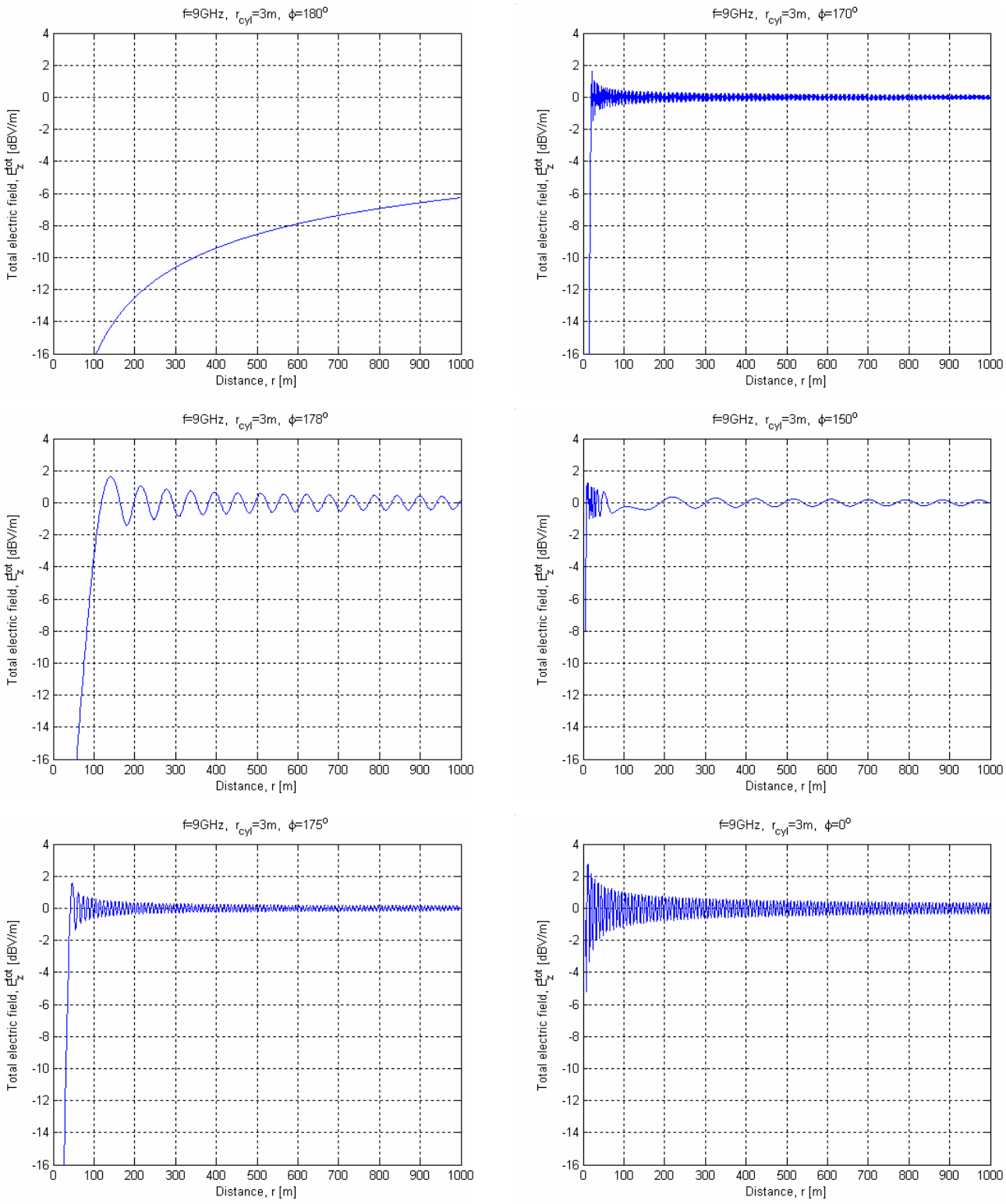

Figure 4.17 The electric field as a function of distance for different angles around an infinitely long conducting cylinder with radius 3 m at 9 GHz.

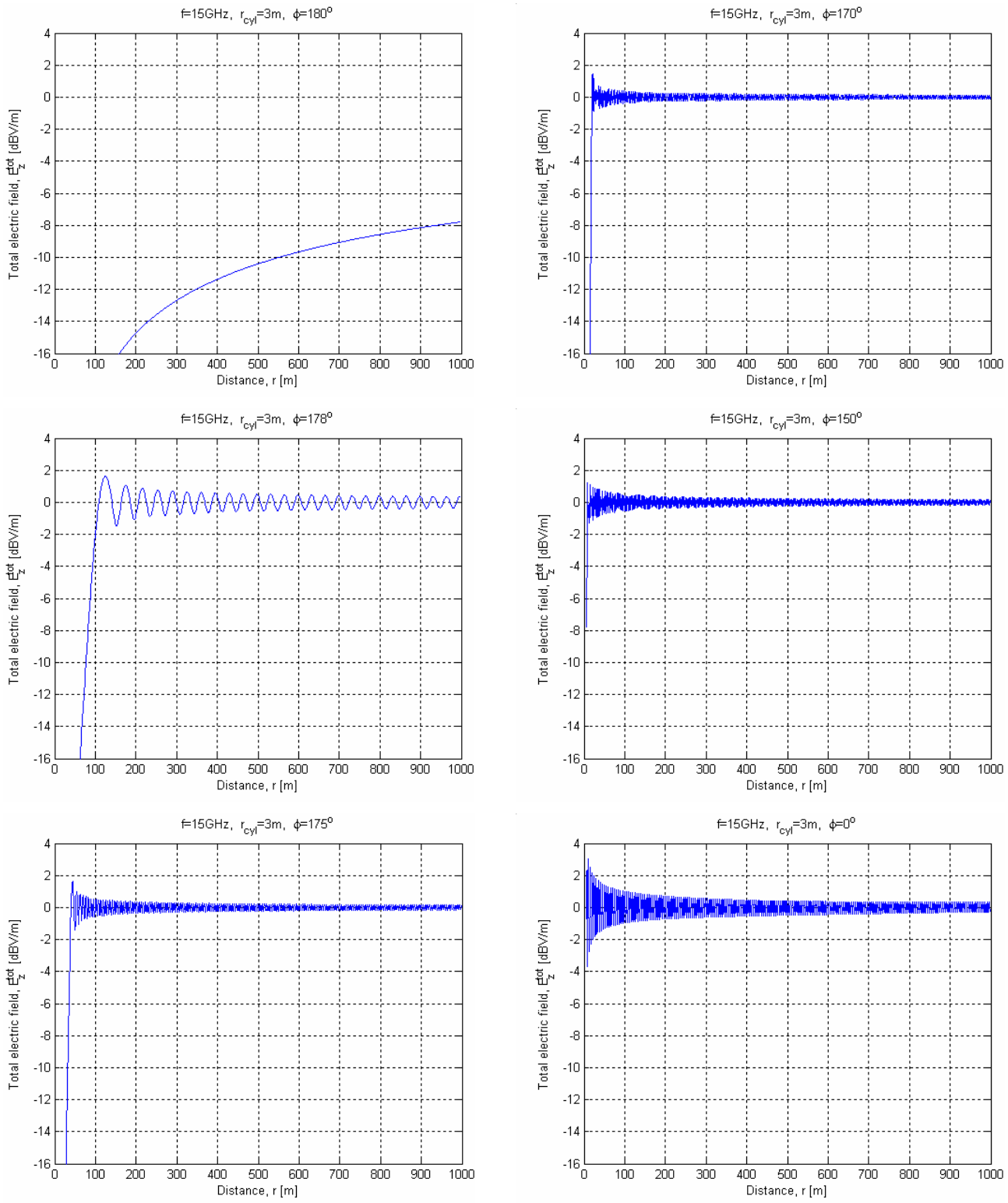

Figure 4.18 The electric field as a function of distance for different angles around an infinitely long conducting cylinder with radius 3 m at 15 GHz.

4.7 The shadow boundary and depth

f	d (m)	$\|Y_b\|$ (m)	$\|y_{min}\|$ (m)	E_z^{tot} (0) (dBV/m)	$E_z^{tot}(y_{min})$ (dBV/m)	$\|\Delta E_z^{tot}\|$	
						(dBV/m)	(%)
100MHz	5	5.3	0.8	-22.7	-27.0	4.3	18.9
	10	6.2	1.5	-13.1	-16.6	3.5	24.0
	50	9.9	4.6	-4.9	-6.3	1.4	29.3
	100	13.8	6.8	-3.3	-4.2	0.9	27.7
1GHz	10	3.9	0.2	-25.8	-36.7	10.9	42.4
	100	6.2	1.9	-7.6	-13.4	5.8	76.8
	500	10.0	5.4	-3.4	-5.4	2.0	60.0
	1000	14.2	7.9	-2.4	-3.6	1.2	53.4
3GHz	10	3.5	0.1	-35.3	-43.9	8.6	24.5
	100	4.6	0.8	-11.4	-22.6	11.2	98.1
	1000	8.1	4.3	-3.9	-6.6	2.8	71.9
	5000	18.6	10.6	-1.7	-2.7	0.9	54.3
9GHz	10	3.3	0.03	-47.7	-55.2	7.5	15.7
	100	4.0	0.3	-16.3	-30.6	14.3	87.1
	1000	6.7	2.1	-6.3	-12.2	5.9	94.9
	10000	15.1	8.7	-2.1	-3.3	1.2	60.7
15GHz	10	3.2	0	-55.0	-55.0	0	0
	100	3.7	0.5	-18.8	-32.0	13.2	70.1
	1000	5.2	1.4	-7.8	-16.1	8.3	106
	10000	11.6	6.5	-2.6	-4.4	1.8	67.7

Table 4.1 Properties of the shadow region behind an infinitely long conducting cylinder for different frequencies. Here d is the distance behind the cylinder, Y_b is the shadow boundary, i.e., the cross-range distance where the total electric field is equal to the unperturbed electric field, y_{min} is the cross-range distance where the electric field has its minimum value $E_z^{tot}(y_{min})$, E_z^{tot} (0) is the electric field on-axis, and ΔE_z^{tot} is the difference between E_z^{tot} (0) and $E_z^{tot}(y_{min})$.

5 DISCUSSION

We will in this chapter discuss the properties of the electromagnetic shadow behind a wind turbine. The discussion is based on the results presented in Chapter 4, where the wind turbine has been modeled as an infinitely long conducting cylinder.

5.1 The electric field around an infinitely long conducting cylinder

Figure 4.1 shows the electric field around an infinitely long conducting cylinder for different ratios between the cylinder radius r_{cyl} and the wavelength λ. The cylinder is placed in the center of the figure with the incoming plane wave moving from the right to the left.

When $r_{cyl} / \lambda = 0.1$ (upper left figure), i.e., for low frequencies, a clear interference pattern can be seen, where the electric field seems to "bend around" the cylinder. The shadow region behind the cylinder is quite wide, about 50 cylinder radii wide at a distance of 100 cylinder radii behind, but not very deep. The reduction in the electric field is only about 8 dBV/m right behind the cylinder and decreases rapidly outwards.

For increasing r_{cyl} / λ, i.e., for higher frequencies, the shadow region behind the cylinder becomes deeper and narrower. When $r_{cyl} / \lambda = 1000$ the shadow region is only a couple of cylinder radii wide at a distance of 100 cylinder radii behind the cylinder. However, the reduction in the electric field reaches about 80 dBV/m right behind the cylinder.

Summary: For low r_{cyl} / λ (low frequencies) the shadow behind the cylinder is shallow and quite wide, while for increasing r_{cyl} / λ (higher frequency) the shadow becomes deeper and narrower.

5.2 The shadow boundary equation

Figure 4.2 shows the boundary of the shadow region behind an infinitely long conducting cylinder for different ratios between the cylinder radius r_{cyl} and the wavelength λ. The cylinder is placed in origo (lower right corner) of the figure.

Blue circles show the shadow boundary calculated from the full set of Equations (2.1)-(2.5), while the blue solid lines show the results when using Equation (2.7) to calculate the shadow boundary. Calculations are done for distances in the range $d / r_{cyl} = (100 - 10000) \cdot (r_{cyl} / \lambda)$. We see that there is good agreement between the results, with deviations kept within about 5% (see Appendix B).

Note that if increasing the ratio r_{cyl}/λ by a factor ten, i.e., increasing the frequency by a factor ten, then if also increasing the distance behind the cylinder d/r_{cyl} by a factor ten the width of the shadow region remains approximately the same.

Conclusion: Equation (2.7) can be used as a good approximation to calculate the boundary of the shadow region behind an infinitely long conducting cylinder.

5.3 The shadow depth equation

Figure 4.3 shows the reduction in the electric field (shadow depth) behind an infinitely long conducting cylinder for different ratios between the cylinder radius r_{cyl} and the wavelength λ.

Blue lines show the shadow depth calculated from the full set of Equations (2.1)-(2.5), while red lines show results when using Equation (2.12) to calculate the reduction in the electric field. We see that there is good agreement between the results.

Note that the shadow depth increases with increasing r_{cyl}/λ (increasing frequency). For $r_{cyl}/\lambda = 0.1$ (upper left figure) the shadow depth is about 1 dBV/m at a distance of 100 cylinder radii behind the cylinder, increasing to about 20 dBV/m for $r_{cyl}/\lambda = 1000$.

Conclusion: Equation (2.12) can be used as a good approximation to calculate the shadow depth behind an infinitely long conducting cylinder.

5.4 The angular dependency of the electric field

Figure 4.4-Figure 4.8 show the angular dependency of the electric field around an infinitely long conducting cylinder at different distances for frequencies of 100 MHz, 1 GHz, 3 GHz, 9 GHz, and 15 GHz respectively.

The figures show that at all frequencies and distances there is a deep shadow at $\varphi = 180°$, i.e., right behind the cylinder. Outside this region the electric field fluctuates rapidly with much smaller amplitude.

At increasing distance from the cylinder, the shadow becomes less deep, and the *angular* width of the shadow decreases. The electric field outside the shadow region fluctuates more rapidly, but the amplitude of the fluctuations decreases.

For increasing frequency, the shadow becomes deeper and narrower, and the electric field outside the shadow region fluctuates more rapidly. The amplitude of the fluctuating field, however, seems to be independent of the frequency.

Summary: There is a deep shadow behind the cylinder, which becomes deeper and narrower with increasing frequency and decreases with increasing distance. Outside the shadow region

the electric field fluctuates rapidly with much smaller amplitude that decreases with increasing distance.

5.5 Cross-range cuts of the electric field

Figure 4.9-Figure 4.13 show cross-range cuts of the electric field at different distances behind an infinitely long conducting cylinder for frequencies of 100 MHz, 1 GHz, 3 GHz, 9 GHz, and 15 GHz respectively.

The figures confirm that there is a deep but narrow shadow region behind the cylinder, and that outside the shadow region the electric field fluctuates rapidly with much smaller amplitude.

The figures show that the shadow region is symmetric around the center line $y = 0$, and that it contains a local maximum for the electric field at its center ($y = 0$) with one global minimum on each side. The global minima may be several dBV/m lower than the local maximum at $y = 0$, see Table 4.1.

At increasing distance behind the cylinder the shadow region becomes wider, and the distance between the global minima increases. At the same time, the shadow depth decreases, and the local maximum and the global minima become less pronounced. For increasing frequency the shadow becomes deeper and narrower.

The light blue dashed lines in the figures show the electric field when using Equation (2.7) and Equation (2.12) to calculate the shadow boundary and depth. The shadow region is approximated by a square well with width equal to the actual width of the shadow region and depth equal to the shadow depth at $y = 0$. The figures show that the shadow width and "average" or "typical" depth are represented well by Equation (2.7) and Equation (2.12). Information about details within the shadow region is, however, not available in this case.

Summary: The shadow region behind the cylinder is symmetric with a local maximum for the electric field at the center and one global minimum on each side. At increasing distance behind the cylinder the shadow region becomes wider and less deep, and the local maximum and the global minima become less pronounced. Equation (2.7) and Equation (2.12) approximate the shadow region by a square well, and can be used as a good approximation to show the main characteristics of the shadow region.

5.6 The radial dependency of the electric field

Figure 4.14- Figure 4.18 show the electric field as a function of distance for different angles around an infinitely long conducting cylinder for frequencies of 100 MHz, 1 GHz, 3 GHz, 9 GHz, and 15 GHz respectively.

The figures confirm that there is a deep shadow right behind the cylinder ($\varphi = 180°$) that decreases in strength with decreasing distance and increases with increasing frequency.

For angles $\varphi \neq 180°$ the electric field fluctuates rapidly with a much smaller amplitude that decreases somewhat with increasing distance. At 100 MHz the amplitude of the oscillations is about 3 dBV/m at a distance of 10 m in front of the cylinder ($\varphi = 0°$) decreasing to about 1 dBV/m at a distance of 100 m.

How rapidly the electric field fluctuates depends on both the frequency and the angle. In general the field fluctuates slower close to the shadow region (angles close to $\varphi = 180°$).

Summary: There is a deep shadow behind the cylinder ($\varphi = 180°$) that decreases with decreasing distance and increases with increasing frequency. Outside the shadow region the electric field fluctuates rapidly with much smaller amplitude that decreases somewhat with increasing distance.

5.7 The shadow boundary and depth

Table 4.1 gives values for the shadow boundary and depth behind an infinitely long conducting cylinder for frequencies of 100 MHz, 1 GHz, 3 GHz, 9 GHz, and 15 GHz respectively.

Regarding the shadow depth, we see that the value for the electric field $E_z^{tot}(y_{\min})$ at the global minima may be several dBV/m lower than the value $E_z^{tot}(0)$ on-axis. The lower value $E_z^{tot}(y_{\min})$ does, however, apply only over a very small part of the shadow. When discussing the depth of the shadow below we will consider the on-axis value. This corresponds to the value used in the square well representation (see Section 5.5) and represents a good average value for the shadow depth (see Figure 4.9-Figure 4.13).

100 MHz:
At a distance of 10 m behind the cylinder the shadow is about 12 m wide and 13 dBV/m deep. Increasing the distance to 100 m increases the shadow width to 28 m and decreases the depth to 3 dBV/m.

1 GHz:
At a distance of 100 m behind the cylinder the shadow is about 12 m wide and 8 dBV/m deep. Increasing the distance to 1000 m increases the shadow width to 28 m and decreases the depth to 2.5 dBV/m.

3 GHz:
At a distance of 100 m behind the cylinder the shadow is about 9 m wide and 11 dBV/m deep. Increasing the distance to 1000 m increases the shadow width to 16 m and decreases the depth to 4 dBV/m. Increasing the distance further to 5000 m increases the shadow width to 37 m and decreases the depth to 2 dBV/m.

9 GHz:
At a distance of 100 m behind the cylinder the shadow is about 8 m wide and 16 dBV/m deep. Increasing the distance to 1000 m increases the shadow width to 13 m and decreases the depth to 6 dBV/m. Increasing the distance further to 10 000 m increases the shadow width to 30 m and decreases the depth to 2 dBV/m.

15 GHz:
At a distance of 100 m behind the cylinder the shadow is about 7 m wide and 19 dBV/m deep. Increasing the distance to 1000 m increases the shadow width to 10 m and decreases the depth to 8 dBV/m. Increasing the distance further to 10 000 m increases the shadow width to 23 m and decreases the depth to 2.5 dBV/m.

Summary: For the lowest frequencies (100 MHz) the shadow is about 28 m wide and 3 dBV/m deep at a distance of 100 m behind the cylinder. The shadow becomes narrower and deeper for higher frequencies, and at the highest frequencies (15 GHz) the shadow is 19 dBV/m deep but only 7 m wide at the same distance. For distances larger than 10 km the shadow depth is less than 3 dBV/m for all frequencies.

5.8 Shadow effects behind wind turbines

We have assumed that the wind turbine tower is the main source of shadowing, and that the tower can be modeled as an infinitely long conducting cylinder. We have further assumed that the radar is far away from the wind turbine so that the incoming electromagnetic wave can be considered to be a plane wave.

A literature study (Chapter 3) has shown that the infinitely long conducting cylinder model can be used as a good representation of the wind turbine. The cylinder radius should be set equal to the maximum radius of the turbine tower. We have used a cylinder radius of 3 m in our calculations (Chapter 4), which corresponds to a large wind turbine with maximum tower radius 3 m.

Our calculations show that the shadow behind a wind turbine is narrow (about 10 m wide) close to the turbine, but not very deep; the reduction in the electrical field less than 8 dBV/m at distances 1 km or more behind the turbine. The shadow is the widest and the least deep for low frequencies and becomes narrower and deeper for higher frequencies. The shadow increases in width, but decreases in depth, when the distance increases.

The radar's ability to detect targets is not expected to be strongly affected by the shadow effects. The detection of airborne targets is not likely to be affected since airplanes normally operate at higher altitudes and would have to fly low and close to the wind turbines in order to be able to hide behind them. The detection of targets on ground or at sea could be affected to some degree if the target is very close to the wind turbine. However, since the shadow is very narrow the target would have to be quite small in order to be able to hide completely behind

the wind turbine. Larger targets would only be partly covered by the shadow and would still be possible to detect.

The effect of having more than one wind turbine present in the area between the radar and the target has not been investigated in this report. Some information can, however, be found in literature. Trappeniers and Van Lil (4) has studied such a case, and they found that the effect of N wind turbines is always smaller than N times the effect of a single wind turbine. They further found that the shadow effects can be computed without taking into account the presence of other wind turbines in the area as long as the wind turbines do not lie approximately on one line with the radar (parallel case). Poupart (9) found that a line of wind turbines running parallel to the radar's boresight will tend to produce a deeper but narrow shadow due to the cumulative blocking effect of the line of wind turbines, while a line of wind turbines that is offset at an angle to the radar's boresight will tend to produce a wider but less deep radar shadow as the angle increases. He also found that a line of wind turbines perpendicular to the radar's boresight will produce the minimal radar shadow, while a random layout, which in reality is more likely, will produce a combination of the above effects.

Summary: The infinitely long conducting cylinder model can be used as a good representation of the wind turbine. The shadow behind a wind turbine is narrow (about 10 m wide) close to the turbine, but not very deep. Several wind turbines on a line running parallel to the radar's boresight will produce a narrow but deeper shadow, while a line of wind turbines that is offset at an angle to the radar's boresight will tend to produce a wider but less deep shadow as the angle increases. The radar's ability to detect targets will not be significantly affected by the shadow effects, except possibly for small targets that are close to the turbine.

5.9 Summary

We have studied the shadow effects behind wind turbines. The wind turbine can be modelled as an infinitely long conducting cylinder. Calculations have shown that there will be a shadow behind the wind turbine that is narrow (about 10 m wide) close to the turbine, but not very deep. Outside the shadow region, the electric field fluctuates rapidly with much smaller amplitude.

At lower frequencies (100 MHz) the shadow is wider and shallower; 28 m wide and 3 dBV/m deep at a distance of 100 m behind the wind turbine. At higher frequencies (15 GHz) the shadow is narrower and deeper; 7 m wide and 19 dBV/m deep at a distance of 100 m behind the wind turbine. The shadow increases in width and decreases in depth for increasing distance behind the wind turbine. For distances larger than 10 km the shadow depth is less than 3 dBV/m for all relevant frequencies.

Several wind turbines on a line running parallel to the radar's boresight will produce a narrow but deeper shadow, while a line of wind turbines that is offset at an angle to the radar's boresight will tend to produce a wider but less deep shadow as the angle increases.

The radar's ability to detect targets will not be significantly affected by the shadow effects, except possibly for small targets that are close to the turbine.

The derived Equations (2.7) and (2.12) for the shadow boundary and depth can be used as a good approximation to assess the electromagnetic shadow behind a wind turbine.

6 SUMMARY

There is at present a considerable interest in renewable energy sources, and a large number of onshore and offshore wind farms are currently under planning or being developed, both in Norway and in several other countries. Depending on location, the development of a wind farm in a particular area may conflict with Defence interests by degrading the performance of Defence installations such as radars or telecommunications systems. One potential problem is the electromagnetic shadow effect behind wind turbines, which has been studied in this report.

The wind turbine can be modelled as an infinitely long conducting cylinder with radius equal to the maximum tower radius. Calculations have shown that there will be a shadow behind the wind turbine that is narrow (about 10 m wide) close to the turbine, but not very deep. At lower frequencies (100 MHz) the shadow is wider and shallower; 28 m wide and 3 dBV/m deep at a distance of 100 m behind the wind turbine. At higher frequencies (15 GHz) the shadow is narrower and deeper; 7 m wide and 19 dBV/m deep at a distance of 100 m behind the wind turbine. The shadow increases in width and decreases in depth for increasing distance behind the wind turbine. For distances larger than 10 km the shadow depth is less than 3 dBV/m for all relevant frequencies.

Several wind turbines on a line running parallel to the radar's boresight will produce a narrow but deeper shadow, while a line of wind turbines that is offset at an angle to the radar's boresight will tend to produce a wider but less deep shadow as the angle increases.

The radar's ability to detect targets will not be significantly affected by the shadow effects, except possibly for small targets that are close to the turbine.

The calculations based on the infinitely long conducting cylinder model can be quite time consuming, especially for higher frequencies. A new set of equations was therefore derived that can be used to quickly calculate the width and depth of the shadow region behind the wind turbine. Our analyses show that the new set of equations can be used as a good approximation to assess the electromagnetic shadow behind a wind turbine, and that the computing time will be considerably reduced.

APPENDIX

A THE INFINITELY LONG CONDUCTING CYLINDER MODEL

We will in this section present the theory behind the infinitely long conducting cylinder model. The theory is well established and can be found in standard literature.

When an infinitely long conducting cylinder is placed in the path of a propagating electromagnetic wave, a secondary wave will be generated by the cylinder that interferes with the incoming primary wave and creates an interference pattern around the cylinder. In particular, a dark shadow region will be formed behind the cylinder. Figure A.1 shows the geometry of the problem.

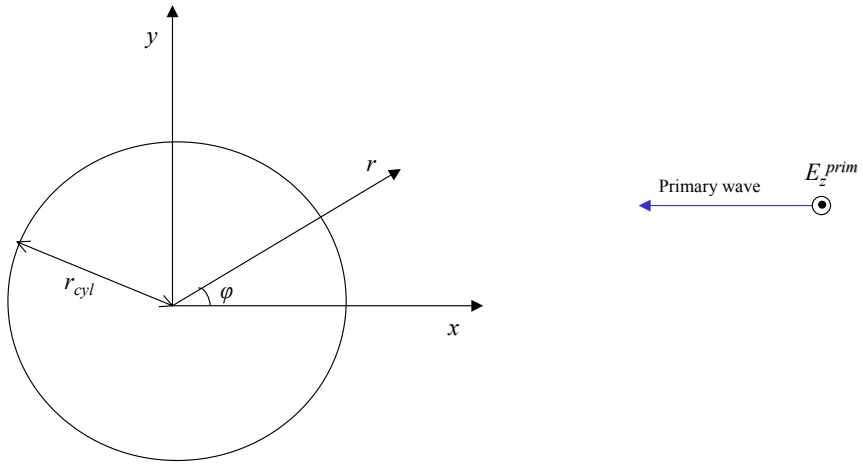

Figure A.1 Diffraction on an infinitely long conducting cylinder (cross-section in the xy-plane).

We assume that the incoming primary wave is a plane wave. This corresponds to the emitter being at far distance from the cylinder. The primary wave E_z^{prim} can then be written:

$$E_z^{prim} = E_0 \cdot e^{jkx} = E_0 \cdot e^{jkr\cos\varphi} \tag{A.1}$$

where E_0 is the electric field amplitude, r is the distance from the cylinder, φ is the angle around the cylinder, and $k = 2\pi / \lambda$ is the wave number with λ being the wavelength. We have assumed that the incoming primary wave has an electric field component along the z-axis only.

We further assume that the electrical field is homogeneous in the z-direction, i.e.,

$$\frac{dE_z^{prim}}{dz} = 0 \tag{A.2}$$

Since the situation is identical for all cross-sections parallel to the xy-plane, the problem can be solved in two dimensions.

The total electrical field at the cylinder surface must at all times be zero in the direction tangential to the cylinder surface, i.e.,

$$E^{tot} = 0, \quad \text{at } r = r_{cyl} \tag{A.3}$$

In order for the boundary condition to be fulfilled, the cylinder must generate a secondary wave E_z^{sec} in response to the incoming primary wave E_z^{prim}. The boundary condition (A.3) can then be expressed as

$$E^{tot} = E_z^{tot} = E_z^{prim} + E_z^{\text{sec}} = 0, \qquad \text{at } r = r_{cyl} \tag{A.4}$$

In order to find the total electrical field E_z^{tot} around the cylinder, we must determine the secondary field E_z^{sec}. The secondary field must fulfil the wave equation

$$\nabla^2 E_z^{\text{sec}} + k^2 E_z^{\text{sec}} = 0 \tag{A.5}$$

where k is a constant. In cylindrical coordinates Equation (A.5) becomes

$$\frac{\partial^2 E_z^{\text{sec}}}{\partial r^2} + \frac{1}{r}\frac{\partial E_z^{\text{sec}}}{\partial r} + \frac{1}{r^2}\frac{\partial^2 E_z^{\text{sec}}}{\partial \varphi^2} + k^2 E_z^{\text{sec}} = 0 \tag{A.6}$$

when $\partial E_z^{\text{sec}} / \partial z = 0$ (see Equation (A.2)).

We assume that the secondary field E_z^{sec} can be expressed as

$$E_z^{\text{sec}} = R(r) \cdot \Phi(\varphi) \tag{A.7}$$

i.e., on a form where the variables r and φ are separated. By substituting Equation (A.7) into Equation (A.6) we get

$$\Phi \frac{d^2 R}{dr^2} + \Phi \frac{1}{r}\frac{dR}{dr} + R\frac{1}{r^2}\frac{d^2\Phi}{d\varphi^2} + k^2 R\Phi = 0 \tag{A.8}$$

Multiplying Equation (A.8) by $r^2 / \Phi R$ further gives

$$\frac{r^2}{R}\frac{d^2 R}{dr^2} + \frac{r}{R}\frac{dR}{dr} + k^2 r^2 = -\frac{1}{\Phi}\frac{d^2\Phi}{d\varphi^2} \tag{A.9}$$

In order for Equation (A.9) to be valid for any arbitrary combination of r and φ, each side of the equation must be equal to a constant. We set the constant equal to m^2 and can then write down the following two separate equations:

$$\frac{d^2\Phi}{d\varphi^2} + m^2\Phi = 0 \tag{A.10}$$

$$\frac{r^2}{R}\frac{d^2R}{dr^2} + \frac{r}{R}\frac{dR}{dr} - m^2 + k^2r^2 = 0 \tag{A.11}$$

We first consider Equation (A.10). This is a second-order differential equation with constant coefficients that has the solution

$$\Phi = C\cos(m\varphi + \varphi_0) \tag{A.12}$$

where C and φ_0 are constants. Due to the axial symmetry of the problem, the direction for $\varphi = 0$ can be chosen arbitrarily, and we choose to set $\varphi_0 = 0$, which gives

$$\Phi = C\cos(m\varphi) \tag{A.13}$$

Here m must be an integer, since the solution for $\Phi(\varphi = 0)$ must equal the solution for $\Phi(\varphi = 2\pi, 4\pi, \ldots)$.

We then consider Equation (A.11). Substituting $\rho = kr$ into Equation (A.11) and rearranging the equation gives

$$\frac{d^2R}{d\rho^2} + \frac{1}{\rho}\frac{dR}{d\rho} + \left(1 - \frac{m^2}{\rho^2}\right)R = 0 \tag{A.14}$$

where m is an integer. Equation (A.14) is a Bessel equation with solution

$$R = D \cdot H_m^{(2)}(\rho) = D \cdot H_m^{(2)}(kr) \tag{A.15}$$

where $H_m^{(2)}$ is the Hankel function of second kind, and D is a constant.

The solution for the secondary field E_z^{sec} can now be written

$$E_z^{\text{sec}} = R(r)\Phi(\varphi) = A_m H_m^{(2)}(kr)\cos(m\varphi) \tag{A.16}$$

where A_m is a constant, and m is an integer.

The general solution for E_z^{sec} is a linear combination of the solution (A.16) for all possible values of m, and can be written

$$E_z^{\text{sec}} = \sum_{m=0}^{\infty} A_m H_m^{(2)}(kr)\cos(m\varphi) \tag{A.17}$$

The coefficients A_m are determined from the boundary condition (A.4). Substituting for E_z^{prim} and E_z^{sec} in the boundary condition gives

$$E_0 e^{jkr_{cyl}\cos\varphi} + \sum_{m=0}^{\infty} A_m H_m^{(2)}(kr_{cyl})\cos(m\varphi) = 0 \tag{A.18}$$

Since

$$e^{jkr_{cyl}\cos\varphi} = J_0(kr_{cyl}) + \sum_{m=1}^{\infty} 2j^m J_m(kr_{cyl})\cos(m\varphi) \tag{A.19}$$

Equation (A.18) can be rewritten

$$\left[E_0 J_0(kr_{cyl}) + A_0 H_0^{(2)}(kr_{cyl})\right] + \sum_{m=1}^{\infty}\left[2E_0 j^m J_m(kr_{cyl})\cos(m\varphi) + A_m H_m^{(2)}(kr_{cyl})\cos(m\varphi)\right] = 0 \tag{A.20}$$

For each value of m the corresponding terms in Equation (A.20) must add up to zero, and this gives for the coefficients A_m

$$A_0 = -\frac{E_0 J_0(kr_{cyl})}{H_0^{(2)}(kr_{cyl})} \tag{A.21}$$

and

$$A_m = -2j^m E_0 \frac{J_m(kr_{cyl})}{H_m^{(2)}(kr_{cyl})} \tag{A.22}$$

The summation in Equation (A.17) for the secondary field can be terminated when $m = M$, where M is given by (see Appendix C)

$$M = \text{ceil}\left[10 + 6.4 \cdot \left(\frac{r_{cyl}}{\lambda}\right)\right] \tag{A.23}$$

Equation (A.23) is valid for $r_{cyl} / \lambda \le 1000$.

B BOUNDARY AND DEPTH OF THE SHADOW REGION

We will in this section derive equations that can be used to quickly calculate the shadow boundary and depth behind an infinitely long conducting cylinder.

B.1 The shadow boundary equation

We define the shadow boundary to be the closest cross-range distance y_b at given distance d behind the cylinder where the electric field E_z^{tot} is equal to the unperturbed electric field. We have calculated the shadow boundary for different r_{cyl}/λ based on Equations (2.1)-(2.5), see Figure B.2 (blue circles). The shadow boundary has the shape of a parabola, which mathematically can be expressed as

$$D = w \cdot Y^2 \tag{B.1}$$

where $D = d / r_{cyl}$ is the distance behind the cylinder (measured in cylinder radii), $Y = y_b / r_{cyl}$ is the cross-range distance to the boundary (measured in cylinder radii), and w is a parameter that is a constant for given r_{cyl}/λ . Equation (B.1) can be rearranged on the form

$$y_b(d) = \sqrt{\frac{d \cdot r_{cyl}}{w}} \tag{B.2}$$

where r_{cyl} is the cylinder radius.

We must determine the optimum value $w = w_0$ that gives the best fit to the shadow boundary for each r_{cyl}/λ. Table B.1 and Figure B.1 show the results for w_0, while Figure B.2 shows the resulting shadow boundary for different r_{cyl}/λ when using $w = w_0$ (blue solid line). The data have been fitted for distances in the range $d / r_{cyl} = (100 - 10000) \cdot (r_{cyl}/\lambda)$.

x	***w₀***	***w***	**Δy_b (%)**
0.1	0.185	0.175	2.8
1	1.50	1.60	3.2
10	13.8	14.6	2.8
100	136	133	1.1
1000	1355	1214	5.6

Table B.1 *The parameter w for different r_{cyl}/λ. The column marked by w_0 shows the optimum values, while the column marked by w shows the resulting values when using Equations (B.4)-(B.5). The last column shows the deviation in the cross-range distance to the boundary y_b when using Equations (B.4)-(B.5) to calculate w instead of using the optimum value w_0.*

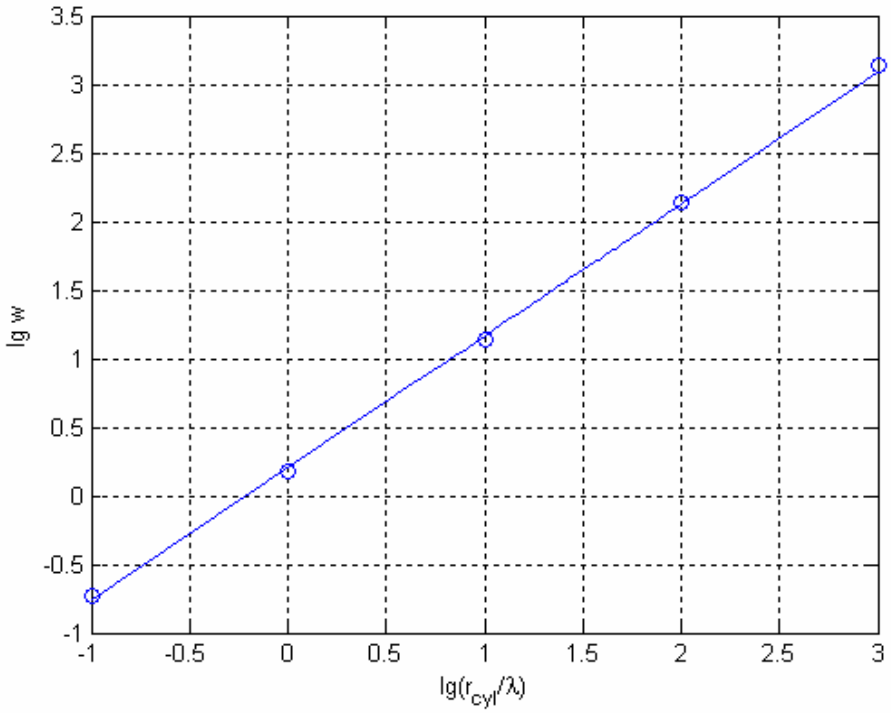

Figure B.1 *The parameter w as a function of r_{cyl}/λ. Blue circles show the results when $w=w_0$ (optimum value) while the blue solid line shows the results when using Equations (B.4)-(B.5) to calculate w.*

In order to use Equation (B.2) for an arbitrary choice of r_{cyl}/λ, we must express w as a function of r_{cyl}/λ. Figure B.1 shows that $\lg w$ is very close to a linear function of $\lg(r_{cyl}/\lambda)$. We can then write

$$\lg w = k \lg\left(\frac{r_{cyl}}{\lambda}\right) + \lg g \tag{B.3}$$

where k and g are constants. Equation (B.3) can be rearranged on the form

$$w = g \cdot \left(\frac{r_{cyl}}{\lambda}\right)^k \tag{B.4}$$

The values of k and g that give the best fit for w as a function of r_{cyl}/λ (see Figure B.1) were found to be

$$\begin{aligned} k &= 0.96 \\ g &= 1.6 \end{aligned} \tag{B.5}$$

Figure B.2 shows the shadow boundary for different r_{cyl}/λ, when using Equation (B.2) with w given by Equations (B.4)-(B.5) (red solid lines).

The deviation in the cross-range distance to the boundary Δy_b, when using Equations (B.4)-(B.5) to calculate w instead of using the optimum value w_0, can be calculated from

$$\Delta y_b = \left| 1 - \sqrt{\frac{w_0}{w}} \right| \tag{B.6}$$

The deviation is found to be well below 5% in all cases (see Table B.1), except when $r_{cyl} / \lambda = 1000$ where the deviation is 5.6%.

Equation (B.2) has been optimized for distances in the range $d / r_{cyl} = (100 - 10000) \cdot (r_{cyl} / \lambda)$. Calculations show that Equation (B.2) can be used as a good approximation also for larger distances, while for distances $d \le d_0$ where

$$d_0 = \begin{cases} 5 r_{cyl} \cdot \left(\dfrac{r_{cyl}}{\lambda} \right), & \dfrac{r_{cyl}}{\lambda} > 1 \\ 5 r_{cyl}, & \dfrac{r_{cyl}}{\lambda} \le 1 \end{cases} \tag{B.7}$$

Equation (B.2) gives a too narrow shadow, see Figure B.3. For distances $d \le d_0$ the following expression can be used to approximate the shadow boundary instead of Equation (B.2)

$$y_b^{d \le d_0}(d) = r_{cyl} + \left(\frac{y_b(d_0) - r_{cyl}}{d_0} \right) \cdot d \tag{B.8}$$

where $y_b(d_0)$ is calculated from Equation (B.2). This corresponds to a linearly increasing shadow boundary that starts with the value r_{cyl} at $d = 0$ and increases to $y_b(d_0)$ at $d = d_0$.

The equation for the shadow boundary Y_b can now be summarized as

$$Y_b = \pm \begin{cases} y_b(d), & d > d_0 \\ r_{cyl} + \left(\dfrac{y_b(d_0) - r_{cyl}}{d_0} \right) \cdot d, & d \le d_0 \end{cases} \tag{B.9}$$

where $y_b(d)$ is given by Equation (B.2).

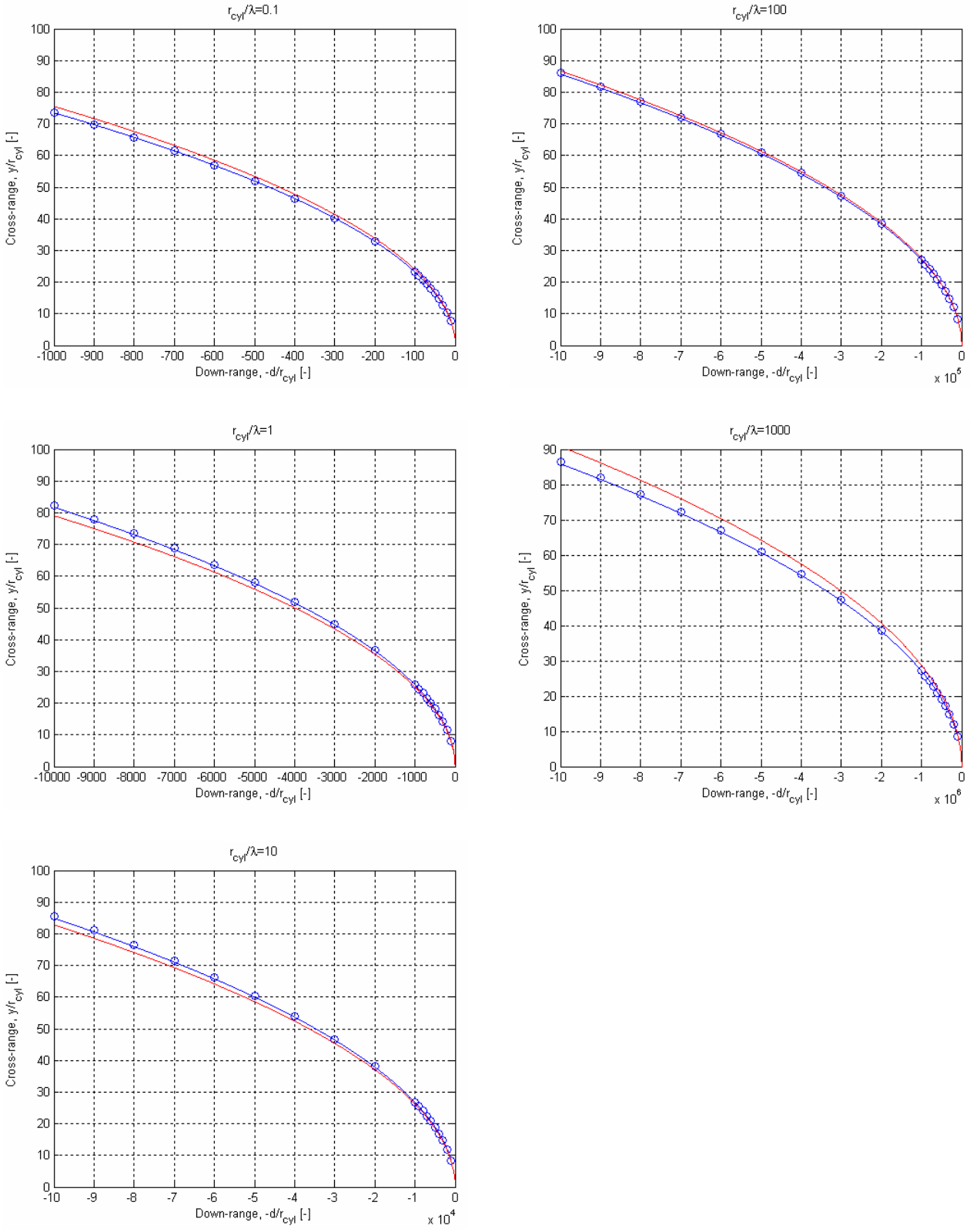

Figure B.2 *The shadow boundary for different r_{cyl}/λ. Blue circles show the results when using Equations (2.1)-(2.5), the blue solid line shows the results when using Equation (B.2) with the optimum value w_0, and the red solid line shows the results when using Equation (B.2) with w given by Equations (B.4)-(B.5).*

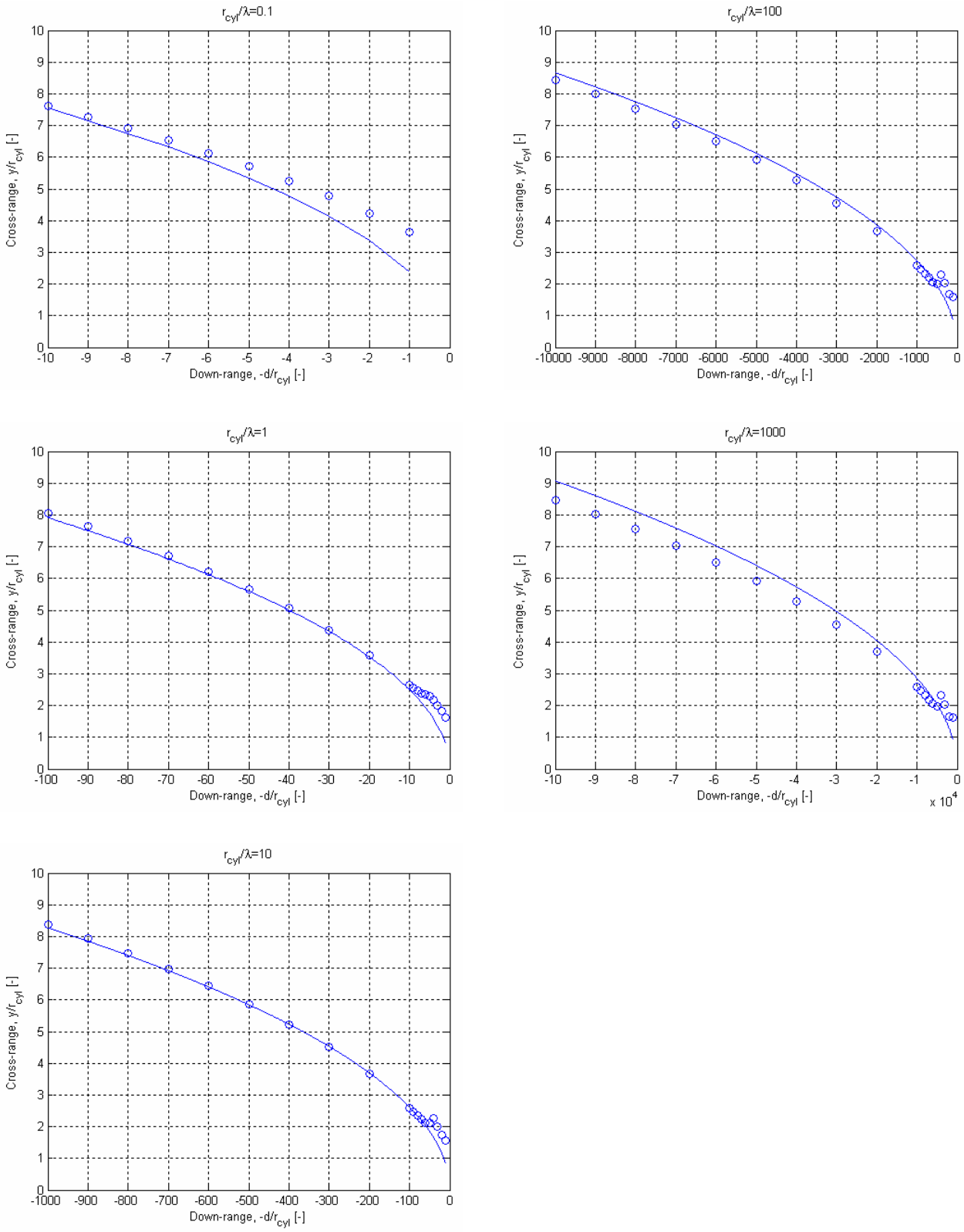

Figure B.3 *The shadow boundary for different r_{cyl}/λ. Blue circles show the results when using Equations (2.1)-(2.5), while the blue solid line shows results when using Equation (B.2) with w given by Equations (B.4)-(B.5).*

B.2 The shadow depth equation

The shadow depth, or reduction in the electric field, behind an infinitely long conducting cylinder can be calculated from Equations (2.1)-(2.5). Figure B.6 shows the resulting shadow depth for different r_{cyl}/λ (blue lines). The shape of the curves can be described by the following expression

$$20\lg E_z^{tot} = a \cdot \left(\frac{d}{r_{cyl}} \right)^{-b} \tag{B.10}$$

where r_{cyl} is the cylinder radius, d is the distance behind the cylinder, and a and b are parameters that are constant for given r_{cyl}/λ .

We must determine the values $a = a_0$ and $b = b_0$ that give the best fit to the shadow depth curve for each r_{cyl}/λ. Table B.2, Figure B.4 and Figure B.5 show the results for a_0 and b_0, while Figure B.6 shows the resulting shadow depth for different r_{cyl}/λ when using $a = a_0$ and $b = b_0$ (blue line).

x	***a₀***	***b₀***
0.1	-17.4646	0.5898
0.5	-21.5465	0.5825
1	-25.3020	0.5761
5	-38.9569	0.5416
10	-46.2652	0.5152
50	-64.8636	0.4422
100	-74.8539	0.4186
500	-111.1654	0.4064
1000	-136.1693	0.4184

Table B.2 The parameters a_0 and b_0 for different r_{cyl}/λ.

In order to use Equation (B.10) for an arbitrary choice of r_{cyl}/λ, we must express a and b as a function of r_{cyl}/λ. Figure B.4 shows that $\lg a$ can be approximated as a linear function of $\lg(r_{cyl}/\lambda)$. We can then write

$$\lg a = s \lg\left(\frac{r_{cyl}}{\lambda} \right) + \lg u \tag{B.11}$$

where s and u are constants. Equation (B.11) can be rearranged on the form

$$a = u \cdot x^s \tag{B.12}$$

The values of s and u that give the best fit for a as a function of r_{cyl}/λ (see Figure B.4) were found to be

$$\begin{aligned} u &= -27.714 \\ s &= 0.22298 \end{aligned} \tag{B.13}$$

Figure B.5 shows $\lg b$ as a function of $\lg(r_{cyl}/\lambda)$. We found that the parameter b can be expressed as

$$\lg b = q_3 \cdot \left[\lg\left(r_{cyl}/\lambda\right)\right]^3 + q_2 \cdot \left[\lg\left(r_{cyl}/\lambda\right)\right]^2 + q_1 \cdot \lg\left(r_{cyl}/\lambda\right) + q_0 \tag{B.14}$$

where q_0, q_1, q_2, and q_3 are constants. The values of q_0 - q_3 that give the best fit for b as a function of r_{cyl}/λ (see Figure B.5) were found to be

$0.1 \le \frac{r_{cyl}}{\lambda} \le 10$:

$$\begin{aligned} q_0 &= -0.2395 \\ q_1 &= -0.02645 \\ q_2 &= -0.01852 \\ q_3 &= -0.003527 \end{aligned} \tag{B.15}$$

and

$10 < \frac{r_{cyl}}{\lambda} \le 1000$:

$$\begin{aligned} q_0 &= -0.2395 \\ q_1 &= 0.01692 \\ q_2 &= -0.08798 \\ q_3 &= 0.02256 \end{aligned} \tag{B.16}$$

Figure 4.3 in Section 4.3 shows the shadow depth for different r_{cyl}/λ, when using Equation (B.10) with a and b given by Equations (B.12)-(B.13) and Equations (B.14)-(B.16) (red lines).

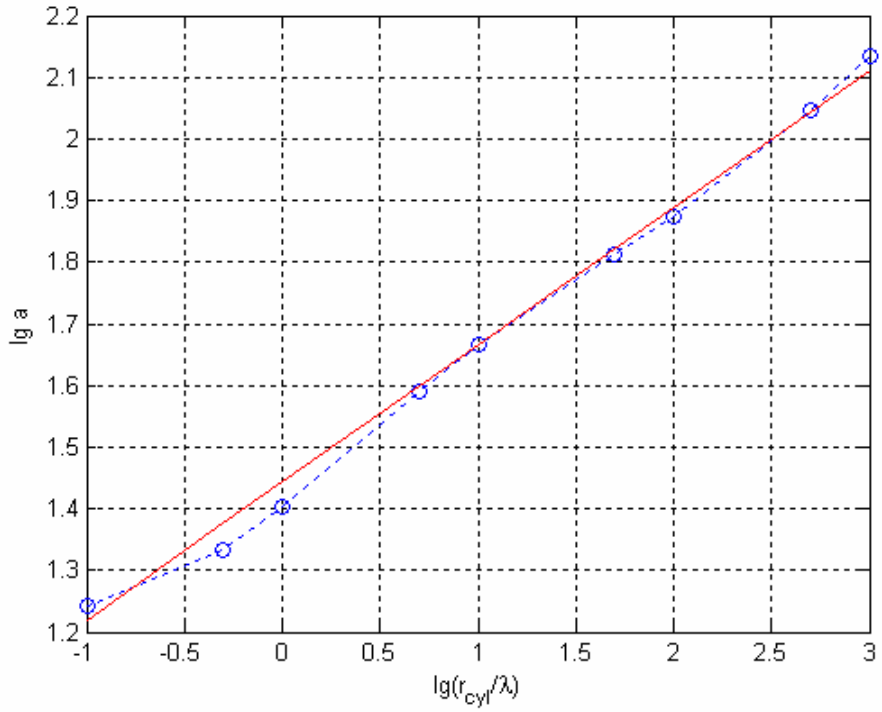

Figure B.4 *The parameter a as a function of r_{cyl}/λ. Blue circles show the results when $a=a_0$ (optimum value), while the red line shows the results when using Equations (B.12)-(B.13) to calculate a.*

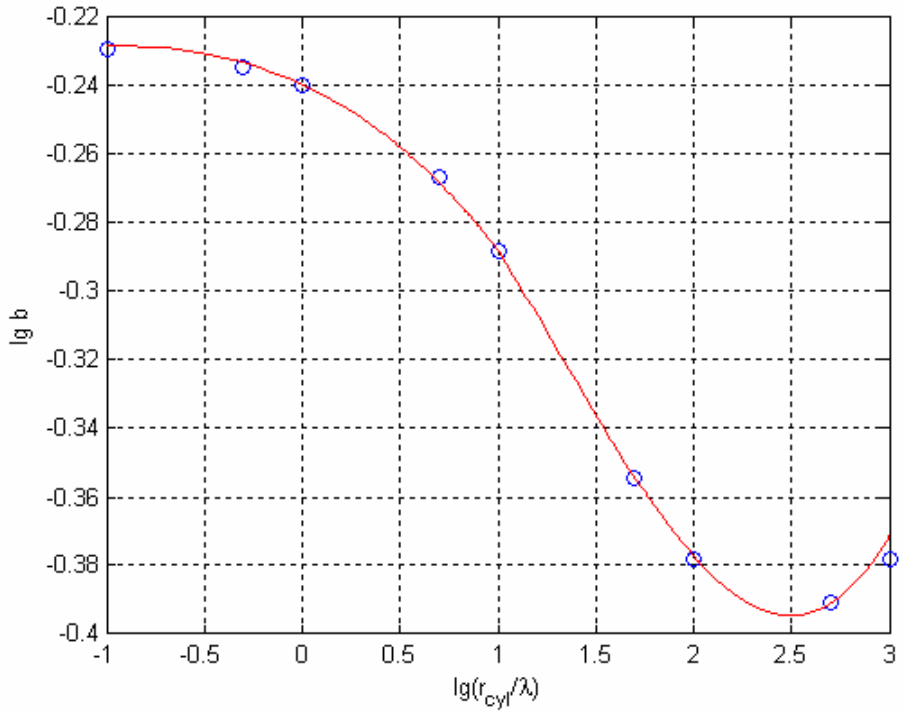

Figure B.5 *The parameter b as a function of r_{cyl}/λ. Blue circles show the results when $b=b_0$ (optimum value), while the red line shows the results when using Equations (B.14)-(B.16) to calculate b.*

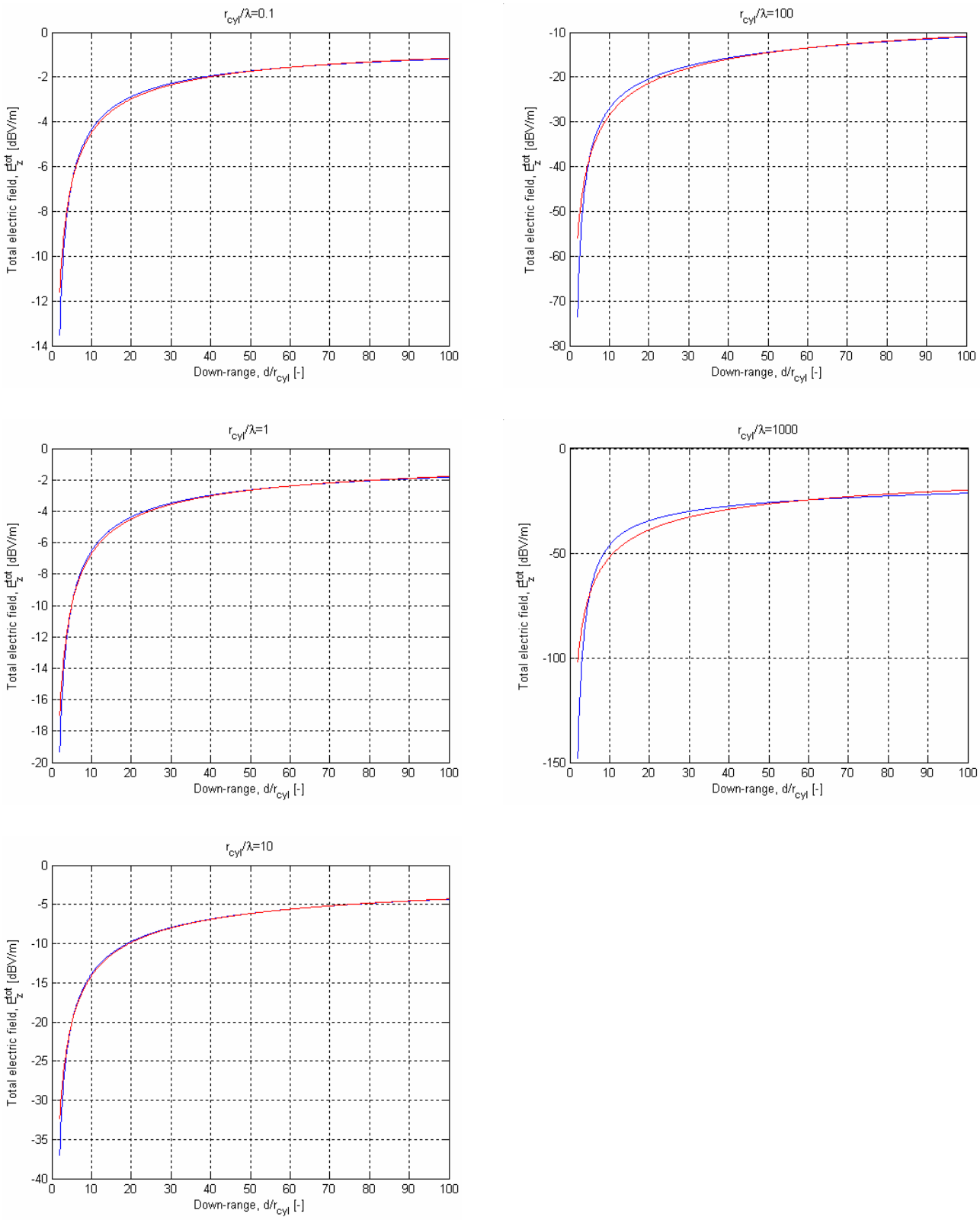

Figure B.6 *The shadow depth for different r_{cyl}/λ. Blue line shows the results when using Equations (2.1)-(2.5), and the red line shows the results when using Equation (B.10) with the optimum values $a=a_0$ and $b=b_0$.*

C TERMINATION OF THE SUMMATION IN THE SECONDARY FIELD EQUATION

It is important to determine as precisely as possible where to terminate the summation for the secondary field in the equation set (2.1)-(2.5) for the infinitely long conducting cylinder model, in order to minimize the computing time.

We will in the following show that the necessary number of terms M to include depends only on the ratio $\left(r_{cyl}/\lambda\right)$, and that M can be calculated from

$$M = \text{ceil}\left[10 + 6.4 \cdot \left(\frac{r_{cyl}}{\lambda}\right)\right] \tag{C.1}$$

Equation (C.1) is valid for $r_{cyl}/\lambda \le 1000$.

C.1 The secondary field equation

The secondary field E_z^{sec} can be written on the form:

$$\begin{aligned} E_z^{\text{sec}} &= \sum_{m=0}^{\infty} {}_m E_z^{\text{sec}} \\ &= \sum_{m=0}^{\infty} \left[\text{Re}\left({}_m E_z^{\text{sec}} \right) + j \cdot \text{Im}\left({}_m E_z^{\text{sec}} \right) \right] \\ &= \sum_{m=0}^{\infty} \text{Re}\left({}_m E_z^{\text{sec}} \right) + j \cdot \sum_{m=0}^{\infty} \text{Im}\left({}_m E_z^{\text{sec}} \right) \\ &\approx \sum_{m=0}^{M} \text{Re}\left({}_m E_z^{\text{sec}} \right) + j \cdot \sum_{m=0}^{M} \text{Im}\left({}_m E_z^{\text{sec}} \right) \end{aligned} \tag{C.2}$$

where M is an integer of finite size, and (ref. Equation (2.3))

$${}_m E_z^{\text{sec}} = A_m H_m^{(2)}(kr)\cos(m\varphi) \tag{C.3}$$

Here r is the distance from the cylinder, φ is the angle around the cylinder (see Figure 2.6), $H_m^{(2)}$ are Hankel functions of the second kind, and the coefficients A_m are given by

$$A_0 = -\frac{E_0 J_0(kr_{cyl})}{H_0^{(2)}(kr_{cyl})} \tag{C.4}$$

and

$$A_m = -2 j^m E_0 \frac{J_m(kr_{cyl})}{H_m^{(2)}(kr_{cyl})} \tag{C.5}$$

where E_0 is the electric field amplitude of the primary wave, $k = 2\pi / \lambda$ is the wave number with λ being the wavelength, and r_{cyl} is the cylinder radius.

The m th component of the secondary field ${}_m E_z^{\text{sec}}$ can then be written on the form

$$ {}_m E_z^{\text{sec}} = a_m \cdot J_m(x) \cdot \frac{H_m^{(2)}(qx)}{H_m^{(2)}(x)} \cdot \cos(m\varphi) \tag{C.6} $$

where

$$ x = 2\pi \cdot \left(\frac{r_{cyl}}{\lambda} \right) \tag{C.7} $$

$$ q = \frac{r}{r_{cyl}} $$

and

$$ a_0 = -E_0 \tag{C.8} $$

$$ a_m = -2 j^m E_0 $$

In the following, we will consider each factor in Equation (C.6) separately in order to determine its contribution to determining M .

C.1.1 The coefficient a_m

The coefficient a_m can be considered a constant

$$ | a_m | = 2E_0 \tag{C.9} $$

for all $m \geq 1$, and does not influence the choice of M .

C.1.2 The cosinus-factor

The cosinus-factor $\cos(m\varphi)$ has the absolute value

$$ | \cos(m\varphi) | \leq 1 \tag{C.10} $$

for all m and φ, and varies cyclically between –1 and 1 as a function of m, see Figure C.1. The cosinus-factor does not influence the choice of M.

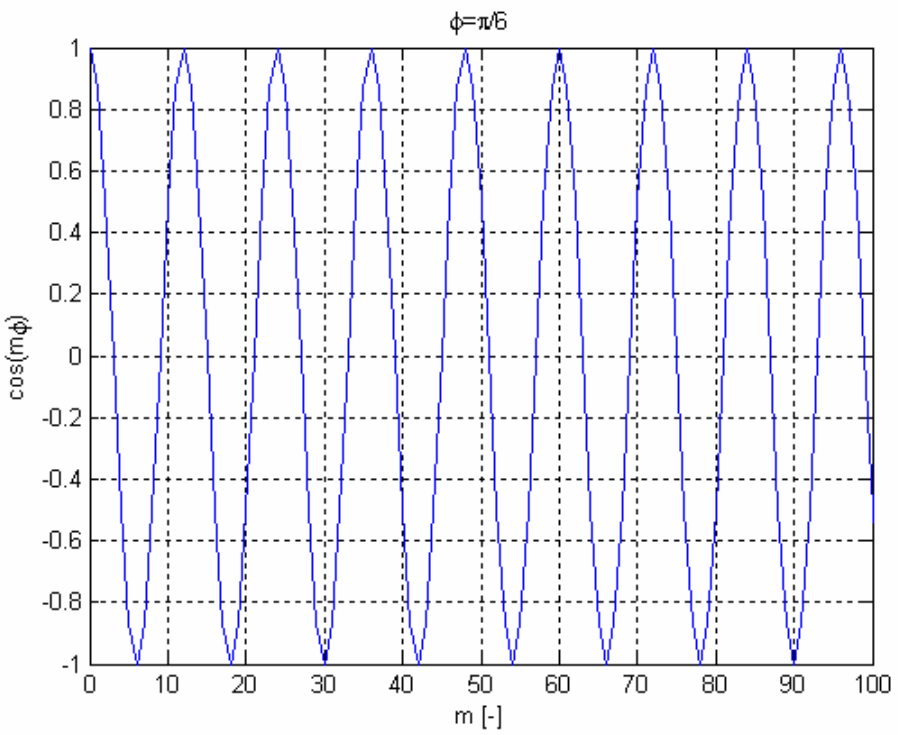

Figure C.1 The cosinus-factor as a function of m when $\varphi = \pi / 6$.

C.1.3 The Hankel-factor

The Hankel-factor $H_m^{(2)}(qx) / H_m^{(2)}(x)$ is a function of $q = r / r_{cyl}$ and $x = 2\pi r_{cyl} / \lambda$. Figure C.2 and Figure C.3 show the Hankel-factor as a function of q for different m when $x = 0.1$ and $x = 10$ respectively.

For given q and x the Hankel-factor is a constant for all $m \geq m_h$. Here m_h is a positive integer, and the value of m_h depends on x. For $x \geq 10$ we have $m_h = 0$, i.e., the Hankel-factor is constant for all m (see Figure C.3), while for $x = 0.1$ we have $m_h = 5$ (see Figure C.2). In general, m_h increases with decreasing x.

Since the Hankel-factor is very nearly a constant with respect to m (except for the lowest m when $x < 10$), the Hankel-factor will not influence the choice of M. This also means that the relative distance $q = r / r_{cyl}$ does not affect the choice of M, since $q = r / r_{cyl}$ only appears in the Hankel-factor in the expression for the secondary field ${}_m E_z^{\text{sec}}$ (Equation C.6). The results shown in Table C.2-Table C.13 confirm this.

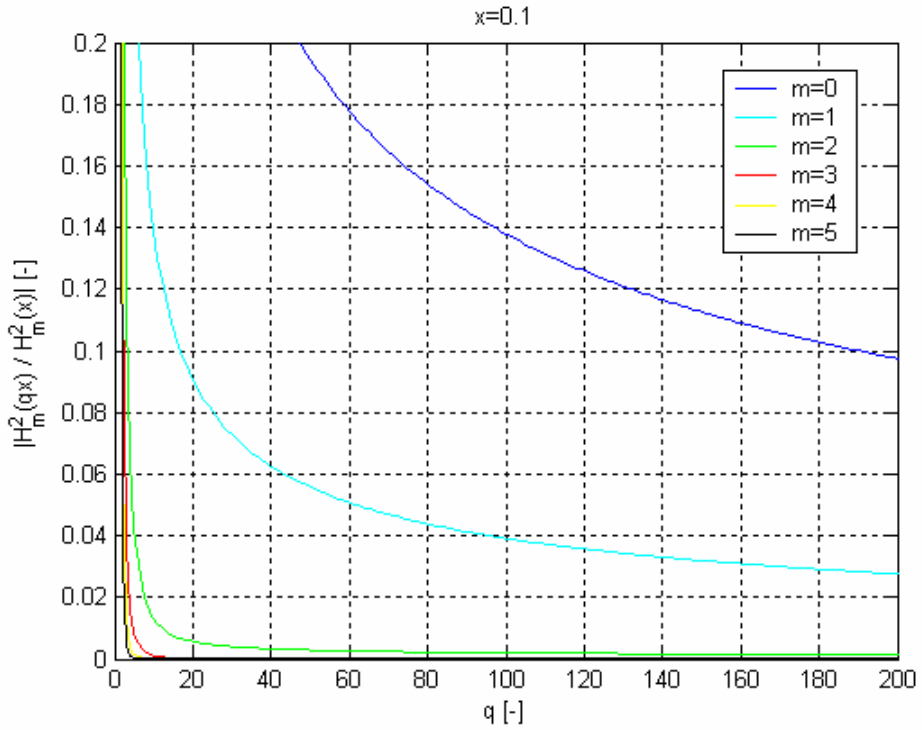

Figure C.2 The Hankel-factor as a function of q for different m when x=0.1.

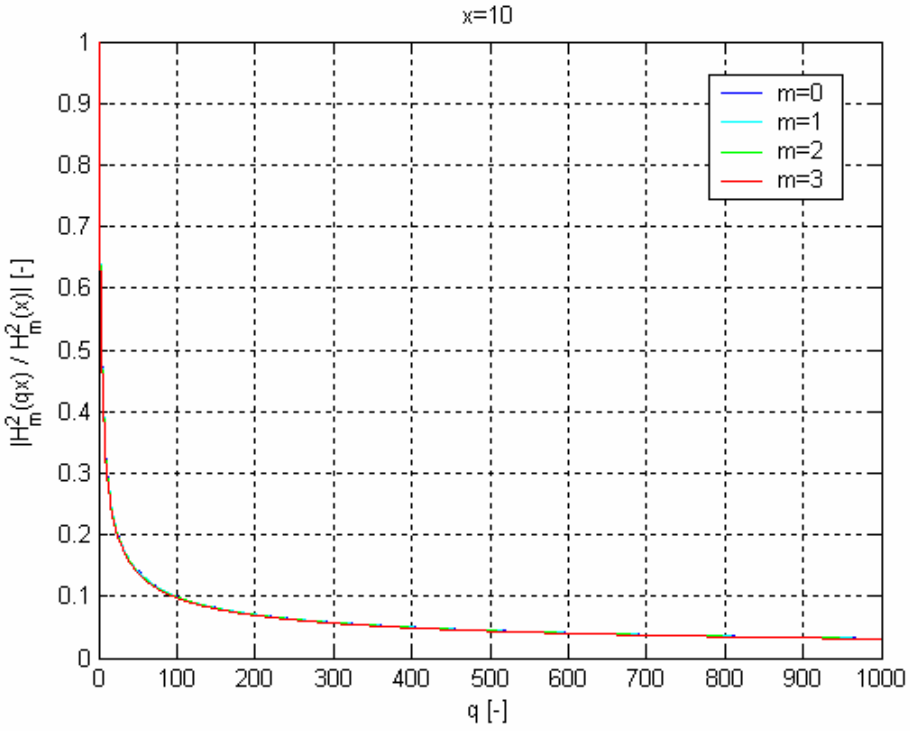

Figure C.3 The Hankel-factor as a function of q for different m when x=10.

C.1.4 The Bessel function

The Bessel function $J_m(x)$ in the expression for the secondary field ${}_mE_z^{sec}$ (Equation C.6) is a function of $x = 2\pi r_{cyl} / \lambda$. Figure C.4 and Figure C.5 show the Bessel function for different m. From the figures we see that for given x the Bessel function becomes negligible when $m > m_J$, where m_J is a positive integer. The figures further show that m_J increases for increasing x. Based on this, we conclude that there is a correspondence between the value of x, i.e., the ratio r_{cyl} / λ, and the number of terms M that must be included in the calculations.

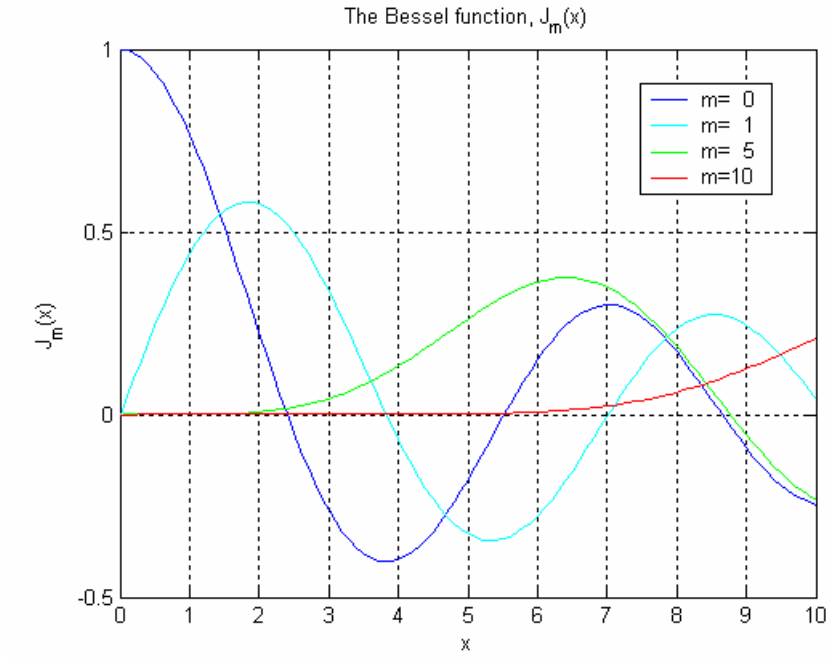

Figure C.4 The Bessel function as a function of x for different m.

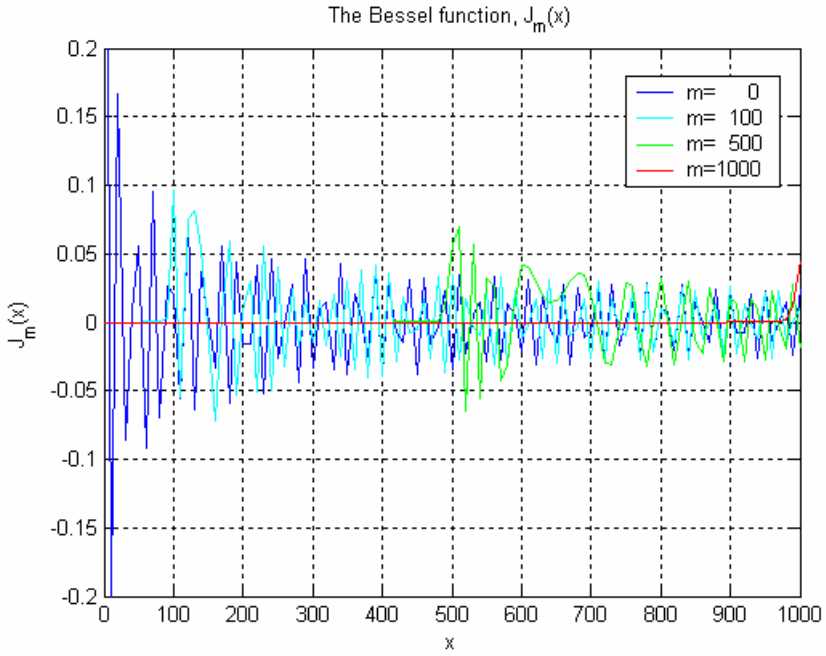

Figure C.5 The Bessel function as a function of x for different m.

C.2 Method

The method used to determine the appropriate value M for terminating the summation in the equation for the secondary field ${}_mE_z^{\text{sec}}$ is described below. We first set

$$E_0 = 1 \text{ V/m}$$
$$\varphi = \pi \tag{C.11}$$

The m^{th} component of the secondary field can then be written

$${}_mE_z^{\text{sec}} = a_m \cdot J_m\left(\tfrac{2\pi r}{\lambda}\right) \cdot \frac{H_m^{(2)}\left(\tfrac{r}{r_{cyl}} \cdot \tfrac{2\pi r}{\lambda}\right)}{H_m^{(2)}\left(\tfrac{2\pi r}{\lambda}\right)} \tag{C.12}$$

where

$$a_0 = 1$$
$$a_m = -2 \cdot (-j)^m, \quad m \geq 1 \tag{C.13}$$

The following algorithm is used to determine M for different values of r_{cyl}/λ and r/r_{cyl}:

- Calculate $|\,{}_mE_z^{\text{sec}}\,|$ for $m = 0,1,...,m_{\max}$, where $m_{\max} > M$.
- Determine the maximum value $|\,{}_mE_z^{\text{sec}}\,|_{\max}$ within the range $m = 0,1,...,m_{\max}$.
- Calculate $|\,{}_mE_z^{\text{sec}}\,| / |\,{}_mE_z^{\text{sec}}\,|_{\max}$ for all $m = 0,1,...,m_{\max}$.
- Determine the highest $m = m_{\text{limit}}$ for which $|\,{}_mE_z^{\text{sec}}\,| / |\,{}_mE_z^{\text{sec}}\,|_{\max} \geq p$, where p is a given percentage of the maximum value. We have used $p = 0.01$ (1%) in the calculations.
- Repeat the steps above for $|\text{Re}({}_mE_z^{\text{sec}})|$ and $|\text{Im}({}_mE_z^{\text{sec}})|$.
- Determine M from $M = \max(m_{\text{limit}}^{|{}_mE_z^{\text{sec}}|},\ m_{\text{limit}}^{|\text{Re}({}_mE_z^{\text{sec}})|},\ m_{\text{limit}}^{|\text{Im}({}_mE_z^{\text{sec}})|})$.

C.3 Results

Results from the calculations are presented in Figure C.6-Figure C.8 and Table C.1-Table C.13.

C.3.1 The secondary field as a function of *m*

Figure C.6-Figure C.8 show the secondary field (normated value) as a function of m when $r_{cyl}/\lambda = 10$. Both total, real, and imaginary part of the secondary field are shown. The green dotted line in the figures indicates the value of p (=0.01). We see that the value for the secondary field drops markedly right before reaching $m = M$ (=69 when $r_{cyl}/\lambda = 10$, see Table C.1) and stays close to zero after that. This confirms our assumption that the summation in the secondary field equation can be terminated for $m = M$ without causing significant errors.

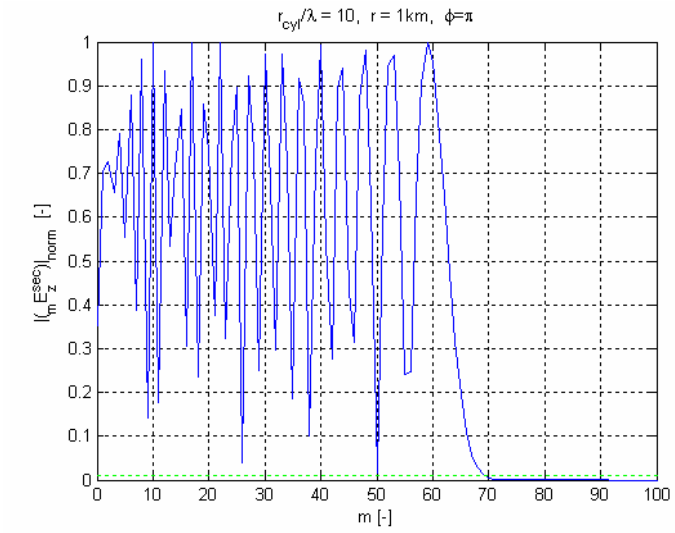

Figure C.6 *The secondary field as a function of m when* $r_{cyl} / \lambda = 10$.

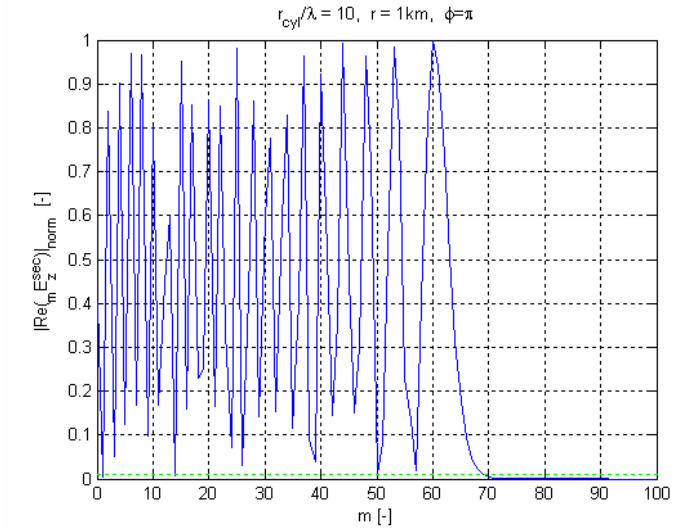

Figure C.7 *Real part of the secondary field as a function of m when* $r_{cyl} / \lambda = 10$.

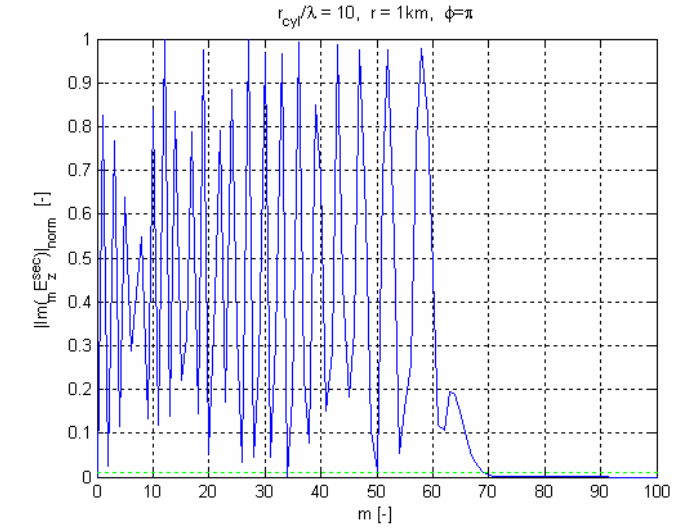

Figure C.8 *Imaginary part of the secondary field as a function of m when* $r_{cyl} / \lambda = 10$.

C.3.2 Determining M

We have determined M for different r_{cyl} / λ based on the method described in Section C.2. Results are shown in Table C.2-Table C.13, with a summary given in Table C.1.

We have also calculated M from Equation (C.1) for comparison. Results are shown in Table C.1 and Figure C.9-Figure C.10.

Table C.1 and Figure C.9-Figure C.10 show that M increases nearly linearly with r_{cyl} / λ, and that Equation (C.1) can be used as a good approximation to calculate M. Note that Equation (C.1) gives slightly higher values for M than the method described in Section C.2. This is done intentionally, in order to ensure that sufficiently many terms are included in the calculations when using Equation (C.1).

r_{cyl}/λ	M	M^*
0.1	2	11
1	9	17
5	36	42
10	69	74
25	165	170
50	325	330
75	483	490
100	642	650
250	1589	1610
500	3165	3210
750	4739	4810
1000	6313	6410

Table C.1 M for different values of r_{cyl}/λ. In the second column M is determined based on the method described in Section C.2. In the last column, M^* is calculated from Equation (C.1).

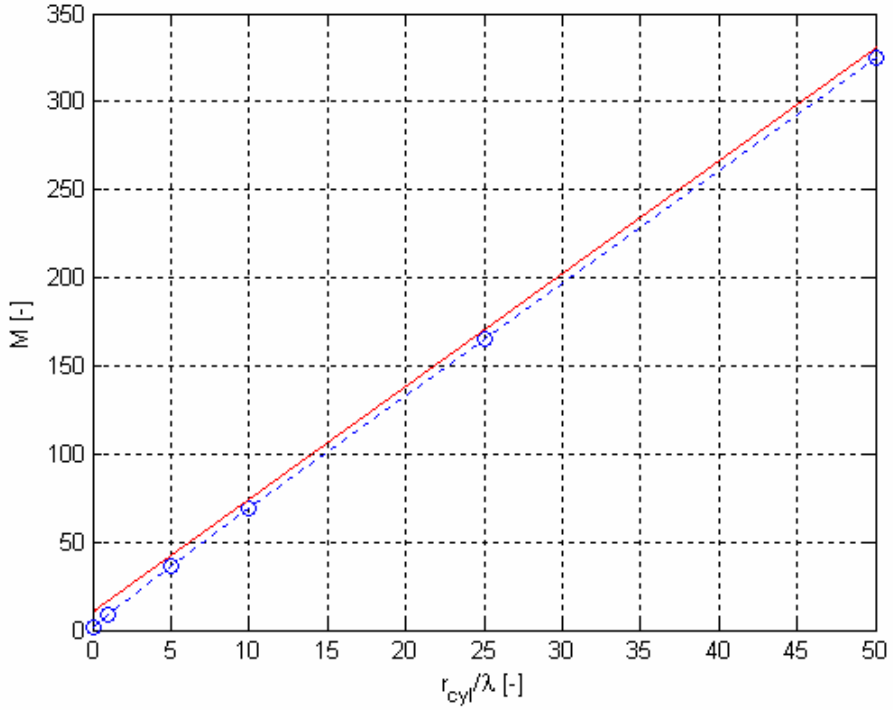

Figure C.9 *M as a function of r_{cyl}/λ. The blue circles show the results from calculations after the method described in Section C.2, while the red line shows results from calculations with Equation (C.1).*

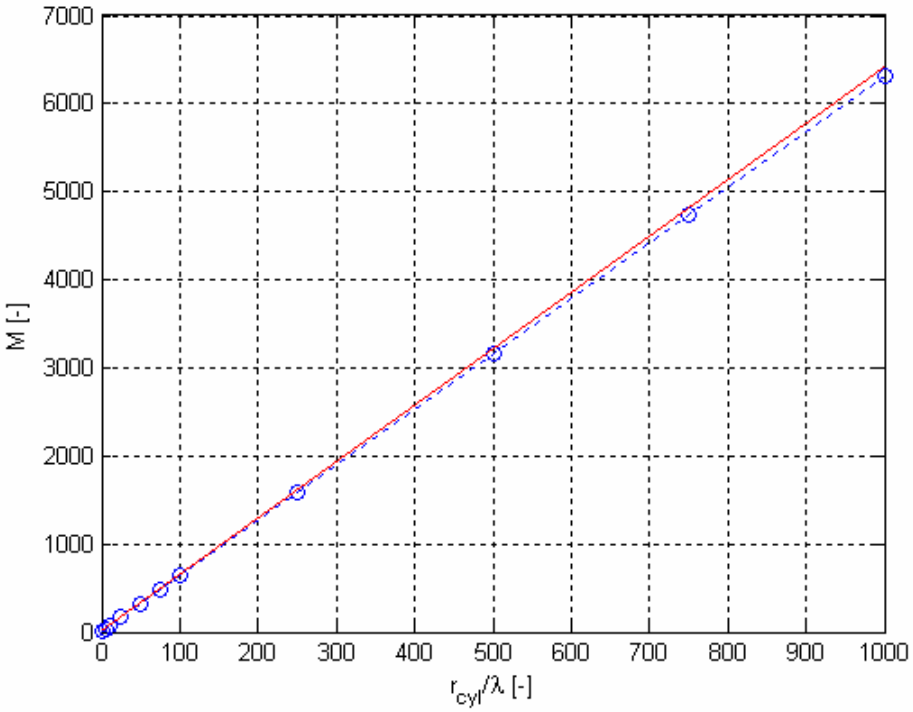

Figure C.10 *M as a function of r_{cyl}/λ. The blue circles show the results from calculations after the method described in Section C.2, while the red line shows results from calculations with Equation (C.1).*

r/r_{cyl}	m_{limit}			M
	$\mathrm{Re}(E_z^{sec})$	$\mathrm{Im}(E_z^{sec})$	$\lvert E_z^{sec}\rvert$	
2.5	2	2	2	**2**
5	1	2	2	**2**
50	2	2	2	**2**
500	2	2	2	**2**
5 000	2	2	2	**2**
50 000	2	2	2	**2**
250 000	2	2	2	**2**

Table C.2 M for different r/r_{cyl} when $r_{cyl}/\lambda=0.1$.

r/r_{cyl}	m_{limit}			M
	$\mathrm{Re}(E_z^{sec})$	$\mathrm{Im}(E_z^{sec})$	$\lvert E_z^{sec}\rvert$	
2.5	9	8	9	**9**
5	8	9	9	**9**
50	9	9	9	**9**
500	9	9	9	**9**
5 000	9	9	9	**9**
50 000	9	9	9	**9**
250 000	9	9	9	**9**

Table C.3 M for different r/r_{cyl} when $r_{cyl}/\lambda=1$.

r/r_{cyl}	m_{limit}			M
	$\mathrm{Re}(E_z^{sec})$	$\mathrm{Im}(E_z^{sec})$	$\lvert E_z^{sec}\rvert$	
2.5	36	35	36	**36**
5	34	36	36	**36**
50	35	36	36	**36**
500	36	36	36	**36**
5 000	36	36	36	**36**
50 000	36	36	36	**36**
250 000	36	36	36	**36**

Table C.4 M for different r/r_{cyl} when $r_{cyl}/\lambda=5$.

r/r_{cyl}	m_{limit}			M
	$\mathrm{Re}(E_z^{sec})$	$\mathrm{Im}(E_z^{sec})$	$\lvert E_z^{sec}\rvert$	
2.5	69	67	69	**69**
5	66	69	69	**69**
50	66	69	69	**69**
500	68	69	69	**69**
5 000	69	69	69	**69**
50 000	69	68	69	**69**
250 000	69	68	69	**69**

Table C.5 M for different r/r_{cyl} when $r_{cyl}/\lambda=10$.

r/r_{cyl}	m_{limit}			M
	$\mathrm{Re}(E_z^{sec})$	$\mathrm{Im}(E_z^{sec})$	$\lvert E_z^{sec}\rvert$	
2.5	164	165	165	**165**
5	165	165	165	**165**
50	165	165	165	**165**
500	165	165	165	**165**
5 000	165	165	165	**165**
50 000	165	165	165	**165**
250 000	165	165	165	**165**

Table C.6 M for different r/r_{cyl} when $r_{cyl}/\lambda=25$.

r/r_{cyl}	m_{limit}			M
	$\mathrm{Re}(E_z^{sec})$	$\mathrm{Im}(E_z^{sec})$	$\lvert E_z^{sec}\rvert$	
2.5	325	323	325	**325**
5	325	323	325	**325**
50	323	324	325	**325**
500	323	325	325	**325**
5 000	324	324	325	**325**
50 000	324	324	325	**325**
250 000	324	324	325	**325**

Table C.7 M for different r/r_{cyl} when $r_{cyl}/\lambda=50$.

r/r_{cyl}	m_{limit}			M
	$\mathrm{Re}(E_z^{sec})$	$\mathrm{Im}(E_z^{sec})$	$\lvert E_z^{sec}\rvert$	
2.5	483	480	483	**483**
5	483	480	483	**483**
50	483	482	483	**483**
500	481	483	483	**483**
5 000	483	483	483	**483**
50 000	483	483	483	**483**
250 000	483	483	483	**483**

Table C.8 M for different r/r_{cyl} when $r_{cyl}/\lambda=75$.

r/r_{cyl}	m_{limit}			M
	$\mathrm{Re}(E_z^{sec})$	$\mathrm{Im}(E_z^{sec})$	$\lvert E_z^{sec}\rvert$	
2.5	640	641	642	**642**
5	641	638	642	**642**
50	640	641	642	**642**
500	637	642	642	**642**
5 000	641	641	642	**642**
50 000	641	641	642	**642**
250 000	641	641	642	**642**

Table C.9 M for different r/r_{cyl} when $r_{cyl}/\lambda=100$.

r/r_{cyl}	m_{limit}			M
	$\mathrm{Re}(E_z^{sec})$	$\mathrm{Im}(E_z^{sec})$	$\lvert E_z^{sec}\rvert$	
2.5	1589	1587	1589	**1589**
5	1585	1589	1589	**1589**
50	1586	1589	1589	**1589**
500	1588	1588	1589	**1589**
5 000	1588	1589	1589	**1589**
50 000	1588	1588	1589	**1589**
250 000	1588	1588	1589	**1589**

Table C.10 M for different r/r_{cyl} when $r_{cyl}/\lambda=250$.

r/r_{cyl}	m_{limit}			M
	$\mathrm{Re}(E_z^{sec})$	$\mathrm{Im}(E_z^{sec})$	$\lvert E_z^{sec}\rvert$	
2.5	3164	3162	3165	**3165**
5	3164	3161	3165	**3165**
50	3161	3164	3165	**3165**
500	3163	3163	3165	**3165**
5 000	3162	3165	3165	**3165**
50 000	3164	3164	3165	**3165**
250 000	3164	3164	3165	**3165**

Table C.11 M for different r/r_{cyl} when $r_{cyl}/\lambda=500$.

r/r_{cyl}	m_{limit}			M
	$\mathrm{Re}(E_z^{sec})$	$\mathrm{Im}(E_z^{sec})$	$\lvert E_z^{sec}\rvert$	
2.5	4739	4739	4739	**4739**
5	4736	4739	4739	**4739**
50	4734	4739	4739	**4739**
500	4737	4737	4739	**4739**
5 000	4733	4739	4739	**4739**
50 000	4738	4738	4739	**4739**
250 000	4738	4738	4739	**4739**

Table C.12 M for different r/r_{cyl} when $r_{cyl}/\lambda=750$.

r/r_{cyl}	m_{limit}			M
	$\mathrm{Re}(E_z^{sec})$	$\mathrm{Im}(E_z^{sec})$	$\lvert E_z^{sec}\rvert$	
2.5	6309	6312	6312	**6312**
5	6306	6311	6312	**6312**
50	6306	6312	6312	**6312**
500	6310	6311	6312	**6312**
5 000	6303	6313	6312	**6313**
50 000	6311	6312	6312	**6312**
250 000	6311	6311	6312	**6312**

Table C.13 M for different r/r_{cyl} when $r_{cyl}/\lambda=1000$.

D MAPPING OF THE ELECTRIC FIELD AROUND THE WIND TURBINE

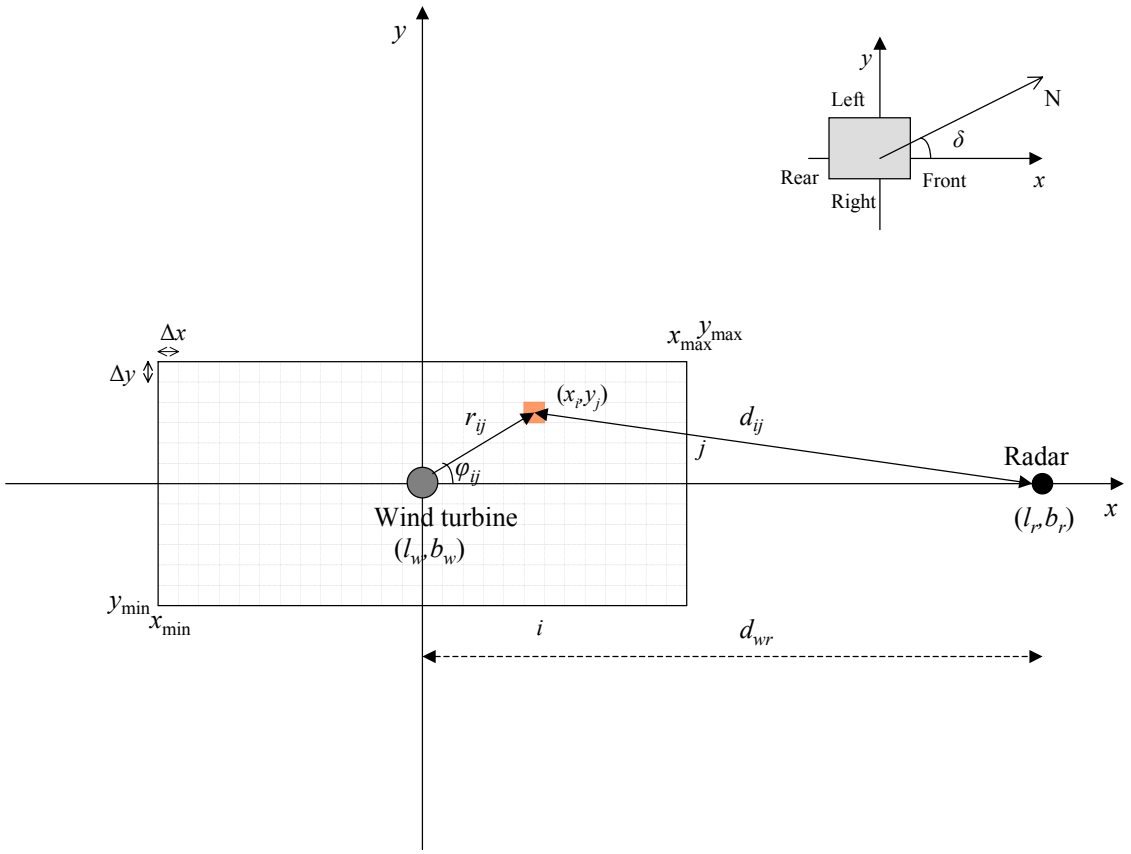

Figure D.1 Relative placement of radar, wind turbine, and grid for mapping the electric field around the wind turbine.

Figure D.1 shows the wind turbine, the radar, and the grid for mapping the electric field around the wind turbine. The wind turbine is placed in the center of the mapping grid. Three different coordinate systems are used:

1) Cartesian coordinate system (x, y, z_0), with $z_0 = 0$
2) Cylindrical coordinate system (r, φ, z_0), with $z_0 = 0$
3) Spherical coordinate system (R, l, b), with $R = 6378$ km (Earth radius)

The wind turbine is placed in origo in the cartesian and the cylindrical coordinate systems. It has the following position:

1) Cartesian: $(0,0,0)$
2) Cylindrical: $(0,0,0)$
3) Spherical: (R, l_w, b_w)

Here l_w is the wind turbine longitude, b_w is the wind turbine latitude, and $R = 6378$ km is the Earth radius.

The radar is placed in the following position in the three coordinate systems:

1) Cartesian: $(d_{wr}, 0, 0)$
2) Cylindrical: $(d_{wr}, 0, 0)$
3) Spherical: (R, l_r, b_r)

Here d_{wr} is the distance between the wind turbine and the radar and is given by (ref. Equation (A-1a) in Appendix A in (2)):

$$d_{wr} = R \cdot \arccos\left(\sin b_w \cdot \sin b_r + \cos b_w \cdot \cos b_r \cdot \cos(l_w - l_r)\right) \tag{D.1}$$

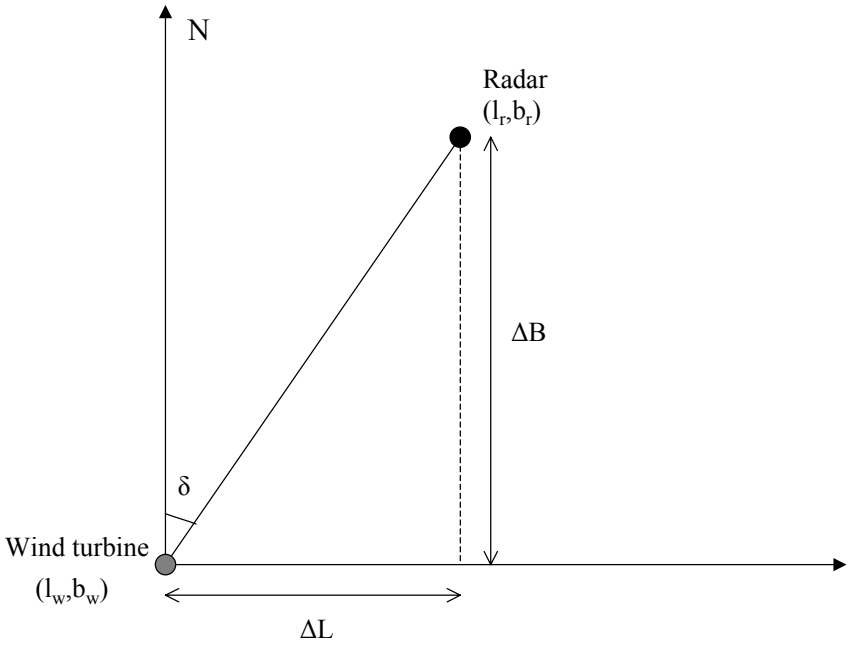

Figure D.2 The angel relative north for the wind turbine-radar system.

The angle δ relative north (clockwise) for the mapping grid is given by (see Figure D.2)

$$\delta = \begin{cases} \arctan\left(\dfrac{\Delta L}{\Delta B}\right), & b_r > b_w \\ \pi + \arctan\left(\dfrac{\Delta L}{\Delta B}\right), & b_r < b_w \\ \dfrac{\Delta L}{|\Delta L|} \cdot \dfrac{\pi}{2}, & b_r = b_w, \ \ l_r \neq l_w \end{cases} \tag{D.2}$$

where

$$\begin{aligned}\Delta B &= R\cdot\left(b_r - b_w\right)\\ \Delta L &= R\cdot\cos b_w\cdot\left(l_r - l_w\right)\end{aligned} \tag{D.3}$$

Here we have assumed that the Earth is locally flat (lines of longitude locally parallel).

The total grid width ΔX_{grid} is

$$\Delta X_{grid} = x_{\max} - x_{\min} \tag{D.4}$$

and the total grid heigth ΔY_{grid} is

$$\Delta Y_{grid} = y_{\max} - y_{\min} \tag{D.5}$$

The coordinates of an arbitrary element ij in the grid are

1) Cartesian: $(x_i, y_j, 0)$
2) Cylindrical: $(r_{ij}, \varphi_{ij}, 0)$

Here i denotes the $(i+1)$ th element of the grid along the x-axis, and j denotes the $(j+1)$ th element of the grid along the y-axis.

The coordinates x_i and y_j can be calculated from

$$\begin{aligned}x_i &= x_{\min} + \tfrac{1}{2}\Delta x + i\cdot\Delta x, \quad i = 0,\ldots(n_x - 1)\\ y_i &= y_{\min} + \tfrac{1}{2}\Delta y + j\cdot\Delta y, \quad \mathrm{j} = 0,\ldots(n_y - 1)\end{aligned} \tag{D.6}$$

where n_x and n_y are the number of grid elements along the x- and y-axis respectively and are given by

$$\begin{aligned}n_x &= \frac{x_{\max} - x_{\min}}{\Delta x}\\ n_y &= \frac{y_{\max} - y_{\min}}{\Delta y}\end{aligned} \tag{D.7}$$

and r_{ij} and φ_{ij} can be found from

$$r_{ij} = \sqrt{x_i^2 + y_j^2} \tag{D.8}$$

and

$$\varphi_{ij} = \begin{cases} \arctan\left(\dfrac{y_j}{x_i}\right), & x_i > 0 \\ \pi + \arctan\left(\dfrac{y_j}{x_i}\right), & x_i < 0 \\ \dfrac{y_j}{|y_j|} \cdot \dfrac{\pi}{2}, & x_i = 0,\ y_j \neq 0 \end{cases} \tag{D.9}$$

If there is no wind turbine present, the electric field amplitude E_0^{ij} at grid element ij is given by

$$E_0^{ij} = \frac{E_0^r}{d_{ij}} \tag{D.10}$$

where E_0^r is the electric field amplitude at 1 m distance from the radar, and d_{ij} is the distance from the radar to grid element ij. The distance d_{ij} is found from

$$d_{ij} = \sqrt{\left(d_{wr} - x_i\right)^2 + y_j^2} \tag{D.11}$$

where d_{wr} is the distance between the wind turbine and the radar as given by Equation (D.1). The total electric field at grid element ij when the wind turbine is present can then be calculated from Equations (2.1)-(2.5) when E_0^{ij}, as given by Equation (D.10), is used as the electric field amplitude E_0 of the primary wave.

E IMPLEMENTATION OF THE SHADOW EFFECTS CALCULATIONS IN WTES

The WTES (Wind Turbine and Electromagnetic Systems) software was developed by FFI to evaluate the effects of windmill development on telecommunication and radar (1). The software was developed in LabView v8.2.

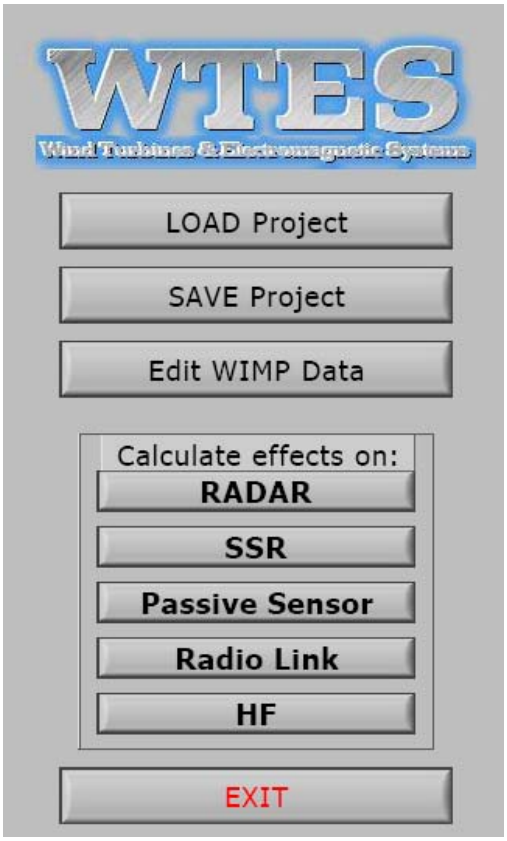

Figure E.1 The WTES Main program (Front Panel of WTES Main.vi).

The Front Panel for WTES is shown in Figure E.1. Calculations can be performed for the following systems:

- RADAR
- SSR (Secondary Surveillance Radar)
- Passive Sensor
- Radio Link
- HF

The results from the calculations are presented as a bitmap that can be plotted in the chart handling system MARIA.

For each system different types of calculations can be performed. For RADAR one type of calculation is the Shadow Effect calculations, and we will in the following describe how the Shadow Effects calculations are implemented in WTES. Note that the implementation procedure is general, and can be applied also for other new calculation modules.

In order to implement the Shadow Effects calculations in WTES, the following new files must be generated:

1) Generate Shadowing Pixmap.vi
2) Init Shadowing Cluster.ctl

In addition, the following existing WTES-files must be modified:

3) Init Cluster.ctl
4) RADAR Settings.vi
5) RADAR Calculations.vi

E.1 Generate Shadowing Pixmap.vi

Generate Shadowing Pixmap.vi (together with its subroutines) contains the new calculation module. It performs the Shadow Effect calculations and generates the corresponding bitmap for displaying the results on the map. A schematic view of the Generate Shadowing Pixmap.vi is shown in Figure E.2. The Front Panel is shown in Figure E.3.

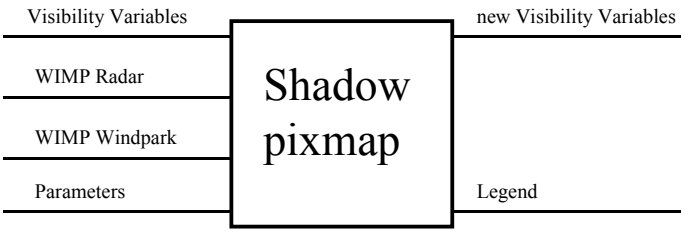

Figure E.2 Schematic view of Generate Shadowing Pixmap.vi.

Input parameters:

Visibility Variables:	Contains the parameters required for generating the bitmap, see Table E.1.
WIMP Radar:	Input from WIMP (to the main program) containing information about the radar.
WIMP Windpark:	Input from WIMP (to the main program) containing information about the windpark.
Parameters:	Input from RADAR Settings.vi containing information specific to the Shadow Effects calculations (set by the user).

Output parameters:

New Visibility Variables:	Contains the information required for generating the bitmap, see Table E.1.
Legend:	Contains the information about the legend for the bitmap.

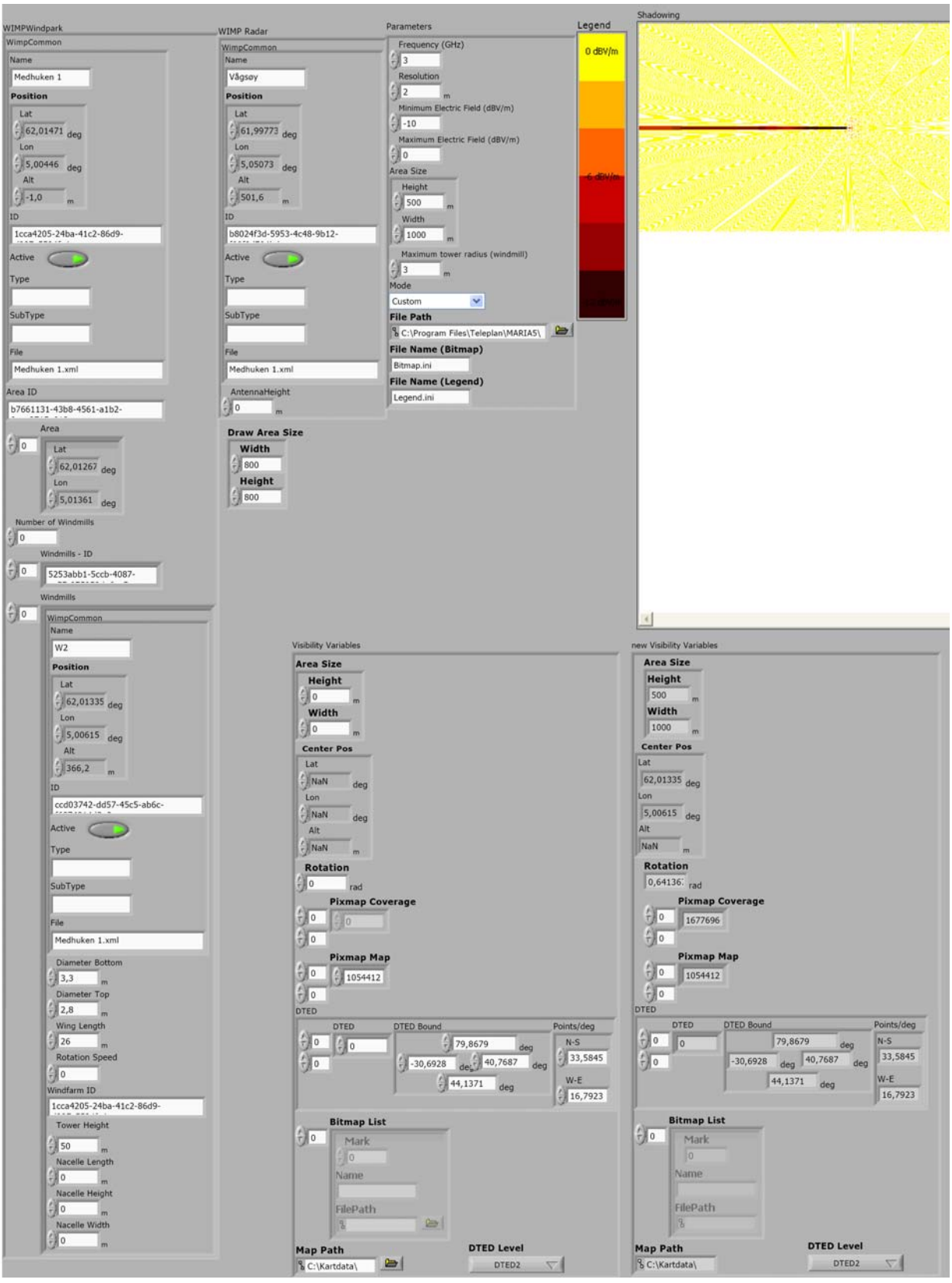

Figure E.3 The Front Panel for the Generate Shadowing Pixmap.vi.

	Visibility Variables	New Visibility Variables
Area Size (Height, Width)	-	Values are set in Generate Shadowing Pixmap.vi. (Received as input (Parameters) from RADAR Settings.vi).
Center Position (Lat, Lon, Alt)		Values are set in Generate Shadowing Pixmap.vi.
Rotation		Values are set in Generate Shadowing Pixmap.vi.
Pixmap Coverage		Values are set in Generate Shadowing Pixmap.vi. (Results from the calculations).
Pixmap Map	Initial values set under Init Frame in RADAR Calculations.vi	-
DTED (DTED, DTED bound, Points/deg)		-
Bitmap List (Mark, Name, Current)		New values are set in RADAR Calculations.vi
Map Path		-
DTED Level		-

Table E.1 The input and output parameters Visibility Variables and New VisibilityVariables.

E.2 Init Shadowing Cluster.ctl

Init Shadowing Cluster.ctl contains the framework for holding the input parameters specific to the Shadow Effects calculations, see Figure E.4.

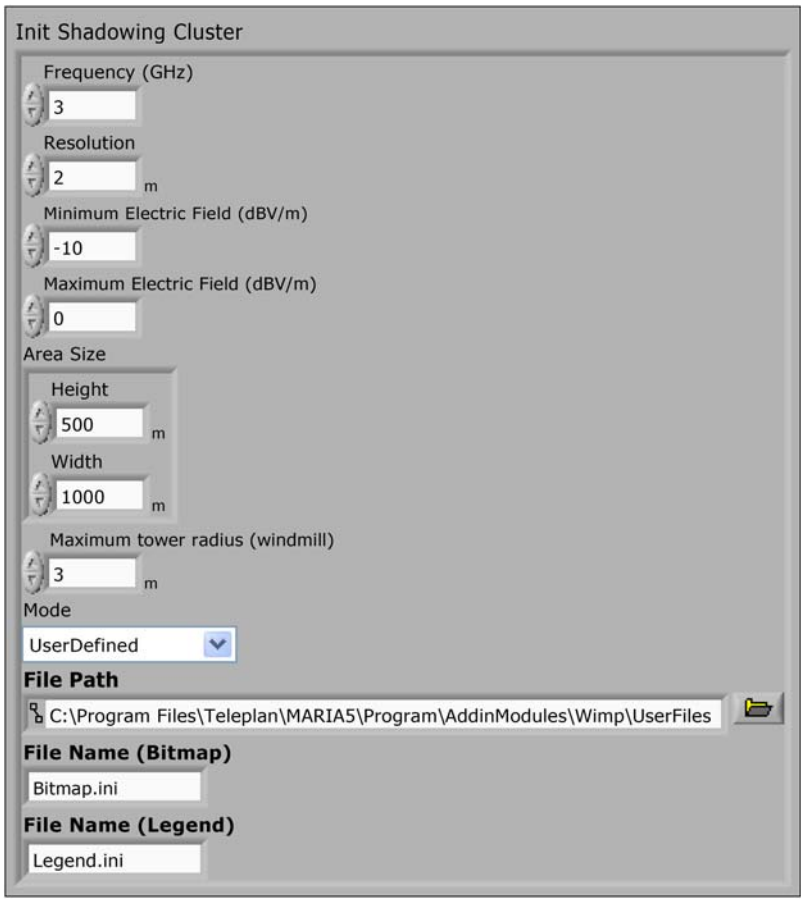

Figure E.4 The Front Panel for the Init Shadowing Cluster.ctl.

E.3 Init Cluster.ctl

Init Cluster.ctl contains the framework for holding all the input parameters for the different calculation modules. The controller Init Shadowing cluster.ctl must be implemented in Init Cluster.vi.

E.4 RADAR Settings.vi

RADAR Settings.vi is used to manually set the input parameters for the different calculation modules.

On the Front Panel for the RADAR Settings.vi a separate pane for “Shadow Effects” must be generated, see Figure E.5.

In the Block Diagram for the RADAR Settings.vi the necessary modifications to include the settings for the Shadow Effects calculations must be done (both in the Init Frame and in the Main Frame).

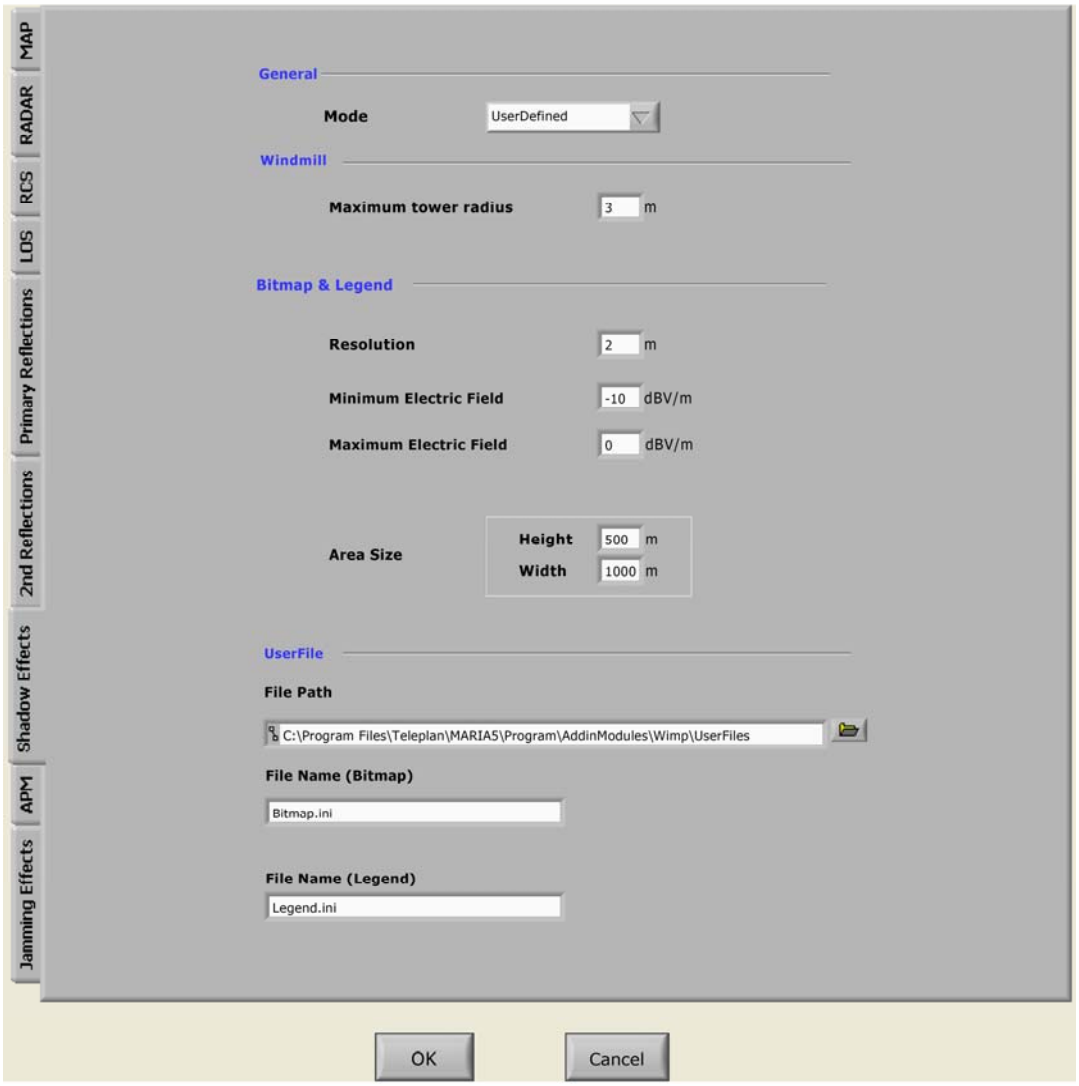

Figure E.5 The Front Panel for the RADAR Settings.vi.

E.5 RADAR Calculations.vi

RADAR Calculations.vi runs the radar calculations.

On the Front Panel for the RADAR Calculations.vi the Shadow Effects calculations must be included as an option in the menu.

In the Block Diagram for the RADAR Calculations.vi the Shadow Effects calculations must be included by adding a case to the case structure that holds the different calculation modules, see Figure E.6.

Input to the case-structure:

- Visibility Variables (see Table E.1)
- WIMP Data (input from WIMP containing WIMP Windpark and WIMP Radar information, see Figure E.3)

Output from the case-structure:

- New Visibility Variables (see Table E.1)

A new calculation module can be implemented in the RADAR Calculations.vi by the following procedure:

1) Copy the Shadow Effects calculation case.
2) Replace the Generate Shadowing Pixmap.vi (placed at the center in the upper part of the Block Diagram shown in Figure E.6) by the new calculation module.
3) Change the Parameters input (for the Generate Shadowing Pixmap.vi) to the Parameters input specific for the new calculation module.
4) Change the information in Description&TipStrip

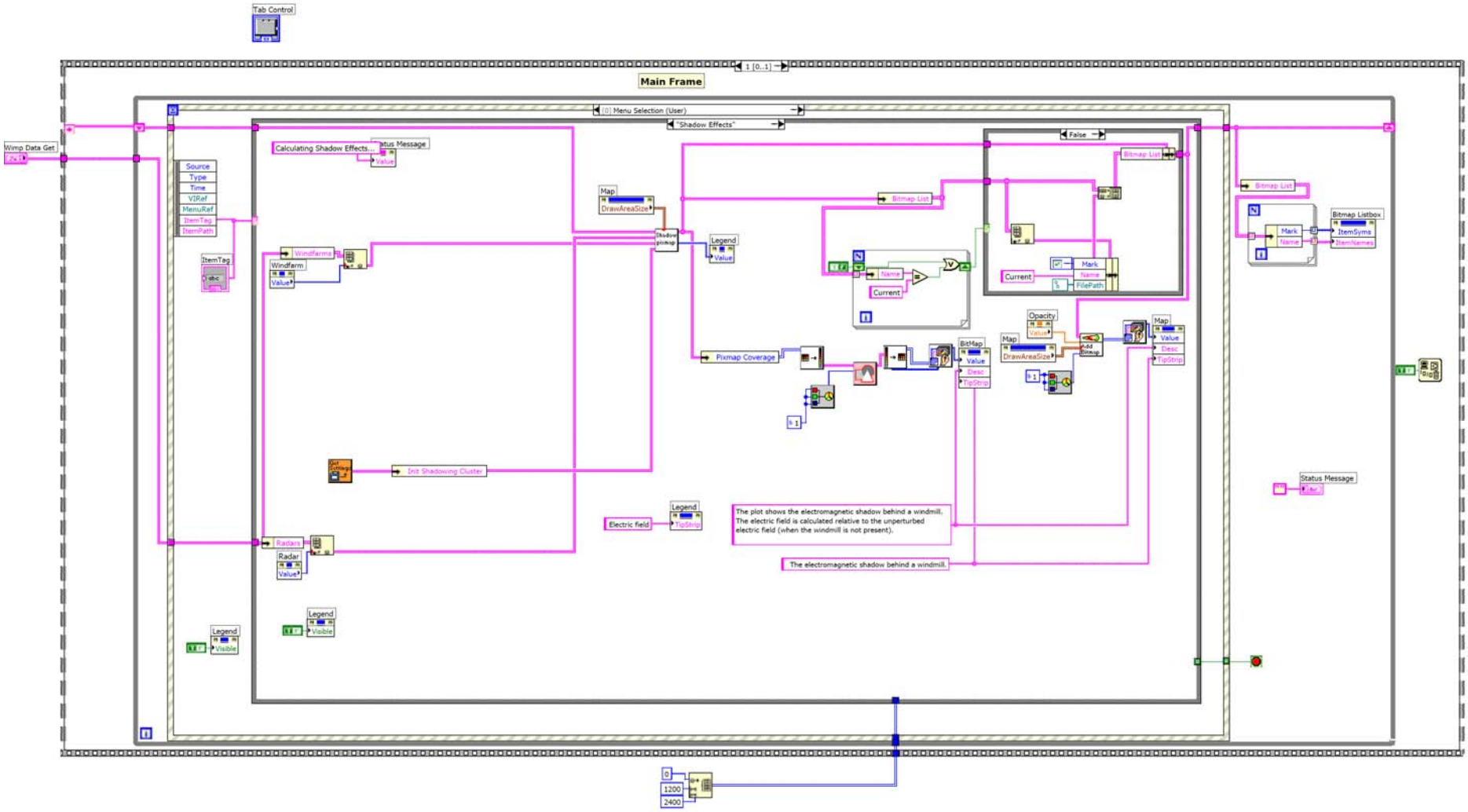

Figure E.6 The Block Diagram for the RADAR Calculations.vi, showing the case for the Shadow Effects calculations.

References

(1) B J Meland, E B Nilssen, G Høye, M Mjanger, S Kristoffersen (2007): Wind Turbines and Electromagnetic Systems (WTES) - Software documentation, FFI/RAPPORT-2007/00833.

(2) J. R. Wertz (2001): Mission geometry; Orbit and Constellation Design and Management, Microcosm Press, Kluwer Academics Publishers.

(3) Martin Howard and Colin Brown (2004): Results of the electromagnetic investigations and assessments of marine radar, communications and positioning systems undertaken at the North Hoyle wind farm by QinetiQ and the Maritime and Coastguard Agency, QinetiQ/03/00297/1.1, MCA MNA 53/10/366, 22 November 2004.

(4) Dave Trappeniers and Emmanuel Van Lil (2005): Computation of the effects of wind turbines on aeronautical radar and communication systems, Version 8, 29-07-2005, Belgocontrol.

(5) A. Frye and B. D. Bloch (2003): Final Report: Effect of obstacles on HF-supported guidance systems, Follow-up study, EADS Deutschland GmbH.

(6) J G Gallagher (2003): Radio frequency and radar shadowing, The impact of Robin Wigg wind turbines on maritime radio frequency systems, Technical report, QINETIQ/S&E/SPS/TR030449.

(7) C Samela, C Fernandes, L Fauro: TV Interference from Wind Turbines.

(8) M M Butler and D A Johnson (2003): Feasibility of mitigating the effects of wind farms on primary radar, ETSU W/14/00623/REP, DTI PUB URN No 03/976.

(9) G J Poupart (2003): Wind farms impact on radar aviation interests - Final report, FES W/14/00614/00/REP, DTI PUB URN 03/1294.